COMPUTATIONAL ANALYSIS OF SPIRAL GROOVE THRUST BEARINGS AND FACE SEALS

by

Nicole Zirkelback
Dr. Luis San Andrés

May 1998

TRC-SEAL-7-98

Texas A&M University
Mechanical Engineering Department

COMPUTATIONAL ANALYSIS OF SPIRAL GROOVE THRUST BEARINGS AND FACE SEALS

NICOLE LISA ZIRKELBACK

P.I. Dr. Luis San Andrés

TRC-Seal-1-98

April 1998

A Research Progress Report to the
Turbomachinery Research Consortium

EXECUTIVE SUMMARY

COMPUTATIONAL ANALYSIS OF SPIRAL GROOVE THRUST BEARINGS AND FACE SEALS

Analyses for incompressible and compressible spiral groove thrust bearings (*SGTBs*) and face seals (*SGFSs*) are presented. A successive approximation linearizes the partial differential equation of pressure that arises in the compressible fluid analysis. The zeroth- and first-order equations giving the static and dynamic performance of *SGFSs*, respectively, are solved using the finite element method for both incompressible and compressible (ideal gas) fluids. Favorable comparisons with the *Narrow Groove Theory* and a *FEM* analysis validate the incompressible fluid case for *SGTBs* without inward radial flow. A parametric study indicates effects of changing face seal geometry on the opening force, force coefficients, leakage rate, and power loss and gives the optimum *SGFS* geometry. Validation of the isothermal compressible fluid model occurs by comparison of the static and dynamic *SGTB* and *SGFS* behavior with previous *NGT* analyses. The optimum compressible fluid *SGFS* geometry follows from a parametric study, indicating the advantages of using grooved face seals with seal dams over traditional mechanical face seals and oil lubricated seal rings.

A skyline profile method for efficient storage of the sparse matrices arising from the FEM model allows a very fast numerical solution of the unsymmetrical system of equations for compressible fluid *SGFSs* and *SGTBs*. The *PC* Fortran programs *SPIRAL* and *SPIRALC* for the analysis of incompressible fluid and ideal gas *SGFSs* and *SGTBs* are availabe to TRC members. The programs are adequately documented and include a *User's Manual* with relevant examples

TABLE OF CONTENTS

LIST OF TABLES

LIST OF FIGURES

NOMENCLATURE

a	Relaxation parameter for successive approximation
B	Groove rotation direction (See Appendix A for definitions.)
c	Ridge clearance [m]
c_g	Groove depth [m]
C_{zz}, $\overline{C}_{zz}$	Axial damping coefficient [N·s/m]; $C_{zz} = C_{zz}/C_*$ (See Appendix A.)
D_o, D_i, D_{gi}	Outer, inner, groove inner diameter [m]; $D_o = 2{\cdot}R_o$; $D_i = 2{\cdot}R_i$; $D_{gi} = 2{\cdot}R_{gi}$
h	Film thickness [m]
K_{zz}, $\overline{K}_{zz}$	Axial stiffness [N/m]; $\overline{K}_{zz} = K_{zz}/K_*$ (See Appendix A.)
l	Radial seal dam extent; $l = \left(R_g - R\right)\Big/(1-R)$
$\dot{m}_{r_i}$, $\dot{m}_{\theta_i}$	First-order mass flow rates
N	Speed [rev/s]
N_g	Number of grooves
n_{pe}	Number of nodes per element
P, P_o, $\overline{P}$	Pressures at speeds (Ω, Ω_o) [Pa]; $\overline{P} = P/P_*$ (See Appendix A.)
ΔP	Pressure variation, $\Delta P = \frac{\partial P}{\partial \Omega}\Big\|_{\Omega_o} \Delta\Omega$
P_a, P_{ref}, P_{avg}	Ambient, reference, and average pressures [Pa] (See Appendix A.)
P_0, P_1	Zeroth and first order pressure fields, [Pa], [Pa/m], [Pa·s/m]
P_{rat}	Pressure ratio from outer to inner diameter; $P_{rat} = P_o/P_i$
$\wp$	Power loss from drag torque [W]; $\wp = \Im\Omega$; $\overline{\wp} = \wp/\wp_*$ (See Appendix A.)
Q	Leakage flow rate [ℓ/min]; $\overline{Q} = Q/Q_*$ (See Appendix A.)
q_n	Flow normal to an element
R	Radius ratio; $R = R_i/R_o$
R_i, R_o	Inner and outer seal dam radii, respectively [m]
R_{gi}, R_{go}	Inner and outer groove portion radii, respectively [m]
R_g	Grooved radius ratio; $R_g = R_{gi}/R_o$
(r, Θ, z)	Cylindrical coordinates, groove surface stationary, $\Theta = \theta + \Omega t$
(r, θ, z)	Cylindrical coordinates, groove surface rotating
$\Re_g$	Gas constant [J/kg·K]
S	Sommerfeld number; $S = \mu N \pi R_o^2 \left(R_o/c_g\right)^2 \Big/ W$
T	Temperature [K]
$\Im$	Friction torque [N·m]
t	Time [sec]
W, $\overline{W}$	Load [N]; $\overline{W} = W/W_*$ (See Appendix A.)
w_r, w_g	Arc width of groove and ridge, respectively [rad]
Z	Complex impedance [N/m]; $Z = K_{zz} + \mathbf{i}\omega C_{zz}$
Δz	Perturbations in axial direction [m]
α_g	Groove width ratio; $\alpha_g = w_g \Big/ \left(w_r + w_g\right)$
β	Spiral groove angle [°]; $\beta = 90° \Rightarrow$ radial grooves

Γ^e	Element boundary
δ	Groove depth ratio, $\delta = c_g/c$
ε_z	Dimensionless eccentricity; $\varepsilon_z = 1 - c/c_g$
θ	Circumferential coordinate attached to rotating face
Θ	Circumferential coordinate fixed to stationary face, $\Theta = \theta + \Omega t$
Θ_{g-r}	Arc length of a groove-ridge pair, $\Theta_{g-r} = 2\pi/N_s$
Λ	Speed number $\Lambda = 6\mu\Omega/p_c\left(R_o/c\right)^2$ (See Appendix A.)
μ	Fluid viscosity [Pa·s]
ρ	Fluid density [kg/m^3]
σ	Frequency number; $\sigma = 2\Lambda\left(\omega/\Omega\right)$
$\left\{\Psi_i\right\}_{i=1}^{n_{pe}}$	Shape functions within the finite element
ω	Frequency of dynamic axial motions
Ω	Rotational speed [rad/s]
Ω^e	Finite element sub-domain

Subscripts

gi	Inner radial groove extent
go	Outer radial groove extent
i	Inner radius
o	Outer radius, starting value
0	Zeroth-order
1	First-order
*	Characteristic values (See Appendix A.)

Superscripts

e	Finite element
*	Original value

Operators

$\bar{\nabla}\cdot\left(\bar{\nabla}\phi\right)$	Divergence of a gradient in cylindrical coordinates; $\bar{\nabla}\cdot\left(\bar{\nabla}\phi\right) = \frac{1}{r}\frac{\partial}{\partial r}\left(r\frac{\partial\phi}{\partial r}\right) + \frac{1}{r}\frac{\partial}{\partial\theta}\left(\frac{1}{r}\frac{\partial\phi}{\partial\theta}\right)$; where ϕ is a scalar function

INTRODUCTION

With the advent of strict mandates from environmental protection laws requiring virtual elimination of harmful leakage in industrial processes, better sealing technologies must be developed to prevent release of these volatile and potentially dangerous process fluids into the atmosphere. The spiral groove face seal (*SGFS*) offers numerous advantages over conventional contacting mechanical seals. Grooves etched on the mating ring of the sealing surfaces do not wear from contact while rotating, greatly lessening the need to overhaul machines for seal replacement. Dry (gas lubricated) operation allows the face seal to perform with less complicated and expensive external support systems like those required for oil lubricated seals. The use of tandem and double sealing arrangements with inert buffer gases allow application of the *SGFS* in machines handling highly volatile process fluids with virtually zero leakage to the atmosphere.

The first analyses adopted to model thin-film grooved bearing geometries use the Narrow Groove Theory (*NGT*) where an infinite number of grooves is the primary assumption. This analysis, as initially applied to parallel, helically grooved configurations, is mostly found for herringbone grooved journal bearings (*HGJBs*). A detailed review of the pertinent literature for *HGJBs* can be found in Zirkelback and San Andrés (1997). In general, the *NGT* is limited to performance prediction for concentric

---

This thesis follows the style and format of ASME JOURNAL OF TRIBOLOGY.

journal operation, and although few advances have been made for modeling turbulent flow, the *NGT* is mainly limited to prediction in the laminar flow regime.

The groove shape became the primary concern when applying the *NGT* to spiral groove thrust bearings (*SGTBs*) due to the logarithmic spiral contour of the grooves. Muijderman (1966) presents an extensive *NGT* analysis for various spiral and herringbone groove thrust bearing configurations including flat, spherical, and conical bearings, and approximate formulae are given for pressure, load capacity, friction torque, and the coefficient of friction for each bearing type. Experiments are also recorded for flat aerostatic *SGTBs*, and comparisons with the given analyses are provided. Although the analyses represent only incompressible fluids, the comparisons prove favorable. Finite differences are applied to solve the Reynolds equation for compressible fluids with constraining jump equations providing flow continuity at the groove-ridge interfaces in *SGTBs* as presented by James and Potter (1967).

Attempting to better represent the specified pressures at the boundaries of *SGFSs*, Sneck and McGovern (1973) introduce the narrow seal theory since the original *NGT*, as presented by Muijderman (1966), considers an infinitely wide thrust bearing face without specified boundary pressures. Despite the simplification of straight parallel grooves, the predictions using the narrow seal theory without pressure gradients compare well with results from Muijderman (1966). Constantinescu and Galetuse (1992) also consider extension of the *NGT* to calculate leakage in face seal applications with various groove types including straight grooves, spiral grooves, and herringbone grooves.

The shortcomings of the *NGT* warranted extensions of the original analyses for various theoretical aspects. Pan and Sternlicht (1967) present a simple heat transfer study that models thermal distortion of flat, ungrooved thrust bearing surfaces, where the drag-induced frictional power is conducted through the bearing faces. The analysis assumes that heat flow through the faces is uniform and purely axial; however, effects of the groove geometry are neglected in the thermal model since the viscous shear stress is calculated between two flat plates. Considering both *SGFSs* and Rayleigh step seals, Cheng, et al. (1969) discuss the relative placement of grooves and seal dams within the context of a *NGT* analysis that uses the Reynolds equation for compressible fluids. The authors conclude that seal dams on the low pressure side of the *SGFS* minimize leakage at the expense of axial stiffness, while seal dams on the high pressure side give higher values of stiffness. Hsing (1972) extends the *NGT* to include slip flow and flow turbulence using generalized coordinates to model most groove bearing geometries (*e. g.*, flat, spherical, conical, and cylindrical). Using results obtained previously, Hsing (1974) presents analytical solutions for force coefficients in spiral groove viscous pumps. Considering the same grooved geometries, Smalley (1972) submits the *NGT* in generalized coordinates and solves the governing equations with finite differences to give load capacity, power loss, leakage, and stiffness coefficients. Furthermore, Sato, et al. (1990) present an incompressible fluid *NGT* analysis in the generalized coordinates provided in Hsing (1972) to obtain the optimum groove geometry for both the *SGTB* and *HGJB* configurations handling viscous, incompressible fluids.

Malanoski and Pan (1965) analyze the static and dynamic characteristics of inward and outward pumping *SGTBs* operating with compressible fluids. The total dynamic force, given by frequency dependent equivalents of stiffness and damping, determines the thrust bearing stability and dynamic performance. Two stability analyses, given in Constantinescu and Galetuse (1987), use the *NGT* to provide dynamic stability limits for *SGTBs* operating with compressible fluids. While the first analysis provides a critical mass parameter to determine the stability limit, a simpler approach furnishes an analytical formula that shows good agreement with the former limits rendered.

Special considerations necessary when dealing with cryogenic fluids are noted for the design of a particular *SGFS* in Shapiro, et al. (1984). The analysis implemented applies enhancements to Muijderman's *NGT* in turbulence, fluid inertia, and thermal and elastic deformations to make predictions of film thickness, axial stiffness, leakage, power loss, and temperature rise for increasing rotational speeds. Salant and Homiller (1992) present a finite difference solution of the Reynolds equation for incompressible fluids that accounts for fluid cavitation in upstream pumping *SGFS* operating in both single and double seal configurations. A parametric study reveals instability due to negative stiffness when a *SGFS* operates as a single seal; however, properly designed *SGFSs* remain stable in double seal configurations. Lastly, Kowalski and Basu (1995) optimize the *SGFS* geometry for reverse rotation and forward rotation simultaneously by solving the Reynolds equations for compressible fluids with finite differences. Tests verify the feasibility of meeting the design demands; however, an expected increase in leakage accompanies the optimized bidirectional design (23° groove angle).

Experimental studies in addition to that presented by Muijderman (1966) include tests by James and Potter (1967) performed on a test rig that employs ceramic *SGTBs* and spiral groove compressors with air. The experiments involve measurements of outlet pressure and air flow rate. Static loads with 10% possible error and an optimum geometry are determined from the tests. In a series of reports, DiRusso (1982, 1984, 1985) presents measurements of the film thickness and drag torque for various *SGFS* configurations operating with air. The latter two reports (DiRusso, 1984, 1985) concentrate on the dynamic axial oscillations of the seal face and the effects of misalignment while reporting instabilities for outward pumping *SGFS* when the hydrodynamic pressure forces overcome the spring force at seal liftoff. DiRusso (1983) also presents a parametric study using a previous *NGT* study to analytically determine the optimum geometry of *SGFSs*. Experiments presented in Furuishi, et al. (1985) for a *SGTB* operating with water give the load carrying capacity and corresponding minimum film thicknesses for geometries with varying groove depths and support configurations. Different support configurations lessen thermal coning so that experiments match more closely with the simplified *NGT* analysis presented. However, the softer support configurations also diminish the load carrying capacity of the spiral groove thrust bearing.

With its ability to easily represent complicated geometries and any number of grooves, the Finite Element Method (*FEM*) has been the more recent choice for solving the Reynolds equation applied to spiral groove bearing and seal designs. Reddi (1969) and Reddi and Chu (1970) discuss application of the *FEM* to incompressible and

compressible fluid spiral groove bearings, respectively. Finite element solutions for load capacity and axial force coefficients are referred to by Someya (1989) for an incompressible fluid *SGTB* having a pressure dam on the bearing inner diameter. Bonneau, et al. (1993) present a finite element model of *SGFSs* that uses upwinding to allow solution of the nonlinear Reynolds equation for compressible fluids. Graphs showing load and leakage rate illustrate the effects of mesh refinement and increased speed numbers.

OBJECTIVE

The present work includes analyses of isothermal, incompressible as well as compressible fluid *SGFSs* using the finite element method to solve the partial differential equations of hydrodynamic pressure. Analytical perturbations are performed for both cases, determining the dynamic axial force coefficients. To allow solution of the non-linear partial differential equation describing compressible fluids in *SGFSs*, the analysis utilizes the successive approximation approach described in Reddi and Chu (1970) to obtain solutions for the zeroth-order (equilibrium) pressure distribution. The lack of meaningful experimental data in the archival literature for this particular grooved configuration makes comparison with previous analyses the primary means to verify the current model. Comparisons are made with the *NGT* (Muijderman, 1966) and with another *FEM* model (Someya, 1989) to validate the present incompressible fluid model with *SGTBs*. A parametric study for *SGFS* operating with incompressible fluids shows the effect of changing the face seal geometry and gives the optimum configuration. Confirmation of the compressible fluid model occurs by comparison with Lebeck (1991), Malanoski and Pan (1965), James and Potter (1967), and Bonneau, et al. (1993). The effect of adjusting compressible fluid *SGFS* geometry as obtained from a parametric study renders the geometry for optimum gas face seal performance.

ANALYSIS

GENERAL DESCRIPTION

Figure 1 shows two configurations of the spiral groove face seal (*SGFS*). In Figure 1.a, the grooved surface is stationary while the flat mating surface rotates (clockwise) with speed Ω. The (r, Θ, z) coordinate system, connected to the stationary grooved surface, is used to describe this seal geometry. Figure 1.b shows the second configuration of the *SGFS* where the grooved surface rotates at speed Ω (counterclockwise) opposing a stationary, flat mating surface. This configuration is described with the (r, θ, z) coordinate system attached to the rotating, grooved surface.

The coordinate transformation between the two configurations is given by

$$\Theta = \theta + \Omega t \tag{1}$$

and groove rotation direction (B) of ± 1 implies stationary or rotating grooves depending on the configuration. (See Appendix A.) The seal has inner radius R_i denoting the beginning of the inner seal dam and outer radius R_o indicating the end of the outer seal dam. The inner and outer radii for the grooved portion are defined with R_{gi} and R_{go}, respectively. It is assumed that the rotating surface can only move axially so that tilt angles can be neglected. Several descriptive parameters characterize the groove geometry. The ridge clearance (c) plus the groove depth (c_g) give the maximum clearance ($c + c_g$), and the groove depth ratio (δ) is described with $\delta = c_g/c$. The width ratio (α_g) is the fraction of the arc length of a groove-ridge pair $\left(\Theta_{g-r} = {}^{2\pi}/_{N_s}\right)$ that is occupied by a groove. The equation governing the logarithmic shape of the grooves is (Muijderman, 1966)

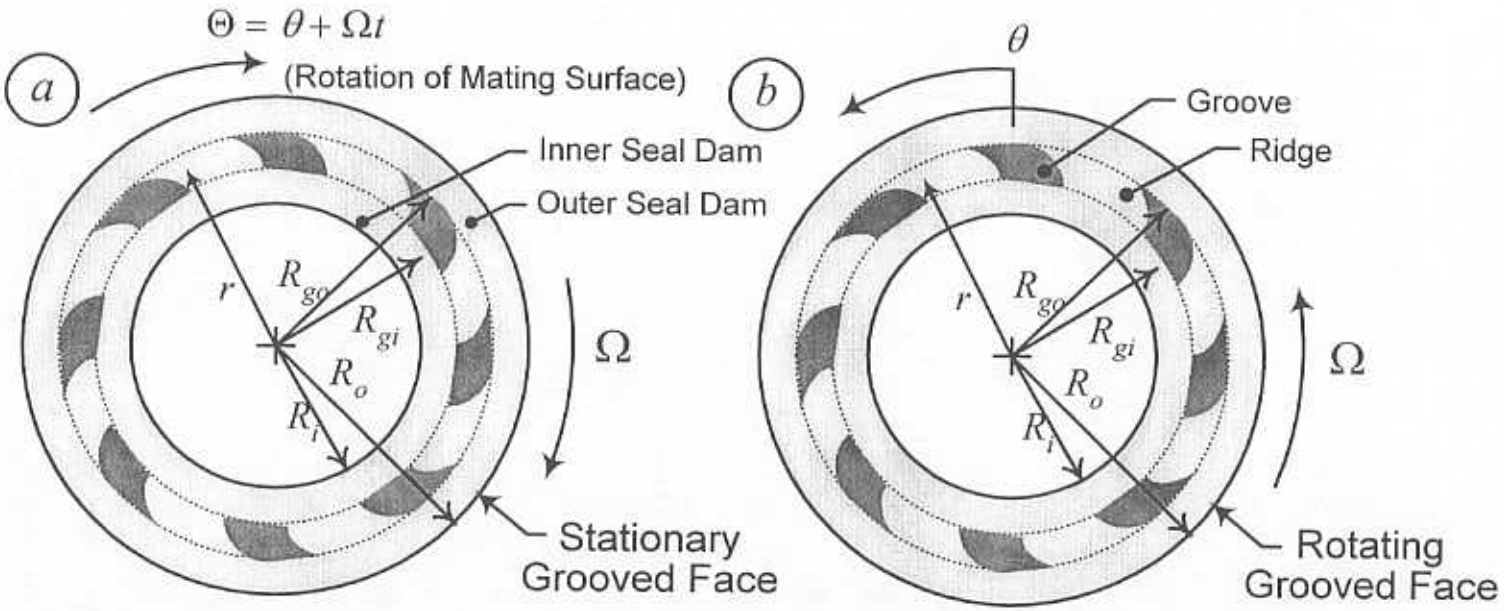

Fig. 1 Spiral groove face seal geometry.

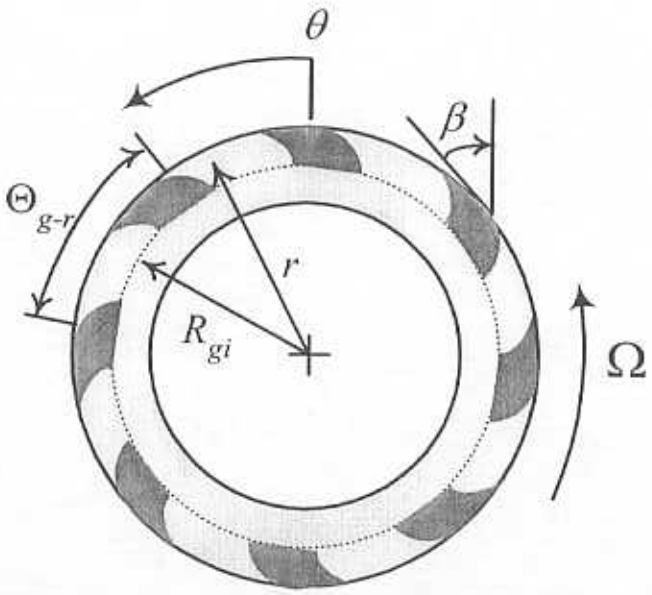

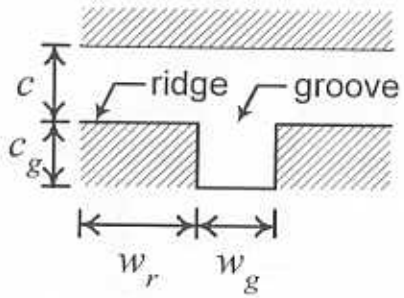

$$\alpha_g = w_g/(w_r + w_g)$$

$$\delta = c_g/c$$

$$r = R_{gi} e^{\theta \tan(\beta)}$$

$$\Theta_{g\text{-}r} = 2\pi/N_g$$

Fig. 2 Spiral groove face seal geometric parameters.

$$r = R_{gi} e^{\theta \tan(\beta)} \tag{2}$$

where the circumferential coordinate is represented by θ and the helix angle (β) is the angle of the groove from the tangent, with $\beta = 90°$ giving radial grooves as illustrated in Figure 2.

Incompressible Fluid SGFS Analysis

The lubricating fluid is regarded as incompressible, isoviscous, and newtonian. The appropriate Reynolds equation in cylindrical coordinates describing isothermal, laminar, inertialess fluid flow on the seal face is

$$\frac{1}{r}\frac{\partial}{\partial r}\left(\frac{rh^3}{12\mu}\frac{\partial P}{\partial r}\right)+\frac{1}{r}\frac{\partial}{\partial \theta}\left(\frac{h^3}{12\mu r}\frac{1}{\partial \theta}\frac{\partial P}{\partial \theta}\right)=\frac{\partial h}{\partial t}+B\frac{\Omega}{2}\frac{\partial h}{\partial \theta} \tag{3}$$
$$0 \le \theta \le \Theta_{g-r};\ \ R_i \le r \le R_o$$

where the groove rotation direction (B) of ±1 implies stationary or rotating grooves depending on the configuration. (See Appendix A.) Refer to the Nomenclature for proper definitions of all variables. The film thickness h in the equations above is described with

$$h = c \tag{4.a}$$

in the ridge region and

$$h = c + c_g \tag{4.b}$$

in the groove region.

The pressure for the seal is specified at the inner and outer radius as, respectively,

$$P(R_i,\theta,t) = P_i \tag{5.a}$$

$$P(R_o,\theta,t) = P_o \tag{5.b}$$

Since azimuthal thermal distortion and misalignments of the faces are neglected, the circumferential pressure distribution for each groove ridge pair is periodic.

$$P(r,\theta_o + n\Theta_{g-r},t)_{n=1,\ldots,N_g} = P(r,\theta_o,t) \tag{6}$$

PERTURBATION ANALYSIS FOR INCOMPRESSIBLE FLUID SGFSS

If the rotating surface describes small axial motions (Δz) from an equilibrium position (h_0), the film thickness is equal to

$$h(r,\theta,t) = h_0(r,\theta) + \Delta z\, e^{i\omega t} \;;\; \mathbf{i} = \sqrt{-1} \tag{7}$$

The effect of these small amplitude motions is to bring perturbations in the pressure about an equilibrium field (P_0), described by the superposition of zeroth- and first-order pressure fields:

$$P(r,\theta,t) = P_0(r,\theta) + P_1 \Delta z\, e^{i\omega t} \tag{8}$$

where P_0 is the zeroth-order pressure field, and P_1 is the perturbed first-order pressure.

With the following definition for the linear differential operator,

$$L(P) = \frac{1}{r}\frac{\partial}{\partial r}\left(\frac{rh^3}{12\mu}\frac{\partial P}{\partial r}\right) + \frac{1}{r}\frac{\partial}{\partial \theta}\left(\frac{h^3}{12\mu r}\frac{1}{r}\frac{\partial P}{\partial \theta}\right) \tag{9}$$

and the substitution of Equations (6) and (7) into the Reynolds Equation (2) gives the zeroth- and first-order equations as

Zeroth-Order Equation

$$L(P_0) = B\frac{\Omega}{2}\frac{\partial h_0}{\partial \theta} \tag{10}$$

First-Order Equations

$$L(P_1) = -\frac{1}{r}\frac{\partial}{\partial r}\left(\frac{3rh_0^2}{12\mu}\frac{\partial P_0}{\partial r}\right) - \frac{1}{r^2}\frac{\partial}{\partial \theta}\left(\frac{3h_0^2}{12\mu}\frac{\partial P_0}{\partial \theta}\right) + \mathbf{i}\omega \tag{11}$$

If Δz is arbitrary, it follows that $P_1 = 0$ on the seal boundaries since the inlet and outlet pressures are invariant.

The equilibrium fluid film seal forces (static) acting on the mating surface are obtained from the integration of the zeroth-order pressure field over the area of the seal face:

$$F_0 = N_g \int_{R_i}^{R_o} \int_0^{\Theta_{g-r}} \left(P_0 - P_{ref}\right) r\,d\theta\,dr \tag{12}$$*

while the stiffness and damping are obtained from real and imaginary parts of first-order pressure field integration,

$$Z = K_{zz} + \mathbf{i}\omega C_{zz} = -N_g \int_{R_i}^{R_o} \int_0^{\Theta_{g-r}} P_1\, r\,d\theta\,dr \tag{13}$$

Note that the partial differential equations from which the stiffness and damping coefficients result are not coupled. Hence, the force coefficients are frequency (ω) independent.

---

* P_{ref} denotes a reference pressure to account for force from on the other side of the face seal. P_{ref} is explicitly noted in the calculations given in Appendix A.

To utilize these expressions for forces and force coefficients (Eqns. 12 and 13), the respective pressure fields must be solved. This is accomplished using the finite element method. The program ***spiral.for*** uses the finite element method to solve the zeroth- and first-order pressure equations for a spiral groove face seal with an incompressible fluid using FORTRAN77 in the WINDOWS NT operating system. The finite element method applied to this analysis will now be discussed in more detail.

FINITE ELEMENT FORMULATION FOR INCOMPRESSIBLE FLUID SGFSS

The flow domain is discretized into a collection of 4-noded isoparametric finite elements. (Reddy, 1993) The pressure over a finite element is a linear combination of nodal values and shape functions $\{\Psi_i\}^e$ given by

$$P_0^e = \sum_{i=1}^{n_{pe}} \Psi_i \overline{P}_{0_i}^e \tag{14.a}$$

$$P_1^e = \sum_{i=1}^{n_{pe}} \Psi_i \overline{P}_{1_i}^e \tag{14.b}$$

This allows the differential pressure equations (10, 11) to be reduced into an algebraic system of linear equations. The Galerkin formulation of the zeroth-order pressure equations becomes

$$\sum_{j=1}^{n_{pe}} k_{ij}^e \overline{P}_{0_j}^e = -q_{0_i}^e + f_{0_i}^e \tag{15}$$

where Γ^e is the closure of the element domain Ω^e and

$$k_{ij}^{e}=\iint_{\Omega^{e}}\left(\frac{h_0^3}{12\mu}\right)^{e}\left\{\frac{\partial\Psi_i}{\partial r}\frac{\partial\Psi_j}{\partial r}+\frac{1}{r^2}\frac{\partial\Psi_i}{\partial\theta}\frac{\partial\Psi_j}{\partial\theta}\right\}^{e} r\,d\theta dr \tag{16.a}$$

$$q_{0_i}^{e}=\oint_{\Gamma^{e}}\Psi_i^{e}q_{\eta_0}\,d\Gamma^{e} \tag{16.b}$$

$$f_{0_i}^{e}=B\frac{\Omega}{2}\iint_{\Omega^{e}}h_0\frac{\partial\Psi_i^{e}}{\partial\theta}r\,d\theta dr \tag{16.c}$$

Note that once the nodal pressures are known, the flow rates can be obtained from the equation above by solving for $\left\{q_{0_i}^{e}\right\}$ along the element boundaries. These equations are condensed by enforcing the corresponding boundary conditions. The result is a symmetric system of equations that are then $\{LL^{T}\}$ decomposed and solved to obtain the discrete pressure field.

The first-order equations are obtained and solved in a similar manner. For finding P_1, the corresponding first-order element equations become:

$$\sum_{j=1}^{n_{pe}}k_{ij}^{e}\overline{P}_{1_j}^{e}=-q_{1_i}^{e}+f_{1_i}^{e}-\sum_{j=1}^{n_{pe}}S_{ij}^{e}\overline{P}_{0_j}^{e} \tag{17}$$

where

$$q_{1_i}^{e}=\oint_{\Gamma^{e}}\Psi_i^{e}q_{\eta_1}\,d\Gamma^{e} \tag{18.a}$$

$$f_{1_i}^{e}=\iint_{\Omega^{e}}\left[B\frac{\Omega}{2}\frac{\partial\Psi_i^{e}}{\partial\theta}-\mathrm{i}\omega\partial\Psi_i^{e}\right]r\,d\theta dr\;;\qquad \mathrm{i}=\sqrt{-1} \tag{18.b}$$

$$S_{ij}^{e}=\iint_{\Omega^{e}}\left(\frac{3h_0^2}{12\mu}\right)^{e}\left\{\frac{\partial\Psi_i}{\partial r}\frac{\partial\Psi_j}{\partial r}+\frac{1}{r^2}\frac{\partial\Psi_i}{\partial\theta}\frac{\partial\Psi_j}{\partial\theta}\right\}^{e} r\,d\theta dr \tag{18.c}$$

Since the finite element equations are symmetric, certain techniques allow storage of the banded matrix in a single vector with fewer zero elements occupying computer memory.

Compressible Fluid SGFS Analysis

If the fluid within the seal is considered as an (compressible) ideal gas at constant temperature (isothermal model), the density is directly proportional to the pressure of the fluid, or

$$\rho = \frac{P}{\Re_g T} \tag{19}$$

where the quantity $\Re_g T$ is constant if the seal characteristic temperature (T) does not change. Since gases have very low fluid viscosities, little temperature change between the inner and outer seal diameters is expected. The limited thermal capacity of gases justifies use of an isothermal, ideal gas for modeling, although other thermal aspects, such as thermal coning of the seal faces, become important. The Reynolds equation in cylindrical coordinates for an isoviscous and newtonian fluid sustaining isothermal, laminar, inertialess fluid flow on the seal face is

$$\bar{\nabla}\cdot\left(\frac{h^3}{12\mu}P\bar{\nabla}P\right) = \frac{B\Omega}{2r}\frac{\partial}{\partial\theta}(rPh) + \frac{\partial Ph}{\partial t} \tag{20}$$
$$0 \le \theta \le \Theta_{g-r}; \quad R_i \le r \le R_o$$

The same film thickness expressions and boundary conditions as in the incompressible case apply. (See Eqns. 4 through 6.) The method for solution of this non-linear partial differential equation is detailed in Reddi and Chu (1970) where a successive

approximation scheme is proposed. Considering a perturbation in rotational speed (Ω), *i.e.*,

$$\Omega = \Omega_o + \Delta\Omega \tag{21}$$

the linearization of pressure (as a function of speed) about this point gives

$$P(\Omega) = P(\Omega_o) + \left.\frac{\partial P}{\partial \Omega}\right|_{\Omega_o} \Delta\Omega \tag{22.a}$$

or

$$P = P_o + \Delta P \tag{22.b}$$

where P_o satisfies the steady-state form of Eqn. (20) for speed Ω_o. Neglecting derivatives of time for steady-state operation, substitution of the perturbed speed and pressure (Eqns. 21 and 22) into the Reynolds Equation (20) gives

$$\bar{\nabla}\cdot\left(\frac{h^3}{12\mu}\bar{\nabla}PP_o\right) = \frac{B}{2r}\frac{\partial}{\partial\theta}\left[rh\left(\Omega_o P + P_o\Omega\right)\right] \tag{23}$$

which is now a linear partial differential equation. For two sufficiently close values of (Ω, Ω_o), the successive approximation determines a sequence of pressures until the steady state form is satisfied, i. e.,

$$\bar{\nabla}\cdot\left(\frac{h^3}{12\mu}\bar{\nabla}P^2\right) = \frac{B}{2r}\frac{\partial}{\partial\theta}\left[rh(2\Omega P)\right] \tag{24}$$

Once this equilibrium pressure is determined, the forces and force coefficients can then be evaluated.

PERTURBATION ANALYSIS FOR COMPRESSIBLE FLUID SGFSS

If the rotating surface describes small axial motions (Δz) from an equilibrium position (h_0) at a frequency (ω), the film thickness is equal to

$$h(r,\theta,t) = h_0(r,\theta) + \Delta z\, e^{i\omega t} \quad ; \quad \mathbf{i}=\sqrt{-1} \tag{25}$$

where ω is the axial excitation frequency. The effect of these small amplitude motions is to bring perturbations in the pressure about an equilibrium field (P_0), described by the superposition of zeroth- and first-order pressure fields:

$$P(r,\theta,t) = P_0(r,\theta) + P_1(r,\theta)\Delta z\, e^{i\omega t} \tag{26}$$

where P_0 is the zeroth-order pressure field, and P_1 is the perturbed first-order pressure.

With substitution of the perturbed film thickness (Eqn. 25) and pressure (Eqn. 26) into the Reynolds equation (Eqn. 20), the first-order partial differential equation of pressure becomes

$$\begin{aligned} &\frac{1}{r}\frac{\partial}{\partial r}\left(r\,\dot{m}_{r_1}\right) + \frac{1}{r}\frac{\partial}{\partial\theta}\left(\dot{m}_{\theta_1}\right) + i\omega\left(P_1 h_0 + P_0\right) = 0 \\ &0 \le \theta \le \Theta_{g-r};\ \ R_i \le r \le R_o \end{aligned} \tag{27}$$

where the first-order mass flow rates are

$$\dot{m}_{r_1} = -\frac{1}{12\mu}\left(3h_0^2 P_0 \frac{\partial P_0}{\partial r} + h_0^3 \frac{\partial\left(P_0\, P_1\right)}{\partial r}\right) \tag{28.a}$$

$$\dot{m}_{\theta_1} = -\frac{1}{12\mu r}\left(3h_0^2 P_0 \frac{\partial P_0}{r\partial\theta} + h_0^3 \frac{\partial\left(P_0\, P_1\right)}{r\partial\theta}\right) + \frac{B\Omega r}{2}\left(P_0 + h_0 P_1\right) \tag{28.b}$$

Integration of the first-order pressure field gives stiffness (real part) and damping (imaginary part) coefficients, together representing a complex impedance

$$Z = K_{zz} + \mathbf{i}\,\omega\, C_{zz} = -N_g \int_{R_i}^{R_o} \int_{0}^{\Theta_{g-r}} P_1\, r d\theta dr \tag{29}$$

Note that once the first-order pressure field is solved and integrated, the stiffness and damping coefficients will be coupled and dependent on the excitation frequency (ω).

FINITE ELEMENT FORMULATION FOR COMPRESSIBLE FLUID SGFSs

The finite element analysis develops for the compressible fluid case in the same manner as before. However, it should be noted that the zeroth-order flow equations are non-linear though effectively linearized by the successive approximation method. The Galerkin formulation of the zeroth-order pressure equations becomes

$$\sum_{j=1}^{n_{pe}} k_{0_{ij}}^{e}\, \overline{P}_{0_j}^{e} = -q_{0_i}^{e} + f_{0_i}^{e} \tag{30}$$

where Γ^e is the closure of the element domain Ω^e and

$$k_{0_{ij}}^{e} = \iint_{\Omega^e} \left\{ \frac{h_0^3}{12\mu} \left[\left(\frac{\partial \Psi_i}{\partial r}\frac{\partial \Psi_j}{\partial r} + \frac{1}{r^2}\frac{\partial \Psi_i}{\partial \theta}\frac{\partial \Psi_j}{\partial \theta} \right) P_o + \left(\frac{\partial \Psi_i}{\partial r}\frac{\partial P_o}{\partial r} + \frac{1}{r^2}\frac{\partial \Psi_i}{\partial \theta}\frac{\partial P_o}{\partial \theta} \right) \Psi_j \right] - \frac{Bh\Omega_o}{2}\frac{\partial \Psi_j}{\partial \theta}\Psi_i \right\} r d\theta dr \tag{31.a}$$

$$q_{0_i}^{e} = \oint_{\Gamma^e} \Psi_i^e \dot{m}_{n_0}\, d\Gamma^e \tag{31.b}$$

$$f_{0_i}^{e} = \iint_{\Omega^e} \frac{Bh_0\Omega_o}{2} P_o \frac{\partial \Psi_i^e}{\partial \theta} r d\theta dr \tag{31.c}$$

where

$$P_0 = \sum_{k=1}^{n_{pe}} \Psi_k P_{0_k} \tag{31.d}$$

The result of these equations due to fluid compressibility renders an asymmetric system of algebraic equations that are then decomposed (LU) and solved to obtain the discrete pressure field.

The first-order equations are obtained and solved in a similar manner. For finding P_1, the corresponding first-order element equations become:

$$\sum_{j=1}^{n_{pe}} k_{1_{ij}}^e \overline{P}_{1_j}^e = -q_{1_i}^e + f_{1_i}^e \tag{32}$$

where

$$k_{1_{ij}}^e = \iint_{\Omega^e} \left\{ \frac{h_0^3}{12\mu} \left[\left(\frac{\partial \Psi_i}{\partial r} \frac{\partial \Psi_j}{\partial r} + \frac{1}{r^2} \frac{\partial \Psi_i}{\partial \theta} \frac{\partial \Psi_i}{\partial \theta} \right) P_0 + \left(\frac{\partial \Psi_j}{\partial r} \frac{\partial P_0}{\partial r} + \frac{1}{r^2} \frac{\partial \Psi_i}{\partial \theta} \frac{\partial P_0}{\partial \theta} \right) \Psi_j \right] - \left[\left(\frac{B\Omega}{2} \frac{\partial \Psi_i}{\partial \theta} - \mathbf{i}\omega \Psi_i \right) h_0 \Psi_j \right] \right\} r d\theta dr \tag{33.a}$$

$$q_{1_i}^e = \oint_{\Gamma^e} \Psi_i^e \dot{m}_1 \cdot \bar{\eta} \; d\Gamma^e \tag{33.b}$$

$$f_{1_i}^e = \iint_{\Omega^e} \left\{ P_0 \left[-\frac{3h_0^2}{12\mu} \left(\frac{\partial \Psi_i}{\partial r} \frac{\partial P_0}{\partial r} + \frac{1}{r^2} \frac{\partial \Psi_i}{\partial \theta} \frac{\partial P_0}{\partial \theta} \right) - \mathbf{i}\omega \Psi_i + \frac{B\Omega}{2} \frac{\partial \Psi_i}{\partial \theta} \right] r d\theta dr \right. \tag{33.c}$$

Note that P_0 in these equations is the zeroth-order discrete pressure field previously solved with the successive approximation approach at speed Ω. Like the zeroth-order finite element equations, the resulting algebraic system of first-order equations is also asymmetric. Storage of entire $\left[k_{ij}^e\right]$ matrices in both the zeroth- and first-order becomes necessary in this case, effecting much demand on computer memory.

As in the incompressible fluid analysis, the zeroth- and first-order pressures are integrated to obtain the load capacity and dynamic force coefficients, respectively, of compressible fluid *SGFSs*. The finite element method is again applied to solve the partial differential equations of pressure in a computer code written in FORTRAN90 within the WINDOWS NT operating system.

Parameters of importance in the analysis with compressible fluids are the speed number (Λ)

$$\Lambda = \frac{6\mu\Omega}{P_a}\left(\frac{R_o^2}{c^2}\right) \tag{34}$$

that describes the level of compressibility as a function of speed (Ω) for a given spiral grooved thrust bearing or seal geometry, and the frequency number (σ)

$$\sigma = 2\Lambda\left(\frac{\omega}{\Omega}\right) = \frac{12\mu\omega}{P_a}\left(\frac{R_o^2}{c^2}\right) \tag{35}$$

used to show the frequency dependence of the force coefficients.

NUMERICAL CONVERGENCE AND MESH DEPENDENCY

In using the successive approximation, convergence of this method to the solution of the pressure field becomes difficult considering that at a given successive approximation step, the new pressure field is based on the previous pressure field. The pressure field solutions may then oscillate between two contrasting pressure fields, each time reacting to the extreme density variation (or lack of) in the previous pressure field.

To hasten convergence, the successive approximation employs an under-relaxation parameter (a) in the following manner:

$$P_{o_{n+1}} = aP_n + (1-a)P_{o_n} \tag{36}$$

for a given step n of the successive approximation, where P_n is a vector containing the solution of the finite element equations calculated for step n. A typical value of the under-relaxation parameter (a) is 0.5 in the present work.

Mesh dependency in a given case must be closely observed from many aspects. When spiral angles approach either 0° or 180° grooves become exceptionally long since they verge on circumferential extension around the seal face. Thus, more elements in the radial direction are required with these cases lest the quadrilateral elements become ill conditioned from containing angles that are too obtuse (Reddy, 1993).

Seal dams also play an important role in determining face seal performance since flat-ungrooved regions help dissipate much of the pressure buildup from the grooves or due to the pressure ratio between the inner and outer diameter. When large pressure drops may occur radially, such as in the case of a face seal, more radial elements in this region can aid in predicting all of the pressure decrease across the seal dam.

The change in film thickness at the groove-ridge interface causes the fluid to contract, inducing a large pressure buildup and density changes (similar to a Rayleigh-step bearing). Higher rotational speeds greaten these effects. Consequently, the circumferential pressure drop over a groove-ridge pair occurs in the ridge region alone. A subsequent discussion will address this fact in more detail. Elements concentrated

circumferentially aid in fully and accurately accounting for the pressure drop in this region.

Note on Numerical Method of Solution

The successive approximation itself maintains many advantages and disadvantages. This method operates quickly within a relatively simple finite element Galerkin formulation with 4-noded quadrilateral elements. However, the price of not using higher order elements, such as in Bonneau, et al. (1993), is the need to refine the mesh (h-refinement) at higher speeds. When the speed number becomes very high oscillatory behavior in the calculated pressure field near the end of the ridge results due to film discontinuity and the large changes in density at this location. Discussing this in detail, Bonneau, et al. (1993) eliminated much of this problem through the use of upwinding and higher order elements (p-refinement) in the necessary locations. As a result, accurate solutions at much higher speeds become possible. In the present model, computations for load capacity may converge on a pressure field containing these fluctuations in the ridge region and give results that vary little with mesh refinement. However, the force coefficients are highly influenced by a refined mesh in these cases.

RESULTS AND DISCUSSION

INTRODUCTION

The need to validate the present analysis against published works arises both to ensure that predictions given by the model are correct and to indicate the advantages of the present research over that performed previously. The observation of previous findings also serves to identify topics of concern with thrust bearing and face seal configurations of this type. These topics become the focus of reported predictions from the present model.

VERIFICATION OF THE INCOMPRESSIBLE FLUID SGFS MODEL[†]

Comparison with Muijderman (1966). Muijderman (1966) provides analytical *NGT* solutions for *SGTBs* that operate with incompressible, isoviscous lubricants. In the model, pressure variation between grooves and ridges is simplified into an average, smoothed pressure. Additionally, the supposition that there is no radial (inward) flow arises since the thrust bearing configurations as studied by Muijderman (1966) have the inward pumping spiral groove thrust plate underneath a flat rotating thrust collar, thus contributing a pressure buildup at the inner diameter (rather than a specified inner diameter pressure) and an additional reaction load (due to the plenum pressure) generated within the inner diameter area of the thrust plate. A modified version of

[†] Characteristic values for making parameters dimensionless are provided in Appendix A while specific geometry and FEM parameters reside in Appendix B.

spiral.for (incompressible fluid) restricts the flow rate at the inner diameter to zero to enable comparison. (A sample calculation of the pressure and load calculations according to Muijderman (1966) can be found in Appendix C.) The results of the comparisons between the *NGT* and present *FEM* computations for dimensionless optimum load capacity $(\overline{W})$ as the radius ratio ($R = R_i/R_o$) increases are shown in Figure 3. Each point in the figure represents the conditions for maximum load capacity as given in Muijderman (1966), and the dimensionless parameters are provided for each case. Note that the total load capacity is the sum of the hydrodynamic load generated by the grooves and the load from the pressure buildup within the inner diameter ($\pi R_i^2 P_i$). Although comparisons are very close, the *NGT* tends to slightly overpredict the load capacity of the *SGTB*, a fact well reported in the literature.

As well as providing analytical calculations for load capacity, Muijderman (1966) gives an estimation of the mean inner diameter pressure using the *NGT*. The actual pressure variations between grooves and ridges as calculated by the *FEM* program is given in Figure 4 with *NGT* pressure calculations included. As expected, the variation in pressure is large for smaller numbers of grooves. As the number of grooves nears infinity (~50), the pressure variation is practically negligible.

Dimensionless dynamic force coefficients are given in Figure 5 for the same geometries. As shown, the stiffness $\left(\overline{K}_{zz}\right)$ remains virtually constant while the damping

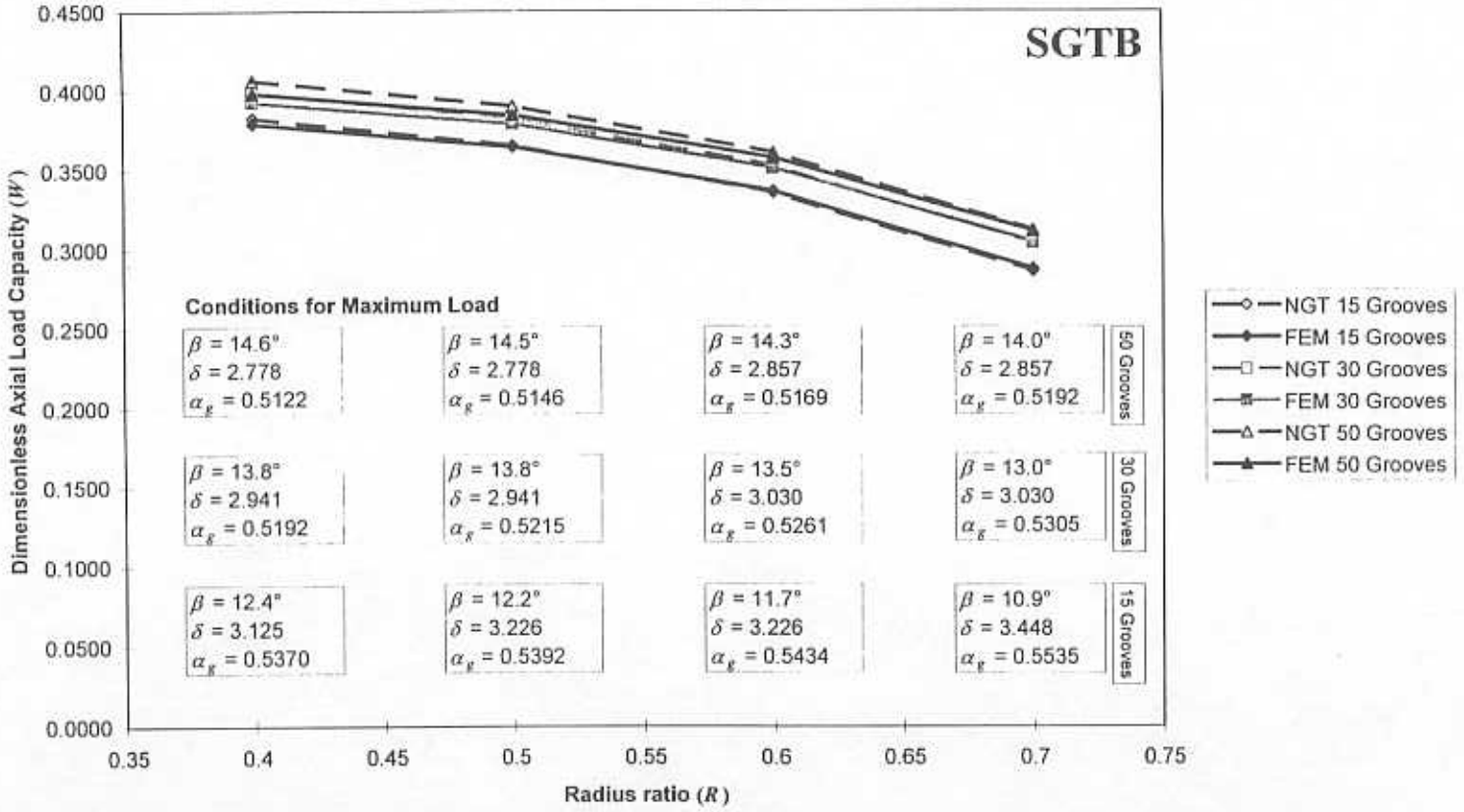

Fig. 3 Comparisons of the *NGT* with present *FEM* results for dimensionless load capacity.

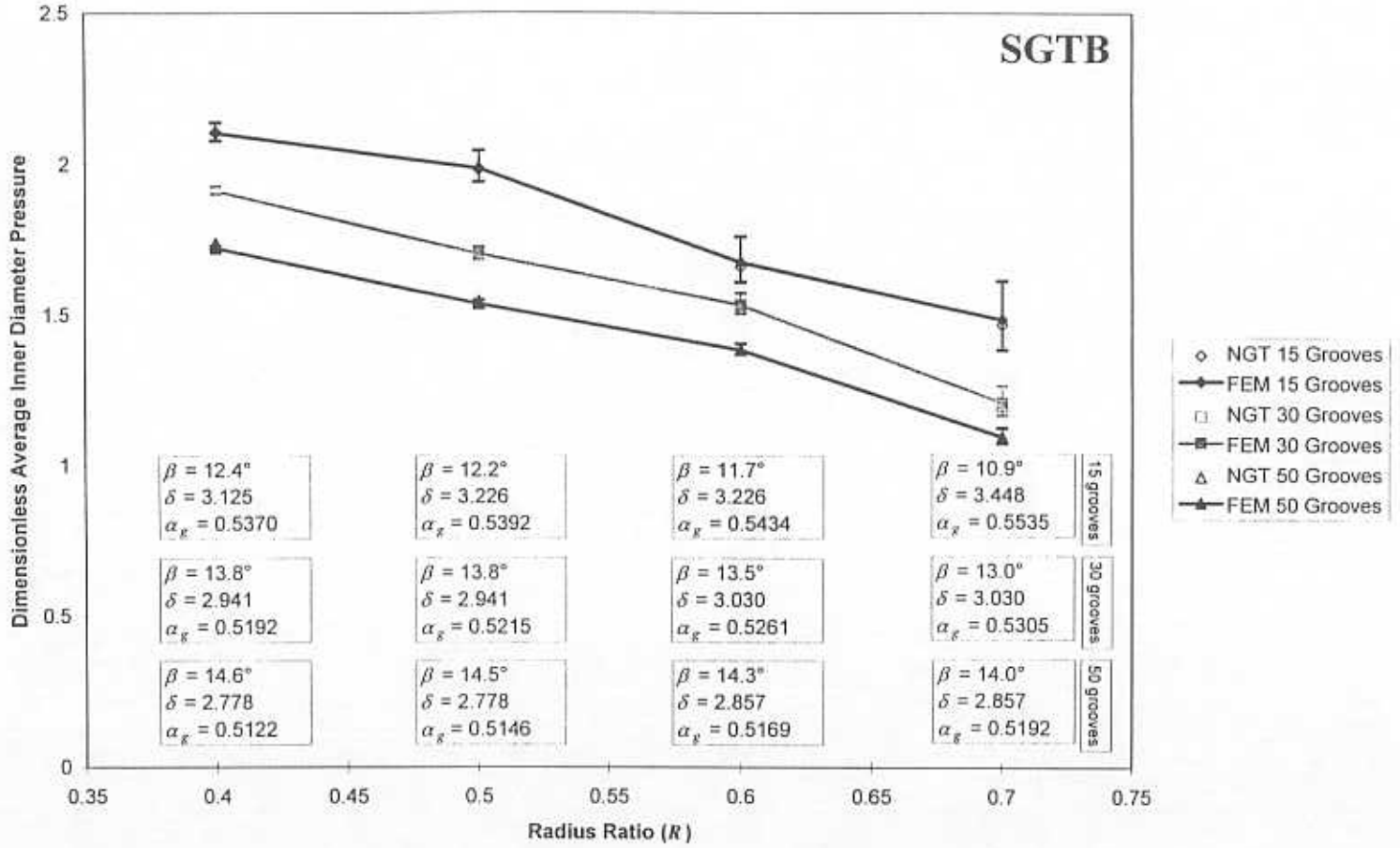

Fig. 4 Calculated inner diameter pressures with variations provided by the *FEM* analysis.

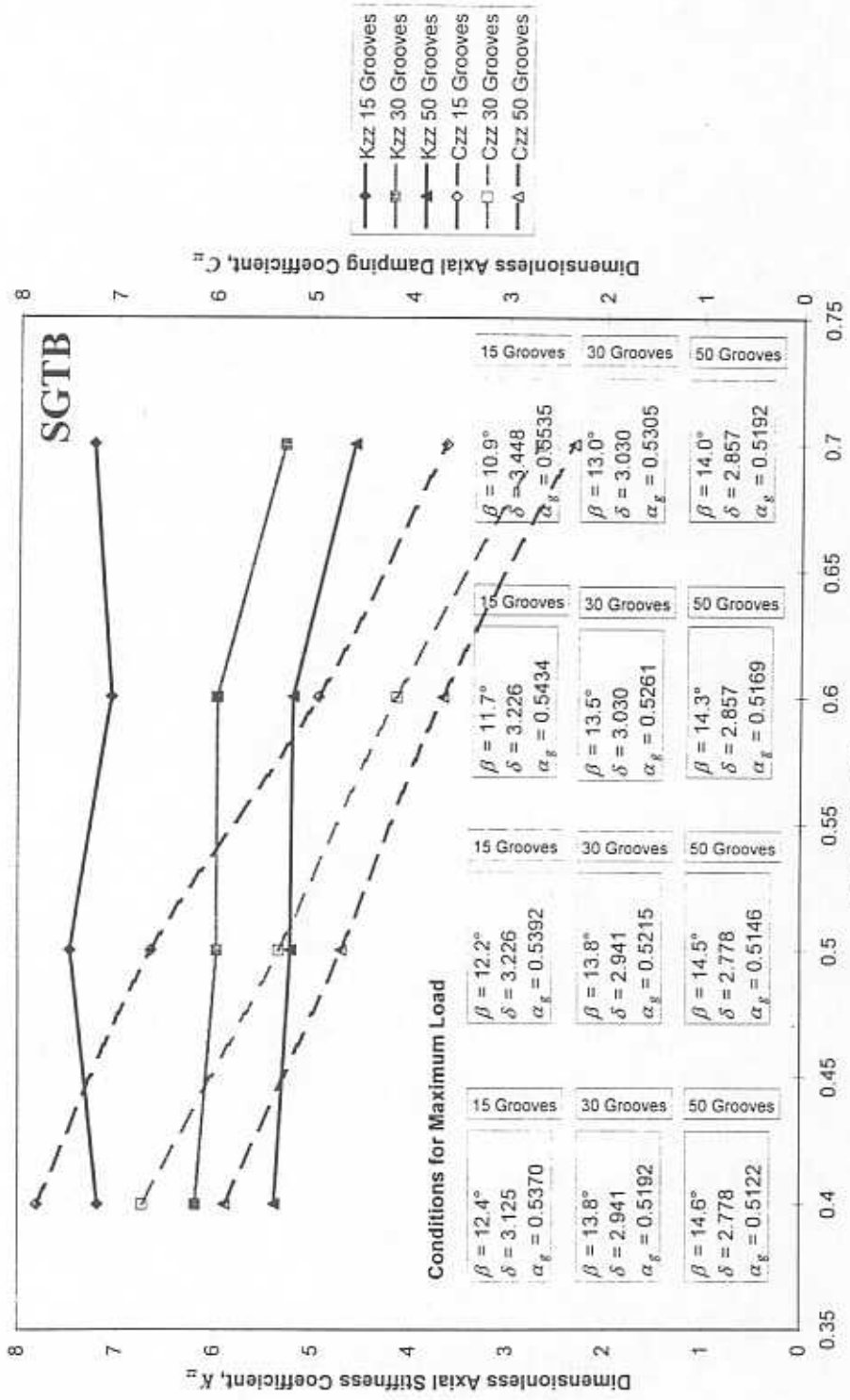

Fig. 5 Dimensionless force coefficients for increasing radius ratios.

coefficients $\left(\overline{C}_{zz}\right)$ decrease as the radius ratio increases, indicating that using narrower thrust bearing plates may be an undesirable practice. A smaller number of grooves is preferred since the thrust bearing exhibits more stiffness and damping as the number of grooves decreases.

Comparison with Someya (1989). Figure 6 presents comparison of the present *FEM* analysis against *FEM* calculations of dimensionless eccentricity ($\varepsilon_z = 1 - c/c_g$) as the Sommerfeld number $S\ \left(=\mu N\pi R_o^2\left(R_o/c_g\right)^2/W\right)$ increases given in Someya (1989) for *SGTBs* with pressure dams on the inner diameter. As defined, the Sommerfeld number (S) represents the inverse of load (W) while the inverse of the ridge (minimum) clearance (c) is designated by the eccentricity (ε_z). The trends show that as the load increases (decreasing S) the ridge clearance decreases (increasing ε_z). Comparisons give very little discrepancy with an average difference of 5.75%.

Parametric Study of Incompressible Fluid Spiral Groove Face Seals

Introduction. Variation of the dimensionless force coefficients, leakage rate, and power loss with changes in the *SGFS* geometry is given in Figures 7 through 11. Table 1 shows how the geometry varies in each case. Although the analysis used to compute the results is for incompressible fluids only, nitrogen gas was used in these cases at low speed numbers ($\Lambda < 6$), where this gas acts as an incompressible fluid. These cases are distinct from those presented by Muijderman (1966) since there exists a pressure differential

Table 1. Parametric study variations for *SGFSs* operating with an incompressible fluid.

Variation	N_g	β [°]	l	α_g	δ
Figure 7. Number of grooves (N_g)	$6 \rightarrow 18$	20	0.48	.5	2
Figure 8. Groove angle (β [°])	12	$10 \rightarrow 30$	0.48	.5	2
Figure 9. Seal dam extent (l)	12	20	$0 \rightarrow 0.64$	.5	2
Figure 10. Groove width ratio (α_g)	12	20	0.48	$0.45 \rightarrow 0.65$	2
Figure 11. Groove depth ratio (δ)	12	20	0.48	.5	$2 \rightarrow 3$

Fixed parameters: (Rotating grooves)	*Fluid properties:*
$D_o = 0.0762$ m	$\rho = 1.1233$ kg/m^3
$D_i = 0.0381$ m	$\mu = 1.782 \times 10^{-5}$ Pa·s
$R = 0.5$	$P_o = 517.1$ kPa
$c = 4$ μm	$P_i = 101.3$ kPa
$\Omega = 2000$ RPM	
$\Lambda = 3.951$	

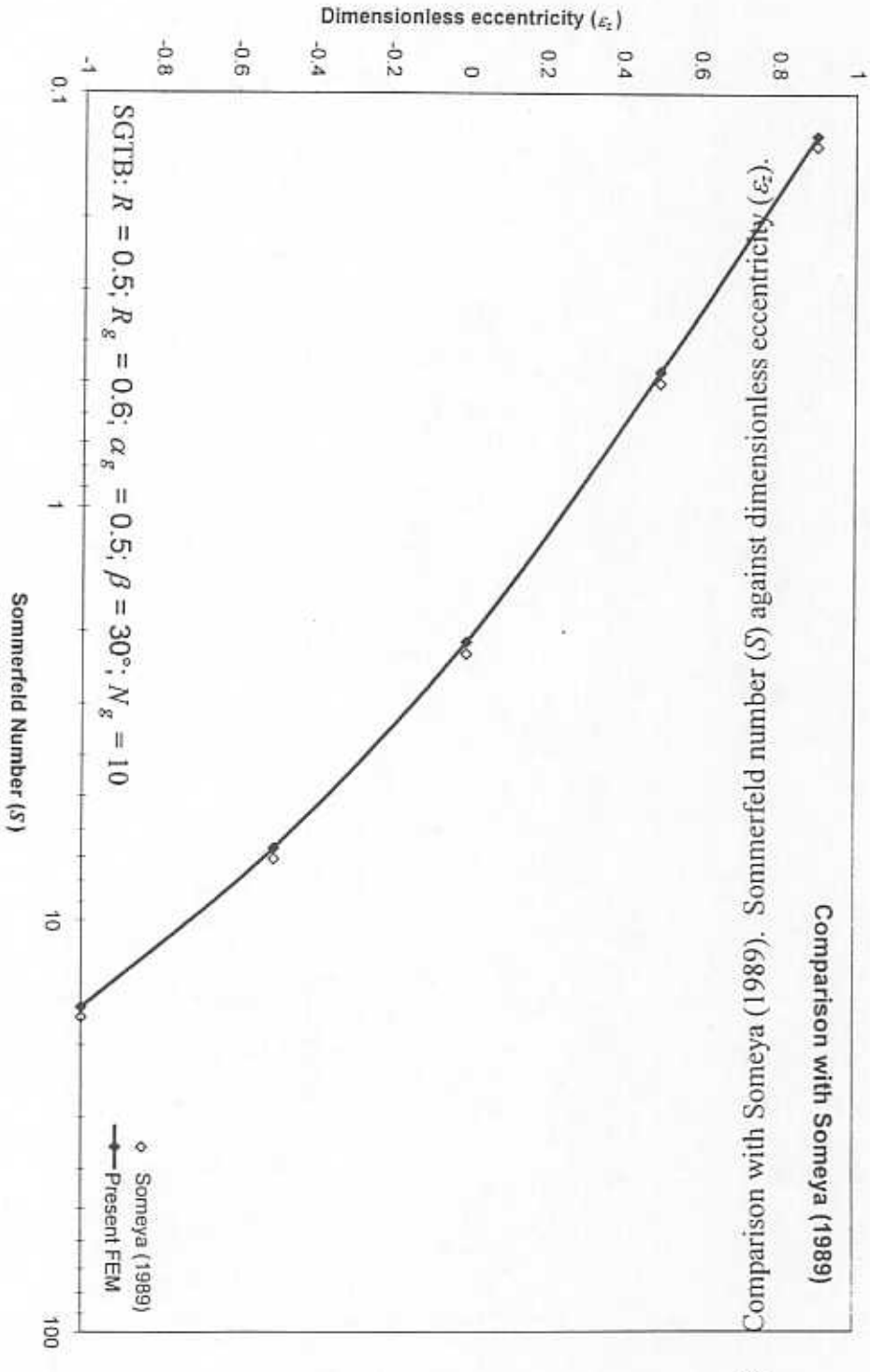

Fig. 6 Comparison with Someya (1989). Sommerfeld number (S) against dimensionless eccentricity (ε_z).

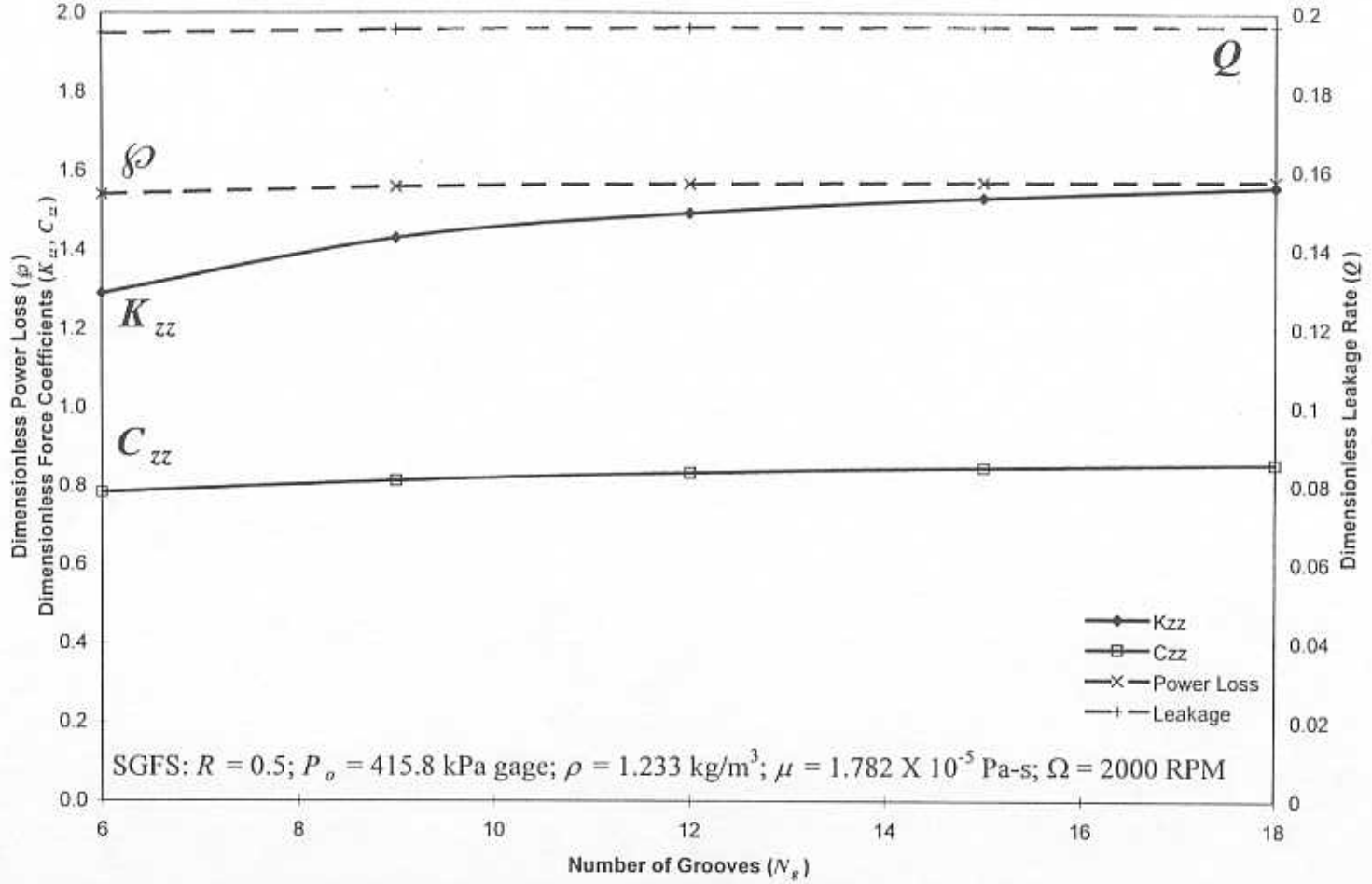

Fig. 7 Variation of force coefficients, leakage rate, and power loss with the number of grooves (N_g).

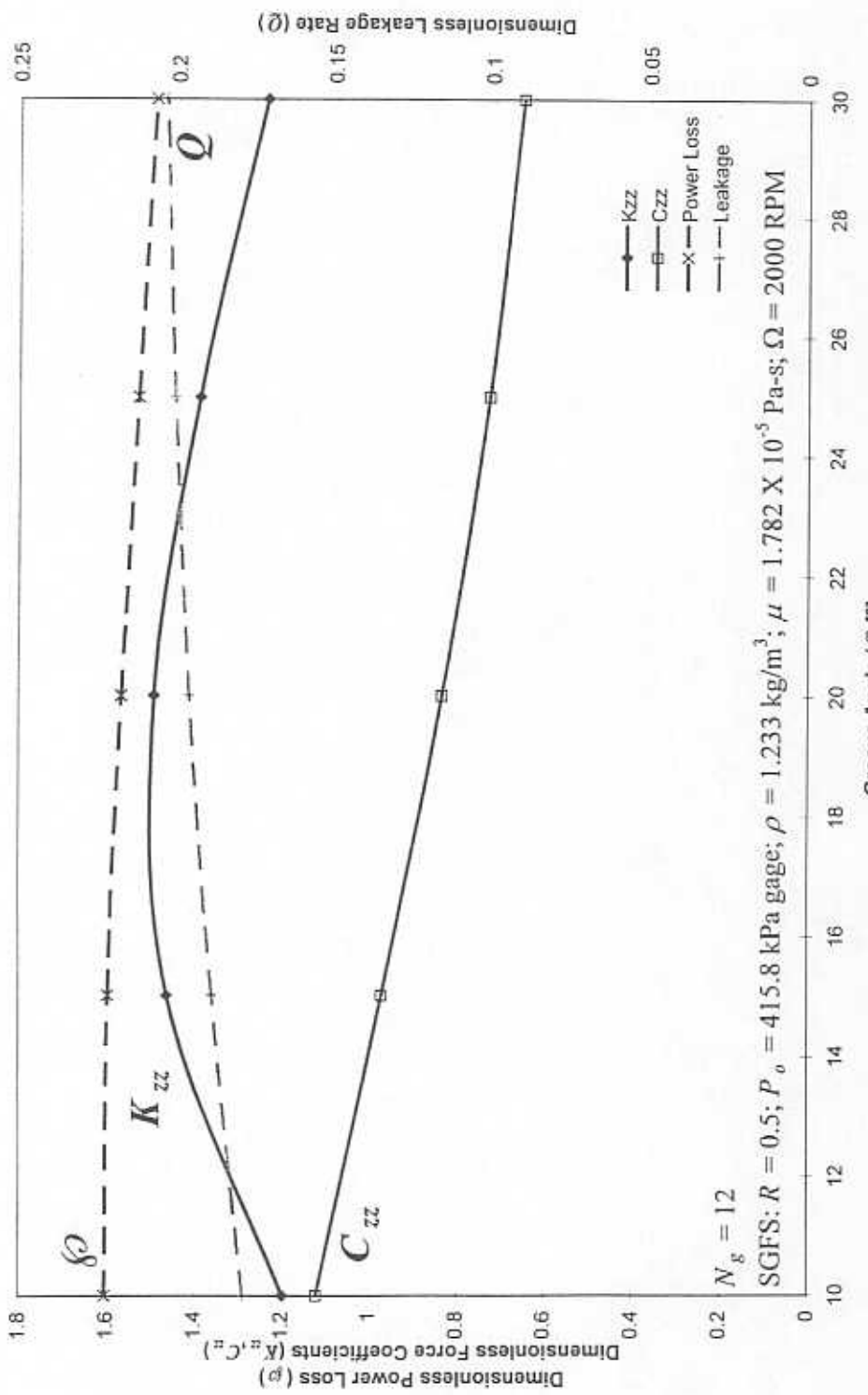

Fig. 8 Variation of force coefficients, leakage rate, and power loss with groove angle (β).

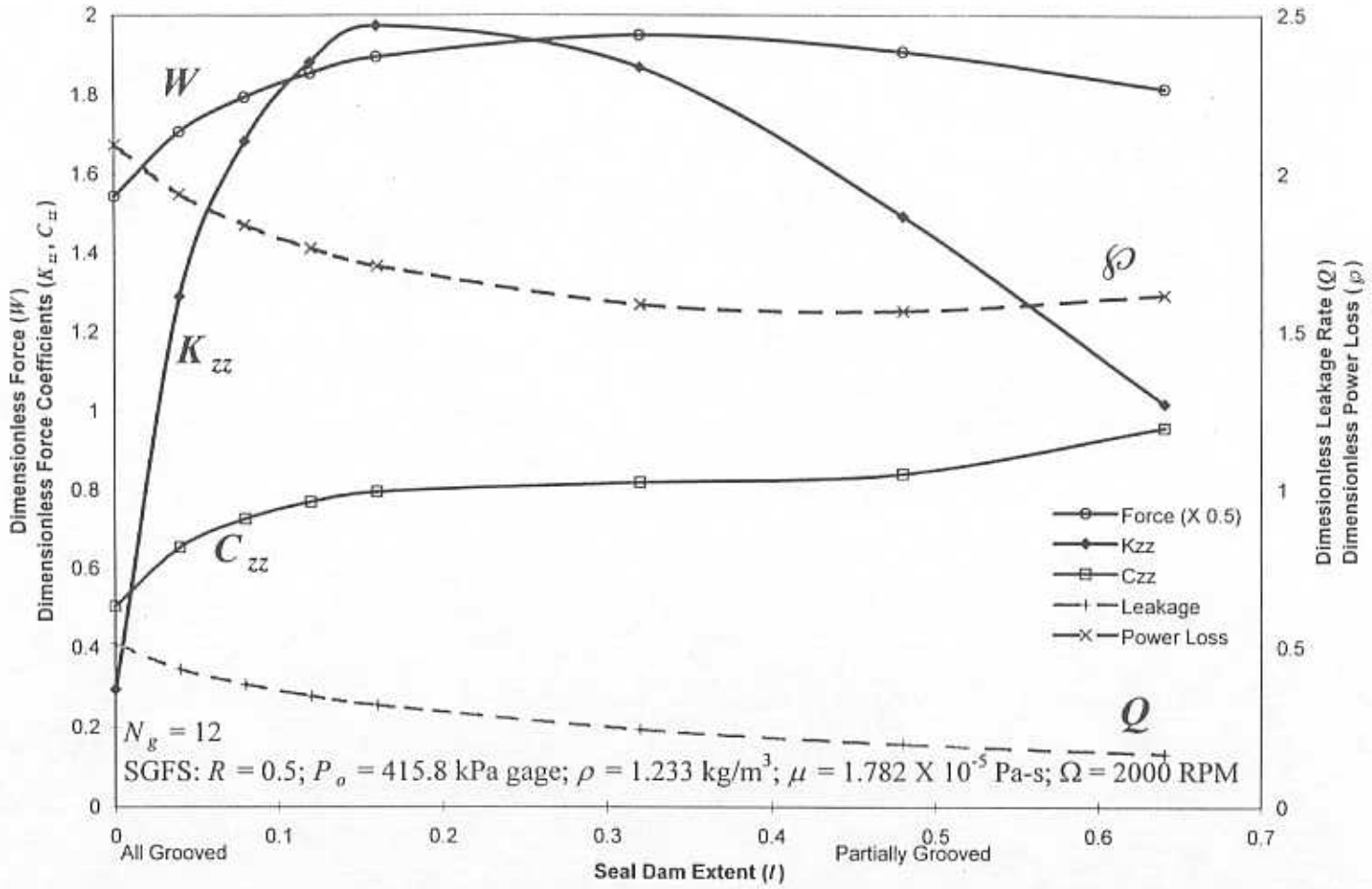

Fig. 9 Variation of the opening force, force coefficients, leakage rate, and power loss with the seal dam radial extent (l).

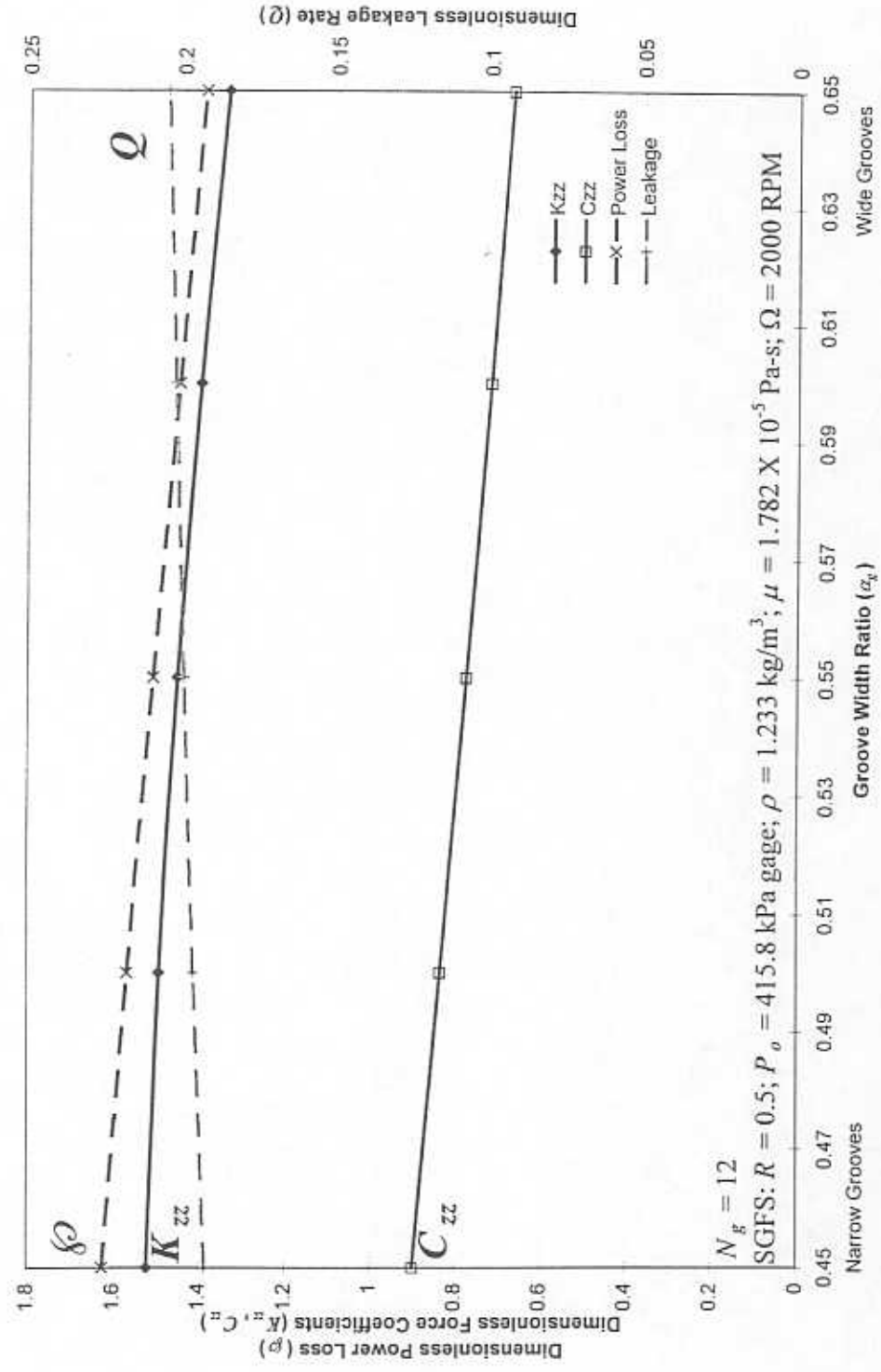

Fig. 10 Variation of the force coefficients, leakage rate, and power loss with the groove width ratio (α_g).

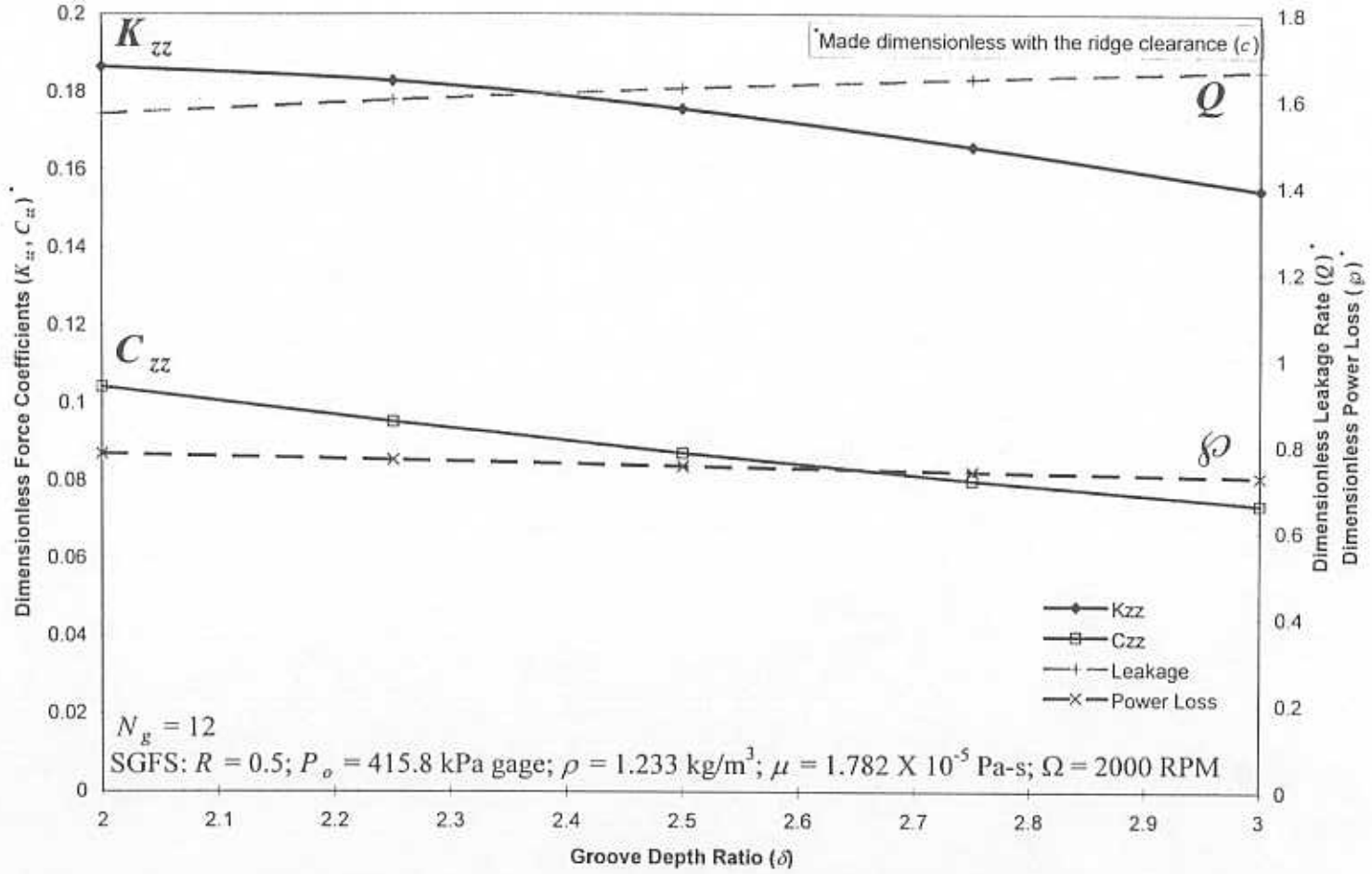

Fig. 11 Variation of the force coefficients, leakage rate, and power loss with the groove depth ratio (δ).

from the outer to inner diameter, i. e., $P_o > P_i$. It should be noted in the figures that the dimensionless leakage rate $\left(\overline{Q} = Q/Q_*\right)^{\ddagger}$ is generally 20% of the leakage between two flat plates with the same order of clearance. These results attest to the obvious advantage of grooved geometries over conventional non-grooved configurations.

Effect of the Number of Grooves (N_g). As the number of grooves (N_g) increases in Figure 7, the stiffness and damping coefficients $\left(\overline{K}_{zz}, \overline{C}_{zz}\right)$ and the power loss $\left(\overline{\wp}\right)$ increase slightly while the leakage rate $\left(\overline{Q}\right)$ remains constant. The opening force (not shown) does not change with an increase in the number of grooves (N_g).

Effect of the Spiral Groove Angle (β). Figure 8 shows that the stiffness coefficient $\left(\overline{K}_{zz}\right)$ reaches a maximum at a groove angle (β) of 20° while the damping coefficient $\left(\overline{C}_{zz}\right)$ and power loss $\left(\overline{\wp}\right)$ decrease as the groove angle (β) increases. The leakage rate $\left(\overline{Q}\right)$ increases slightly as the groove angle (β) increases. When the groove angle approaches radial grooves ($\beta \rightarrow 90°$), less seal area exists over which the pressure can develop, and the grooves do not pump fluid outward as well, explaining the drop in stiffness and increase in leakage at higher groove angles (β). On the other hand, grooves that are nearly tangential ($\beta \rightarrow 0°$) do not develop pressure efficiently.

---

‡ Q_* is the flow rate for two flat plates having the same dimensions as the SGFS with clearance c_g.

Effect of the Seal Dam Extent (l). A relatively small seal dam (with ridge clearance, c) on the inner diameter significantly influences the behavior of *SGFSs* as shown in Figure 9. The opening force $(\overline{W})$, direct stiffness coefficient $(\overline{K}_{zz})$, and damping coefficient $(\overline{C}_{zz})$ increase significantly with the introduction of a seal dam. The direct stiffness coefficient reaches a maximum value at a seal dam extent (l) of 0.18 (18% of the seal radial width) and falls as the seal dam extends over more of the seal face. The leakage rate $(\overline{Q})$ drops somewhat with increasing seal dam extent (l) while the power loss $(\overline{\wp})$ significantly lowers only until a seal dam extent (l) of 0.3. Since the seal dam has the same clearance as the ridge (minimum) film clearance (c), a more extensive seal dam represents a reduction in the average film clearance over the entire seal. Thus, the stiffness coefficient $(\overline{K}_{zz})$ and opening force are expected to increase as the grooved extent increases, and the leakage $(\overline{Q})$ should increase. With less grooved area to pump fluid outward, the stiffness coefficient $(\overline{K}_{zz})$ decreases when the seal dam becomes too large compared to the grooved part of the seal.

Effect of the Groove Width Ratio (α_g). Changes in the groove width ratio (α_g), given in Figure 10, do not significantly change the seal parameters of interest, although the leakage rate $(\overline{Q})$ does increase slightly as the groove width ratio (α_g) increases. Again, this effect can be illustrated by the general increase in the seal average clearance.

Effect of the Groove Depth Ratio (δ). Figure 11 shows the effect of increasing the groove depth ratio (δ). Since the definitions of the dimensional parameters depend on the groove depth (c_g), the parameters were made dimensionless using the ridge clearance (c), which is held constant, rather than the groove depth (c_g), as in all other cases. Thus, trends of the dependent dimensionless parameters are preserved. The stiffness $\left(\overline{K}_{zz}\right)$ and damping $\left(\overline{C}_{zz}\right)$ coefficient decrease with the groove depth ratio while the leakage rate $\left(\overline{Q}\right)$ increases. The dependence of the parameters on the groove depth can be generally inferred by realizing that an increase in the groove depth ratio (δ) represents an increase in the average seal clearance. The power loss $\left(\overline{\wp}\right)$ remains nearly constant with the groove depth ratio.

Verification of the Compressible Fluid SGFS Model

Comparison with Lebeck (1991). Several case studies given in Lebeck (1991) serve to confirm the compressible fluid model for spiral groove face seals, and Table 2 provides the dimensionless geometry for each case. Lebeck (1991) applies the equations given in Muijderman (1966) to *SGFSs* with specified inner and outer radius pressures and accounts for fluid compressibility by considering an isentropic relationship ($P \propto \rho^{1.4}$). As well as predicting load capacity and leakage rate, Lebeck (1991) employs a finite film

Table 2. Geometry for Lebeck (1991) *SGFS* case studies. $P_{rat} = 19.8$.

Case No.	*Groove Angle* β [°]	*Groove Width Ratio* (α)	Radius Ratio (R)	*Seal Dam Extent* (l)	*Groove Depth Ratio* (δ)	*Speed No.* (Λ)
1	20	0.500	0.8727	0.3	1.5	160.9
2	10	0.500	0.8727	0.3	1.5	160.9
3	30	0.500	0.8727	0.3	1.5	160.9
4	20	0.333	0.8727	0.3	1.5	160.9
5	20	0.667	0.8727	0.3	1.5	160.9
6	20	0.500	0.9300	0.3	1.5	133.0
7	20	0.500	0.8250	0.3	1.5	191.5
8	20	0.500	0.8545	0.2	1.5	160.9
9	20	0.500	0.8909	0.4	1.5	160.9
10	20	0.500	0.9273	0.6	1.5	160.9
11	20	0.500	0.8727	0.3	1.0	160.9
12	20	0.500	0.8727	0.3	2.0	160.9

Number of grooves (N_g) of 80 used in FEM analysis.

thickness perturbation to obtain static[§] axial stiffness coefficients. Figure 12 shows comparisons of the dimensionless load capacity $(\overline{W})$ from the present analysis to be in good agreement with those of Lebeck (1991). The same assertion holds for the dimensionless static stiffness coefficients $(\overline{K}_{zz})$ and leakage rate $(\overline{Q})$ given in Figures 13 and 14, respectively. Discrepancies most likely arise from differences between the simple *NGT* and present *FEM* solution. The fact that the two analyses use different pressure/density relationships (isentropic vs. isothermal gas) may also account for some of the disparity.

Comparison with James and Potter (1967) and Bonneau, et al. (1993). Comparison of the present *FEM* model with results from the finite difference solution given by James and Potter (1967) as well as the upwinding *FEM* model derived in Bonneau, et al (1993) occurs in Figure 15 for load capacity in *SGTBs* with inner radial flow as the pressure ratio between the inner and outer diameter (P_i/P_o) varies and for a speed number (Λ) of 175.7. The previous models tend to underpredict the load capacity although all trends predicted are virtually identical. The present model converges to the same results provided by James and Potter (1967) as the pressure ratio (P_i/P_o) tends to unity. Discrepancies may lie in the fact that the operating conditions and geometry were difficult to ascertain from the original example given in James and Potter (1967).

[§] Static implies dynamic axial perturbations at very low excitation frequencies, i. e. $\omega \to 0$ $(\sigma \to 0)$.

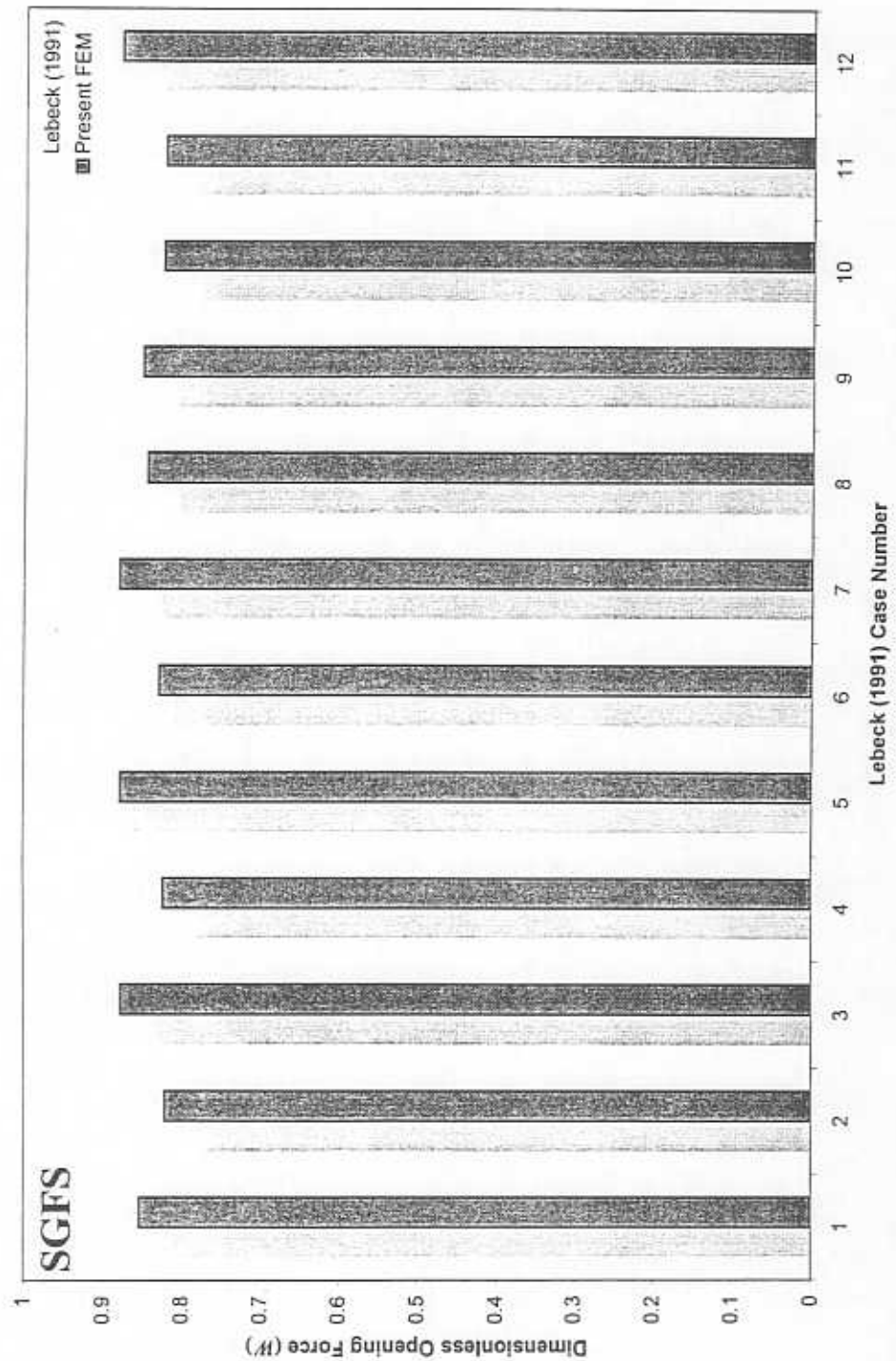

Fig. 12 Comparison with Lebeck (1991) case studies. Opening force.

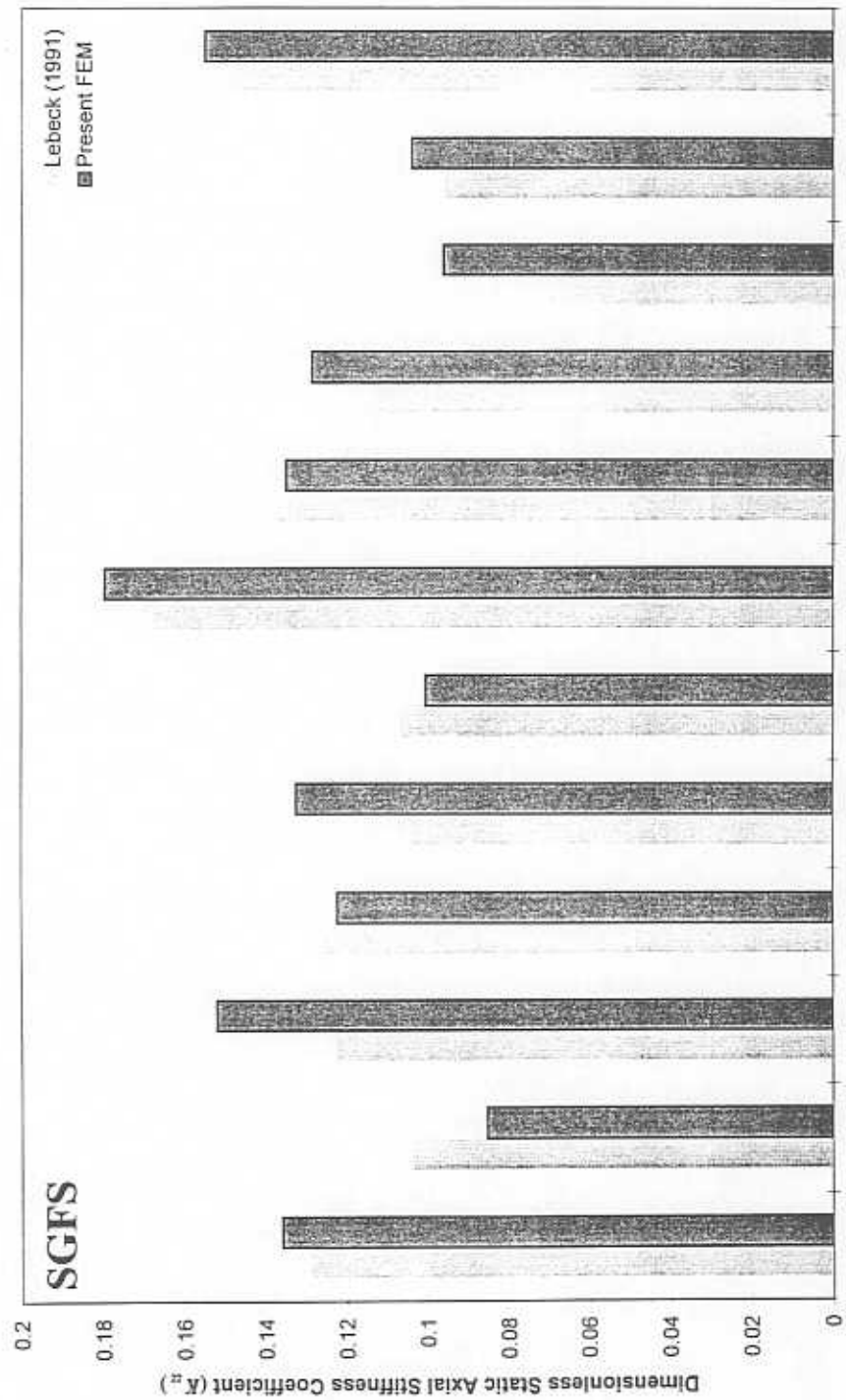

Fig. 13 Comparison with Lebeck (1991) case studies. Static axial stiffness coefficient.

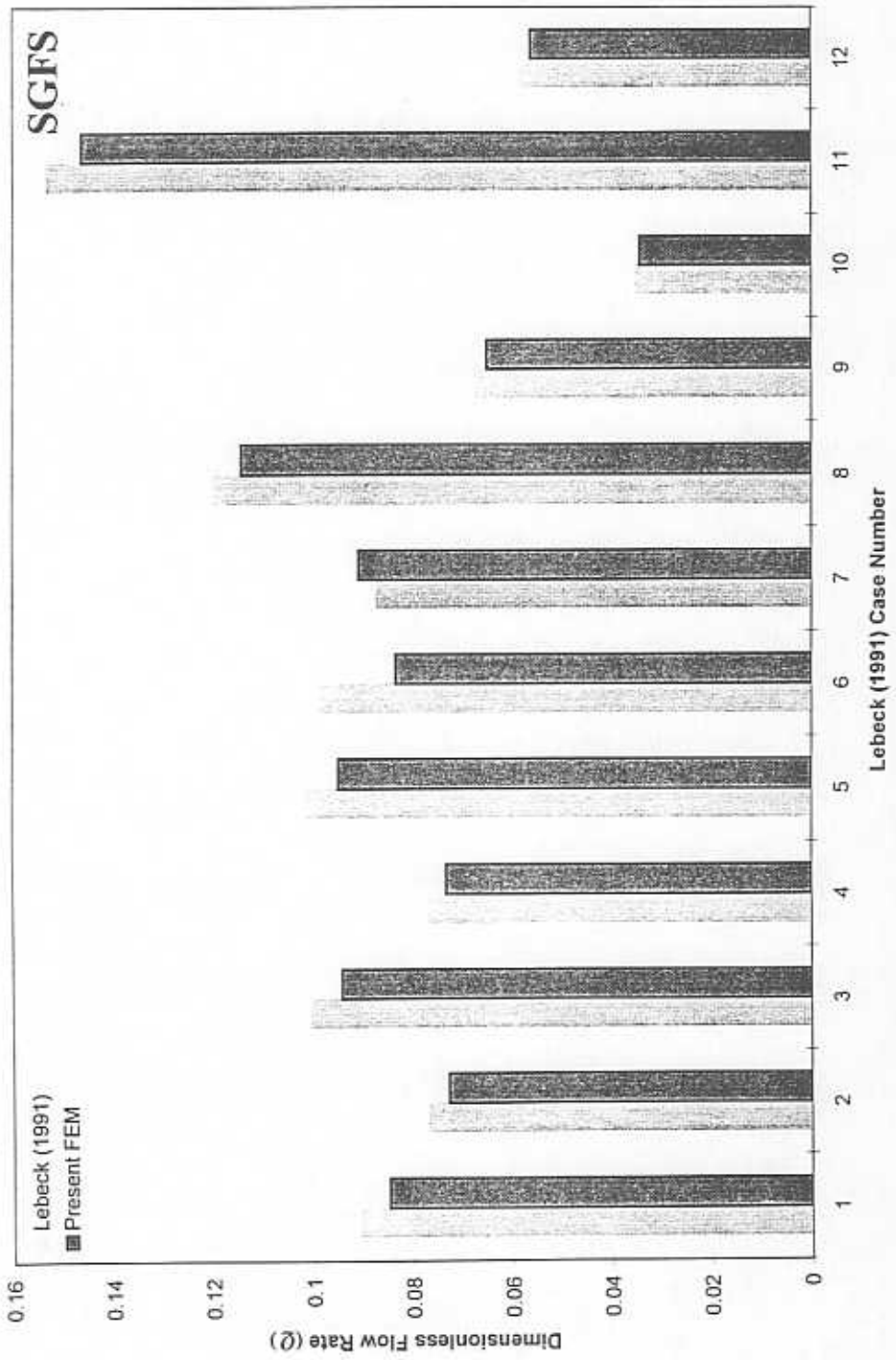

Fig. 14 Comparison with Lebeck (1991) case studies. Leakage rate.

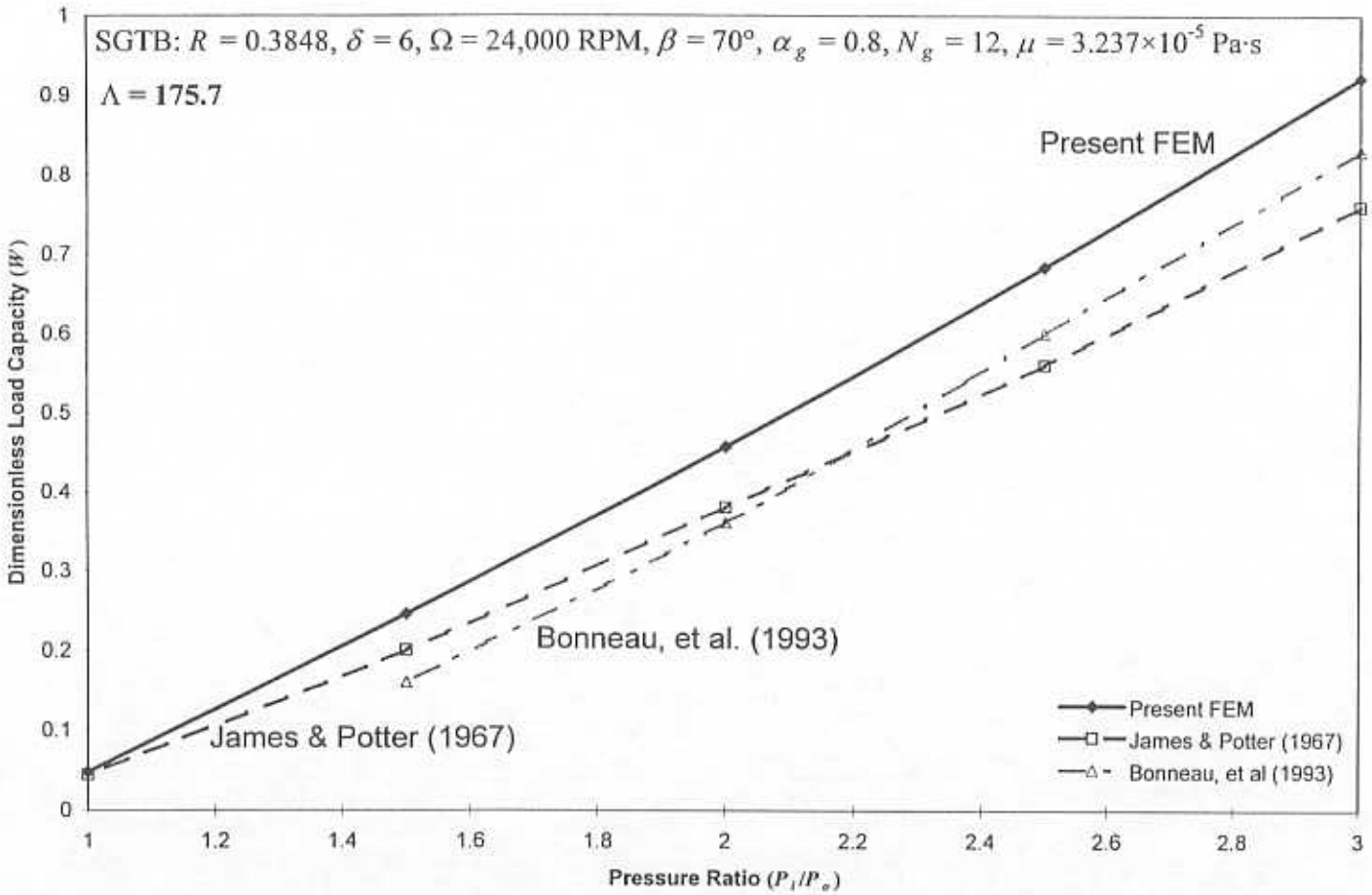

Fig. 15 Comparison with James and Potter (1967) and Bonneau, et al. (1993). Load capacity as the pressure ratio increases.

Comparison with Malanoski and Pan (1965). Using the *NGT* for compressible fluids, Malanoski and Pan (1965) examine the *SGFS* load capacity as well as frequency dependent dynamic axial stiffness and damping coefficients. Figure 16 shows the dimensionless load capacity $\left(\overline{W}\right)$ and static (zero frequency) axial stiffness coefficients $\left(\overline{K}_{zz}\right)$ versus speed number (Λ) to compare well with those of Malanoski and Pan (1965). Both analyses show virtually constant dimensionless load capacity and static axial stiffness except at high speed numbers (Λ) where each parameter drops slightly. Since the characteristic load is directly proportional to the speed number (Λ), this decrease suggests the considerable effect of compressibility as each dimensional parameter reaches an asymptotic upper limit.

Figures 17 and 18 clearly demonstrate the dramatic behavior of the dynamic force coefficients with variable axial excitation frequency numbers (σ) for three different speed numbers (Λ). In general, the force coefficients remain constant at low excitation frequencies (σ) implying that the fluid is incompressible. At high excitation frequency numbers (σ), compressibility largely affects the dynamic *SGFS* performance.

The dimensionless stiffness coefficient $\left(\overline{K}_{zz}\right)$, shown in Figure 17, rises with increasing axial excitation frequency (σ) for the lowest speed number ($\Lambda = 2$), representing a nearly incompressible fluid model. The stiffness coefficient $\left(\overline{K}_{zz}\right)$ remains almost constant with excitation frequency (σ) for moderate speed numbers ($\Lambda = 20$), while at the largest speed number ($\Lambda = 100$), the stiffness coefficient $\left(\overline{K}_{zz}\right)$ decreases

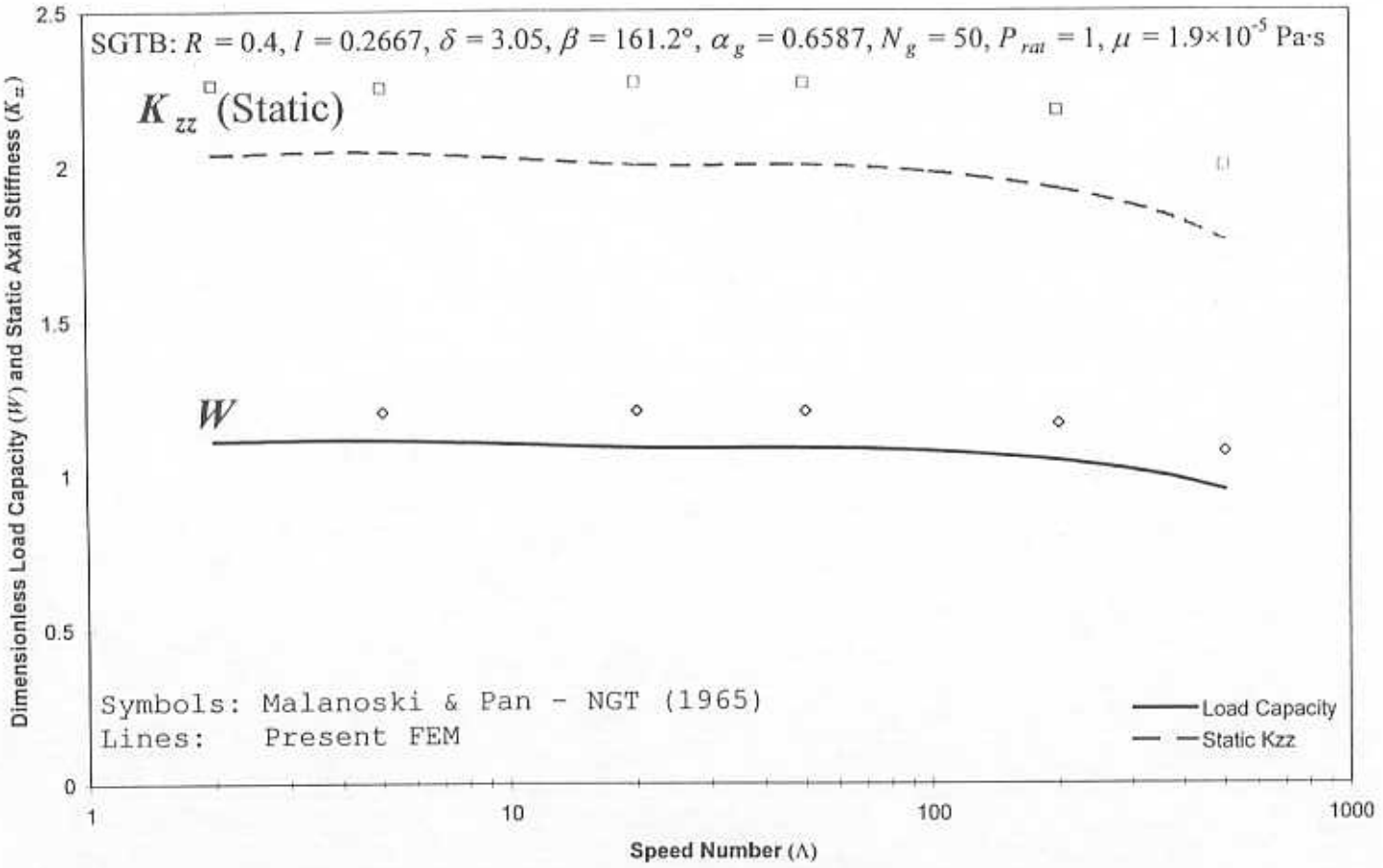

Fig. 16 Comparison with Malanoski and Pan (1965). Load capacity for increasing speed number (Λ).

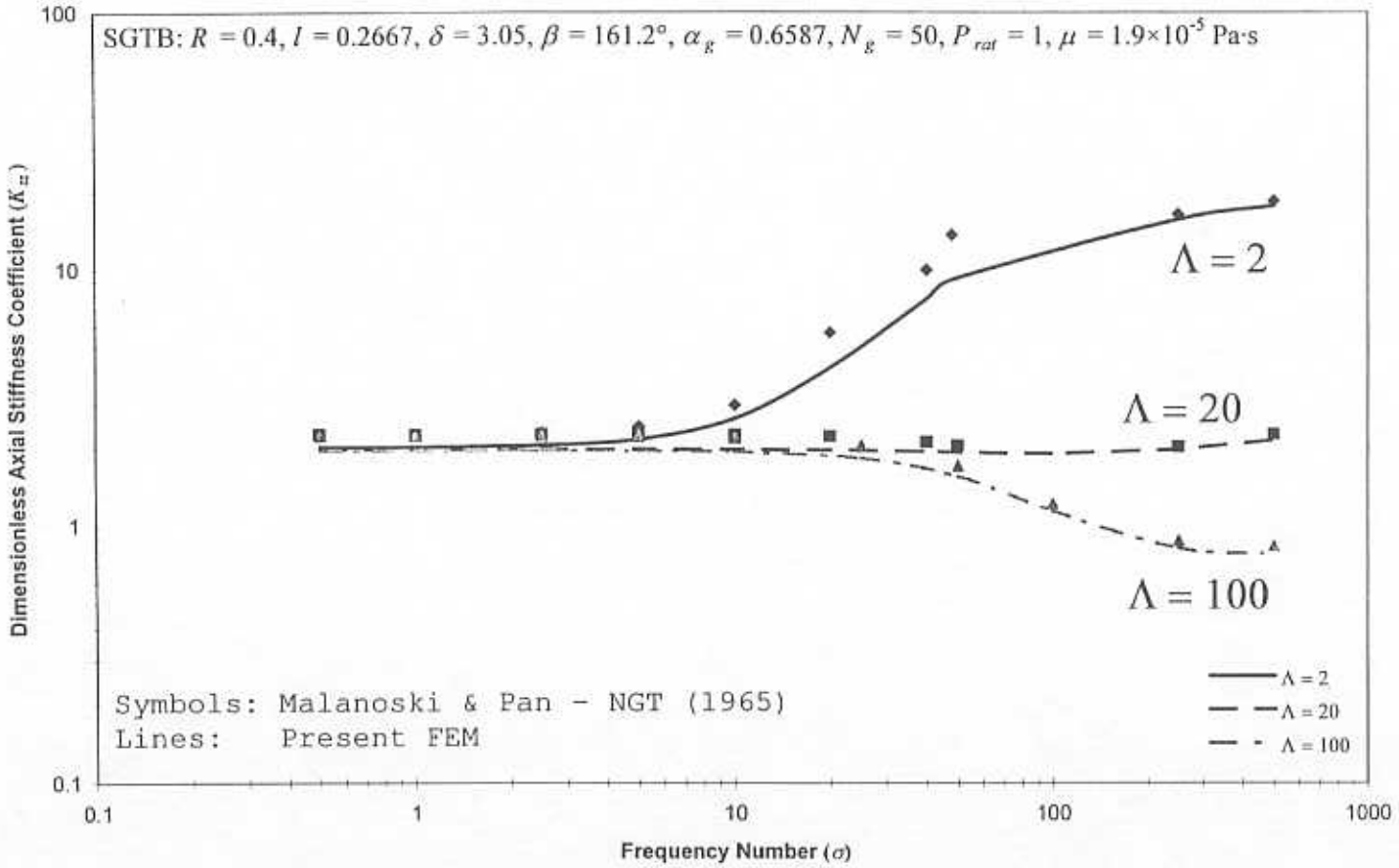

Fig. 17 Comparison with Malanoski and Pan (1965). Variation of the axial stiffness coefficient with excitation frequency (σ) for three speed numbers (Λ).

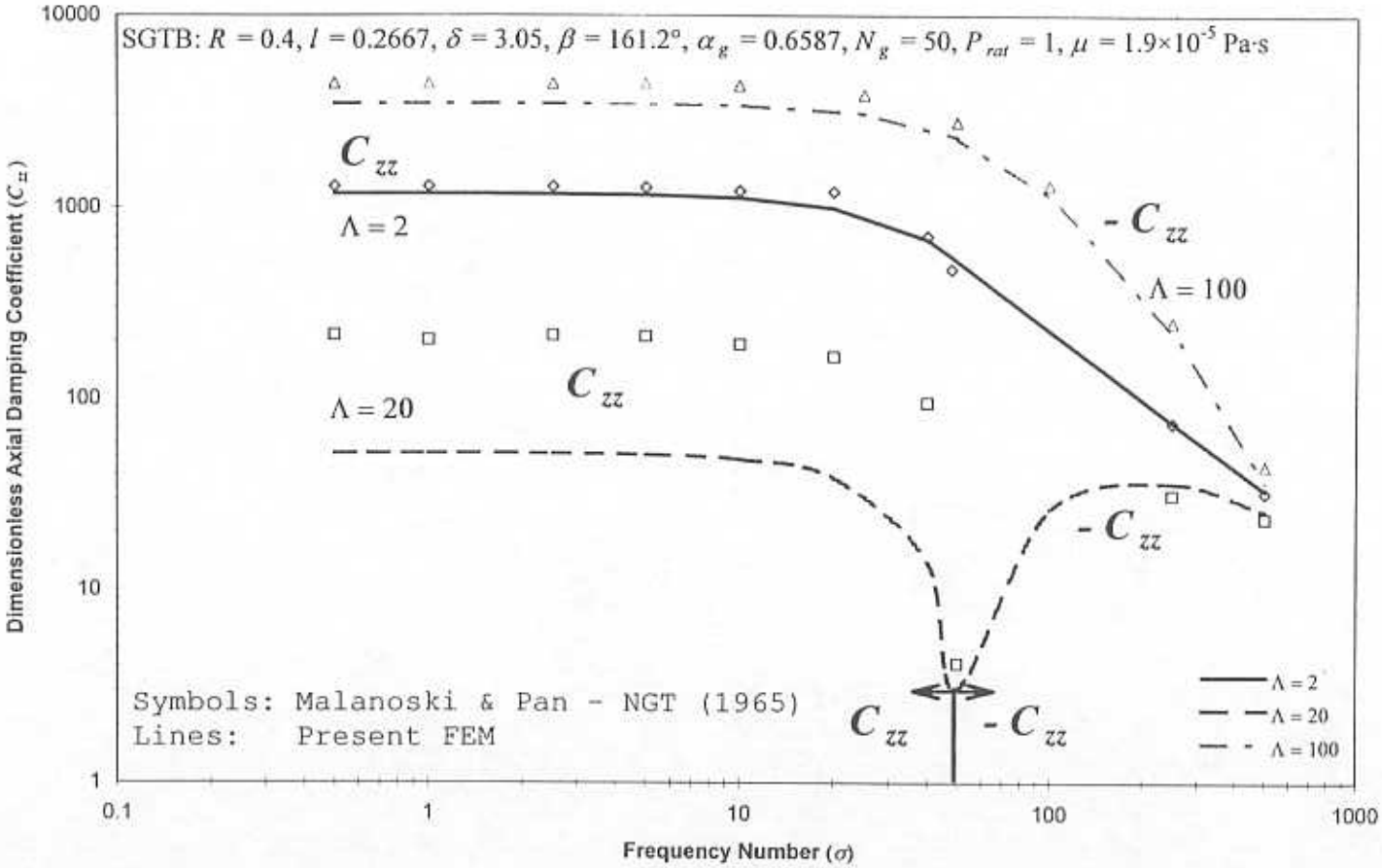

Fig. 18 Comparison with Malanoski and Pan (1965). Variation of the axial damping coefficient (absolute value) with excitation frequency (σ) for three speed numbers (Λ).

with excitation frequency (σ). For low excitation frequency numbers (σ), the stiffness coefficients tend toward the same value regardless of speed number (Λ). The damping coefficients $\left(\overline{C}_{zz}\right)$, plotted in Figure 18 as absolute values, drop at high excitation frequencies for the nearly incompressible fluid case ($\Lambda = 2$). Thrust bearing instability, predicted by negative axial damping $\left(\overline{C}_{zz}\right)$ at moderate excitation frequencies ($\sigma > 50$), occurs for moderate compressibility ($\Lambda = 20$). The damping $\left(\overline{C}_{zz}\right)$ remains negative throughout the range of excitation frequencies (σ) for the highest value of speed number ($\Lambda = 100$), i.e. with large fluid compressibility effects. Note that the damping $\left(\overline{C}_{zz}\right)$ shows variation in orders of magnitude as the speed number (Λ) increases. At low speed numbers (Λ), the stiffness $\left(\overline{K}_{zz}\right)$ increase with high excitation frequencies (σ) is accompanied by a drop in damping $\left(\overline{C}_{zz}\right)$; while at high speed numbers (Λ), stiffness $\left(\overline{K}_{zz}\right)$ decreases and damping $\left(\overline{C}_{zz}\right)$ is negative.

Comparisons between the two models prove relatively close considering the differences in the two numerical models and the limited treatment of fluid compressibility in Malanoski and Pan (1965). This example cautions the use of *SGTBs* at high speeds due to predicted instability from null or negative damping $\left(\overline{C}_{zz}\right)$, especially at low excitation frequencies (σ).

Parametric Study of Compressible Fluid Spiral Groove Face Seals

Introduction. A parametric study for compressible fluid *SGFSs* helps ascertain an optimum face seal geometry and the resulting static and dynamic face seal behavior, acting as design tool and benchmark for *SGFS* performance. The baseline geometry and its variation are given in Table 3. The lack of published experimental data prevents comparison of the present model with experiments. Furthermore, manufacturers, reluctant to release information obtained in their own research facilities, refuse to provide even the most basic information about *SGFS* geometries presently in use. Thus, the present baseline geometry is derived from the example given in Lebeck (1991).

This baseline example represents a narrow width *SGFS* ($R = 0.8$) having twelve grooves with a inner diameter seal dam extending over 30% of the seal width ($l = 0.3$). The pressure ratio (P_{rat}) of nearly 20 ($P_{rat} = 19.8$) represents a large pressure drop across a typical gas face seal. The groove parameters are set to previously published values for this type of seal configuration (groove angle: $\beta = 20°$; groove width ratio: $\alpha_g = 0.5$; groove depth ratio: $\delta = 2$).

The choice of optimum parameters is very dependent on the particular *SGFS* application, thus the following study primarily represents a design tool from which expected *SGFS* behavior can be derived. In the present work, optimum geometric parameters are chosen to provide a combination of both static and dynamic performance characteristics with emphasis placed on obtaining higher values of stiffness and damping while minimizing seal leakage.

Table 3. Parametric study variations for *SGFSs* operating with air (ideal gas).

Variation	σ	N_g	β [°]	α_g	l	δ	P_{rat}	R
Figure 19. Number of grooves (N_g). Λ = 160.9, 321.8.	≈ 0	$6 \rightarrow 48$	20	0.5	0.3	2	1	0.8
Figure 20. Excitation frequency (σ) and no. of grooves (N_g). Λ = 160.9	$0 \rightarrow 10{,}000$	$6 \rightarrow 48$	20	0.5	0.3	2	1	0.8
Figure 21. Excitation frequency (σ) and no. of grooves (N_g). Λ = 321.8	$0 \rightarrow 10{,}000$	$6 \rightarrow 48$	20	0.5	0.3	2	1	0.8
Figure 22. Pressure variation over a groove-ridge pair. Λ = 160.9, 321.8.	-	12	20	0.5	0.3	2	1	0.8
Figure 23. Pressure surface plot. Λ = 160.9	-	12	20	0.5	0.3	2	1	0.8
Figure 24. Pressure surface plot. Λ = 321.8	-	12	20	0.5	0.3	2	1	0.8
Figure 25, 26. Number of grooves (N_g)		$6 \rightarrow 48$	20	0.5	0.3	2	19.8	0.8
Figure 27, 28. Groove angle (β [°])	≈ 0	12	$10 \rightarrow 80$	0.5	0.3	2	19.8	0.8
Figure 29, 30. Groove width ratio (α_g)	≈ 0	12	20	$0.2 \rightarrow 0.8$	0.3	2	19.8	0.8
Figure 31, 32. Seal dam extent (l)	≈ 0	12	20	0.5	$0 \rightarrow 0.64$	2	19.8	0.8
Figure 33, 34. Groove depth ratio (δ)	≈ 0	12	20	0.5	0.3	$2 \rightarrow 3$	19.8	0.8
Figure 35, 36. Pressure ratio (P_{rat})	≈ 0	12	20	0.5	0.3	2	$1 \rightarrow 30$	0.8
Figure 37,38. Radius Ratio (R)	≈ 0	12	20	0.5	0.3	2	19.8	$0.4 \rightarrow 0.8$
Fixed parameters: *Optima:* Rotating grooves Λ = 160.8; Fig. 19, 22: Λ = 160.9, 321.8 *Fluid properties:* $\mu = 1.9 \times 10^{-5}$ Pa·s $\Re_g$ = 8314.34 J/kmole·K T = 323.15 K	-	12	12°	0.5	0.16	1.8	-	-

Effect of the Number of Grooves (N_g) with No Pressure Drop. Effects from the spiral grooves alone, demonstrated by a *SGFS* without a pressure drop, demonstrate the necessity of keeping the number of grooves (N_g) small and thus the benefits of having a predictive model capable of characterizing this situation. Figure 19 indicates that the opening force $\left(\overline{W}\right)$ increases only slightly with the number of grooves (N_g) for two speed numbers (Λ = 160.9, 321.8). The static axial stiffness coefficient $\left(\overline{K}_{zz}\right)$ shows a slight increase with the number of grooves (N_g) at the lower speed number (Λ) while the stiffness $\left(\overline{K}_{zz}\right)$ increases greatly with the number of grooves (N_g) at high speed numbers (Λ), when compressibility becomes important. Without a radial pressure drop, the axial (zero frequency) damping coefficient $\left(\overline{C}_{zz}\right)$ exhibits stabilizing (positive) behavior for only small numbers of grooves (N_g). Higher speeds provide more opening force $\left(\overline{W}\right)$ and stiffness $\left(\overline{K}_{zz}\right)$, but the damping $\left(\overline{C}_{zz}\right)$ at these speeds becomes more negative, further into the unstable region. In the case with a pressure ratio (P_{rat}) of unity, static or zero-frequency force coefficients represent the asymptotic limit of the force coefficient at low excitation frequencies, as will be discussed immediately.

Effect of the Excitation Frequency (σ) and Number of Grooves (N_g) with No Pressure Drop. The frequency dependence of the force coefficients becomes apparent at high excitation frequencies (σ), and the number of grooves (N_g) has a pronounced effect, as given in Figures 20 and 21 for lower and higher speed numbers (Λ = 160.9, 321.8),

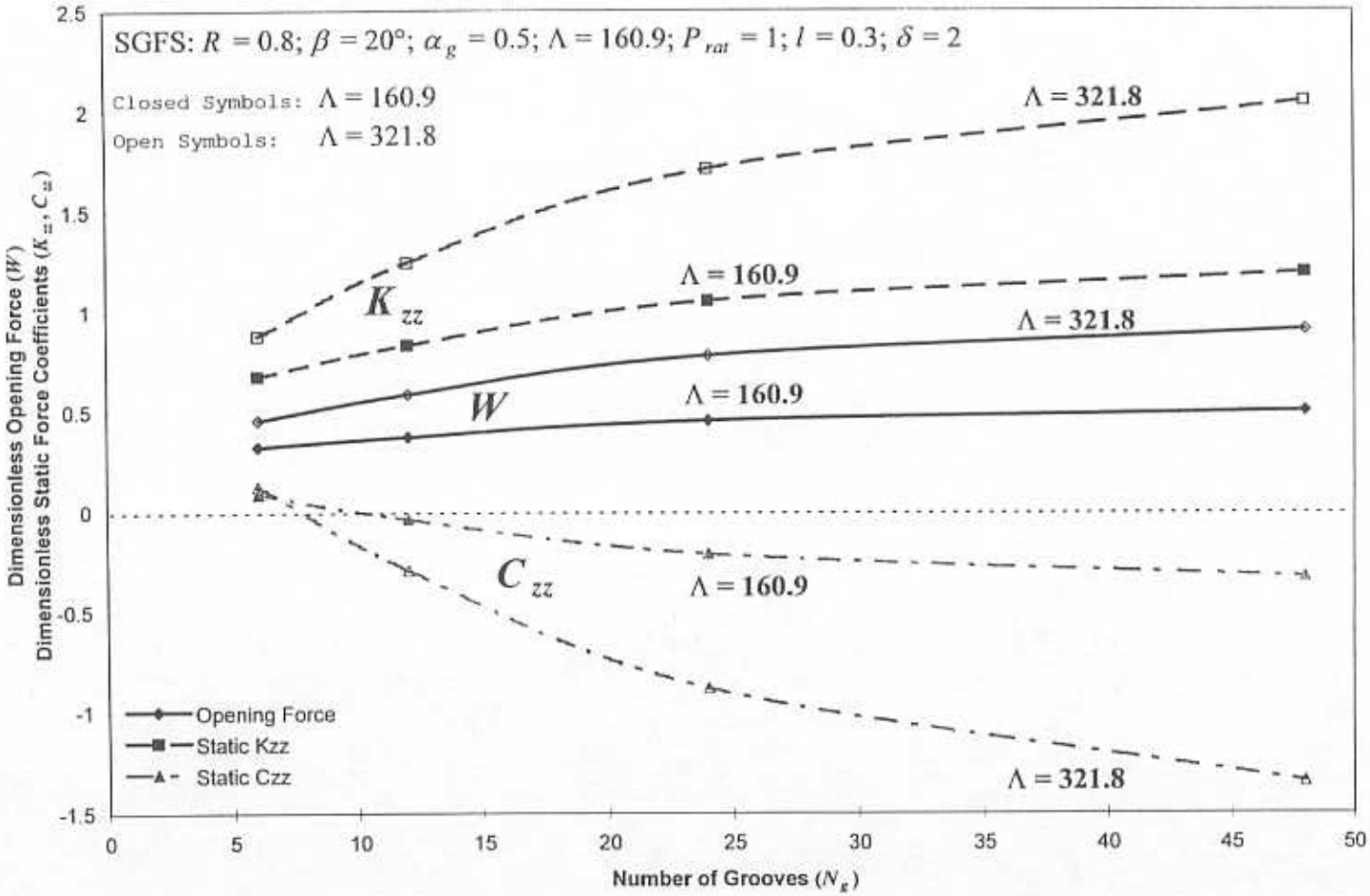

Fig. 19 Variation of the opening force and static force coefficients with the number of grooves (N_g) for two speed numbers (Λ).

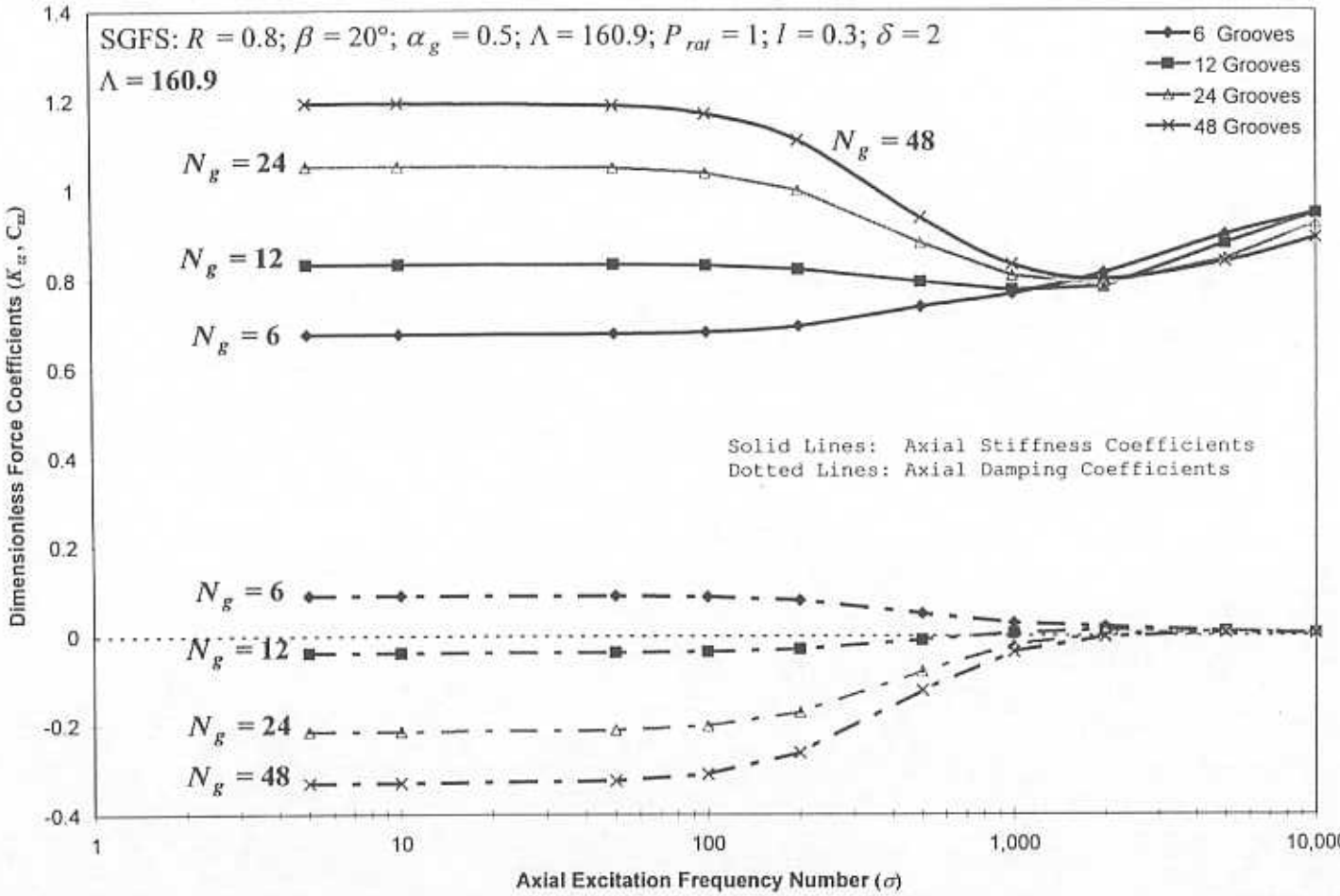

Fig. 20 Variation of the force coefficients with excitation frequency for increasing numbers of grooves (N_g). $\Lambda = 160.9$.

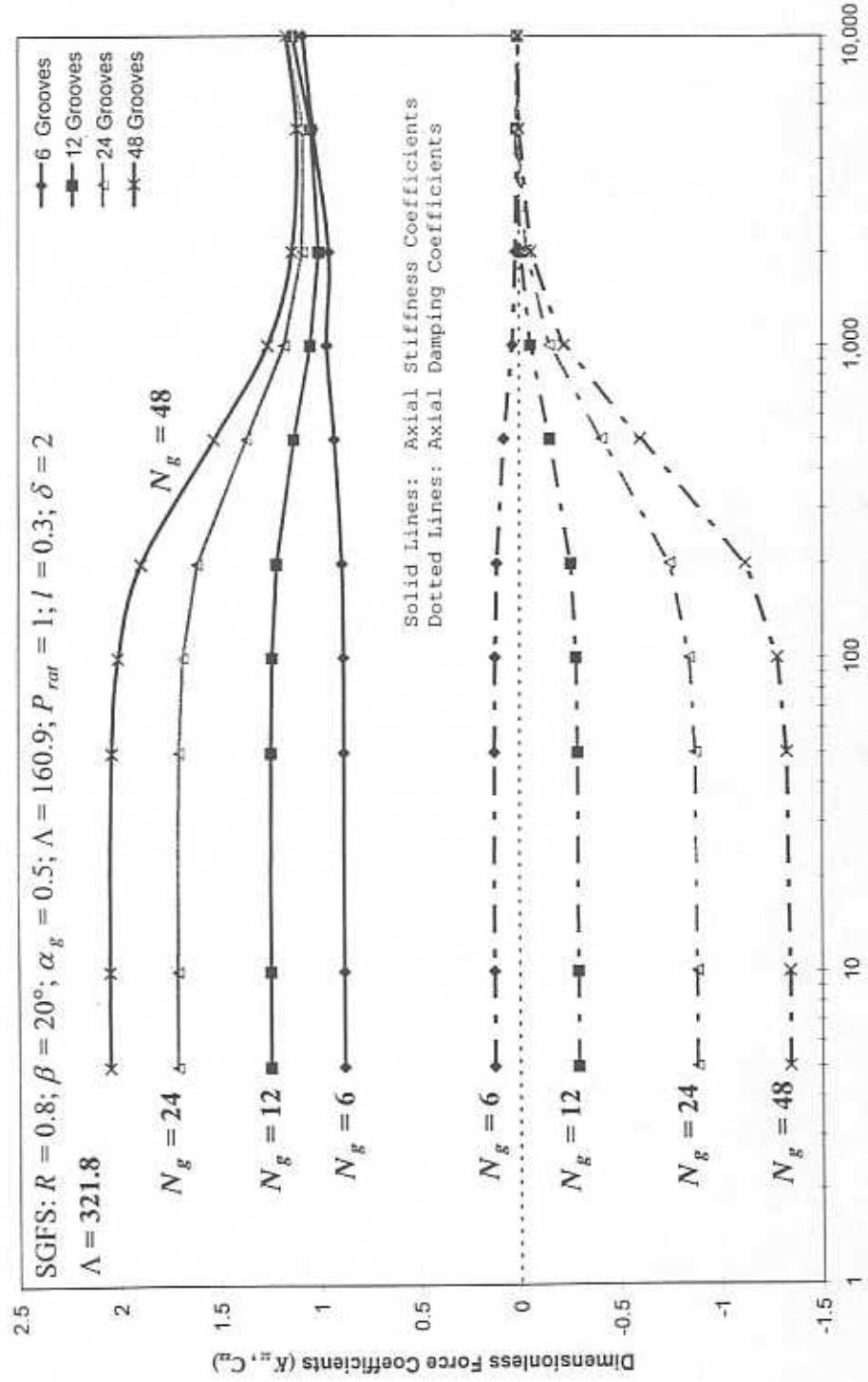

Fig. 21 Variation of the force coefficients with excitation frequency for increasing numbers of grooves (N_g). $\Lambda = 321.8$.

respectively. Axial stiffness $\left(\overline{K}_{zz}\right)$ and damping $\left(\overline{C}_{zz}\right)$ remain constant as excitation frequency (σ) increases for both low excitation frequencies and a small number of grooves (N_g). At low excitation frequencies (σ), the stiffness $\left(\overline{K}_{zz}\right)$ increases with the number of grooves (N_g), but the stiffness coefficients $\left(\overline{K}_{zz}\right)$ all tend toward the same values at high excitation frequencies (σ) for any number of grooves . While only small numbers of grooves (N_g) give consistently positive damping coefficients $\left(\overline{C}_{zz}\right)$, the damping tends toward zero independent of the number of grooves (N_g) showing marginal stability at high excitation frequencies (σ). Without a pressure drop across the seal, the present model predicts instability with large numbers of grooves (N_g) since negative axial damping coefficients $\left(\overline{C}_{zz}\right)$ occur.

Pressure Variation between Grooves and Ridges. As stated earlier, one of the primary advantages of the present *FEM* analysis over the traditional *NGT* is the ability to obtain the pressure variation over a groove-ridge pair. Figure 22 illustrates this by showing the circumferential pressure variation for one groove-ridge pair at the interface between the seal dam and grooved portion for two different speed numbers (Λ = 160.9, 321.8) without a pressure drop (P_{rat} = 1). Obviously, the higher speed yields higher pressures in general. The fact that the pressure at the entrance of the groove equals the pressure at the exit of the ridge implies fulfillment of the circumferential periodicity condition between grooves and ridges. The entire pressure field for the lower speed

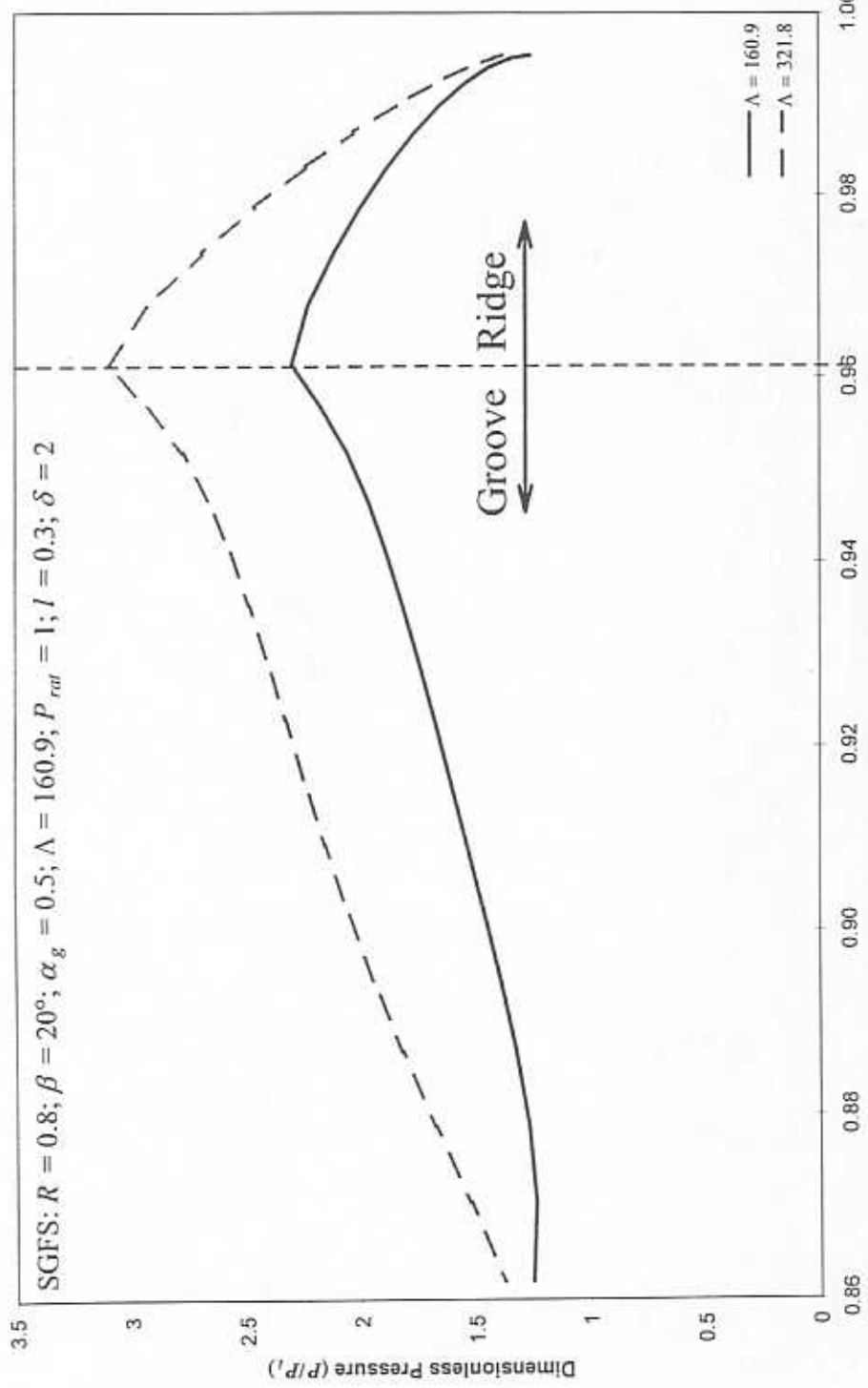

Fig. 22 Pressure variation over a groove-ridge pair at the end of the seal dam. $\Lambda = 160.9, 321.8$.

number ($\Lambda = 160.9$), displayed in Figure 23, shows a peak in pressure near the end of the grooves (or beginning of the seal dam). Figure 24 shows the similar response of pressure with high speeds ($\Lambda = 321.8$). Pressures are elevated over those of the previous speed with more pressure drop required in the ridge region.

Effect of the Number of Grooves (N_g). The parametric study continues with demonstration of the effect of the different parameters on a *SGFS* with a large pressure ratio ($P_{rat} = 19.8$). Note that in general, the leakage flow rate $\left(\overline{Q}\right)$ is a fraction of the flow rate for geometrically identical flat plates separated by the ridge clearance (c) operating with compressible fluids. (See Appendix A.) The opening force $\left(\overline{W}\right)$, power loss $\left(\overline{\wp}\right)$, and leakage rate $\left(\overline{Q}\right)$ remain unchanged with an increase in the number of grooves (N_g), as shown in Figure 25.

With high pressure ratios (P_{rat}), the force coefficients change little with excitation frequency (σ), thus static force coefficients are representative throughout the range of excitation frequencies ($\sigma \leq 5\Lambda$). Figure 26 shows that the dimensionless static ($\sigma \cong 0$) axial stiffness coefficient $\left(\overline{K}_{zz}\right)$ rises prominently from the smallest values of N_g but becomes asymptotic as the number of grooves becomes large. The dimensionless static axial damping coefficient $\left(\overline{C}_{zz}\right)$ reaches a minimum value at $N_g = 14$ before rising slightly for a larger number of grooves (N_g). Considering the previous concerns about stability, the point at which the stiffness and damping cross ($N_g = 12$) determines the

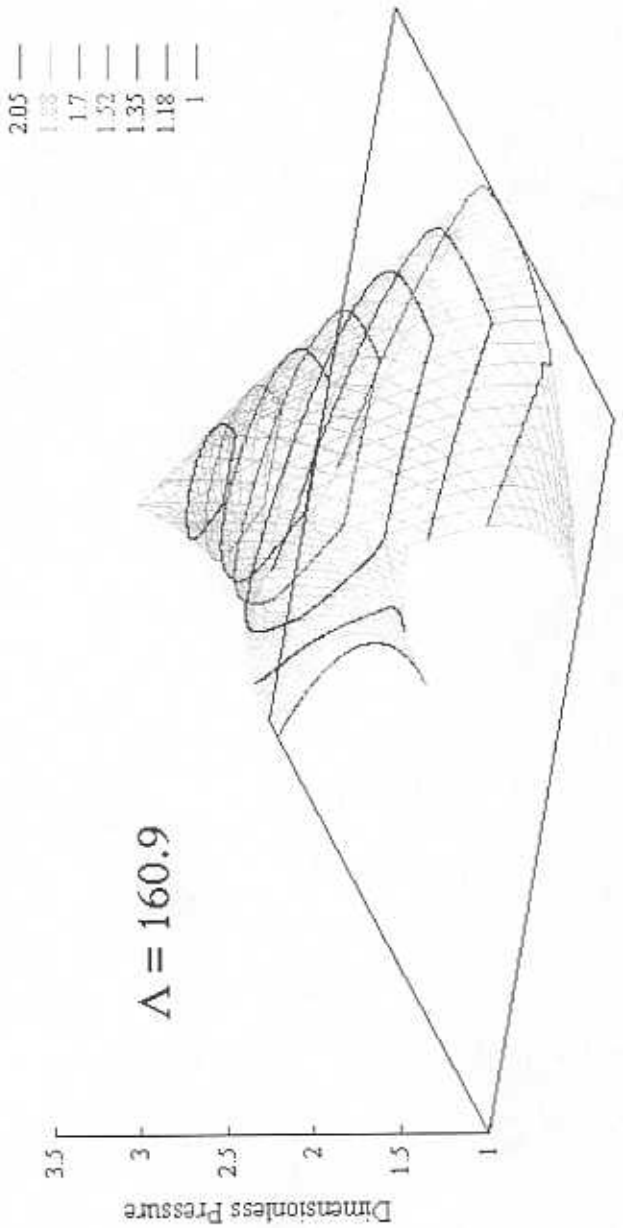

Fig. 23 Pressure surface plot with isobaric lines. $\Lambda = 160.9$.

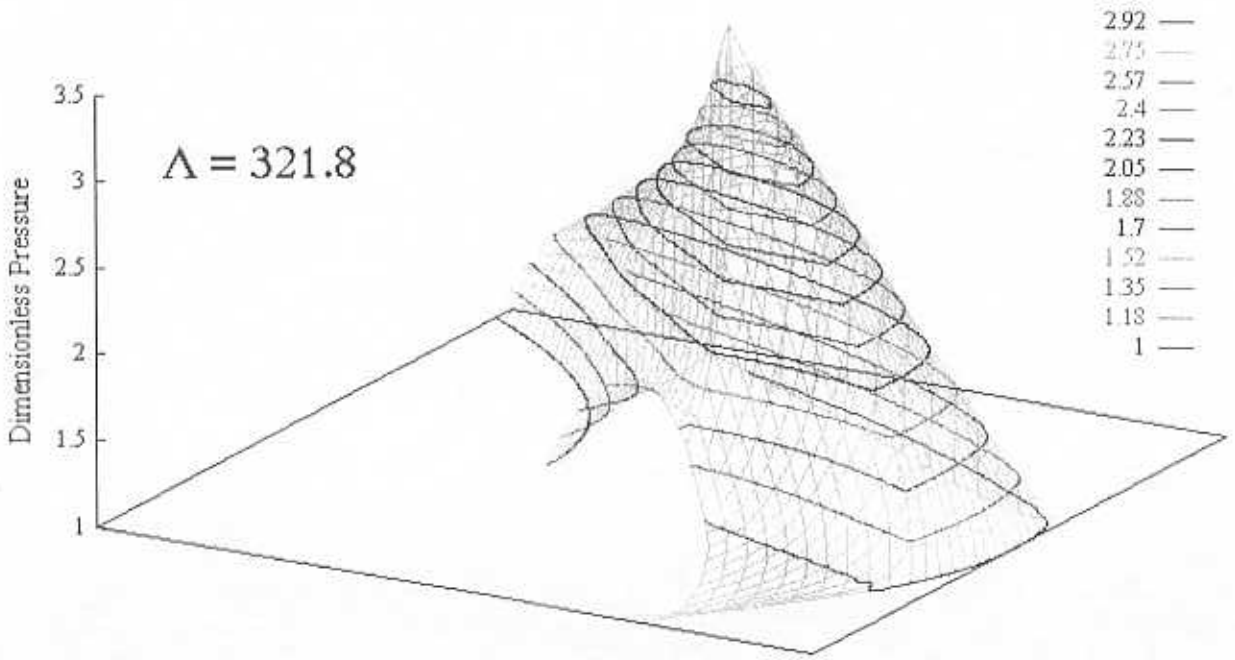

Fig. 24 Pressure surface plot with isobaric lines. $\Lambda = 321.8$.

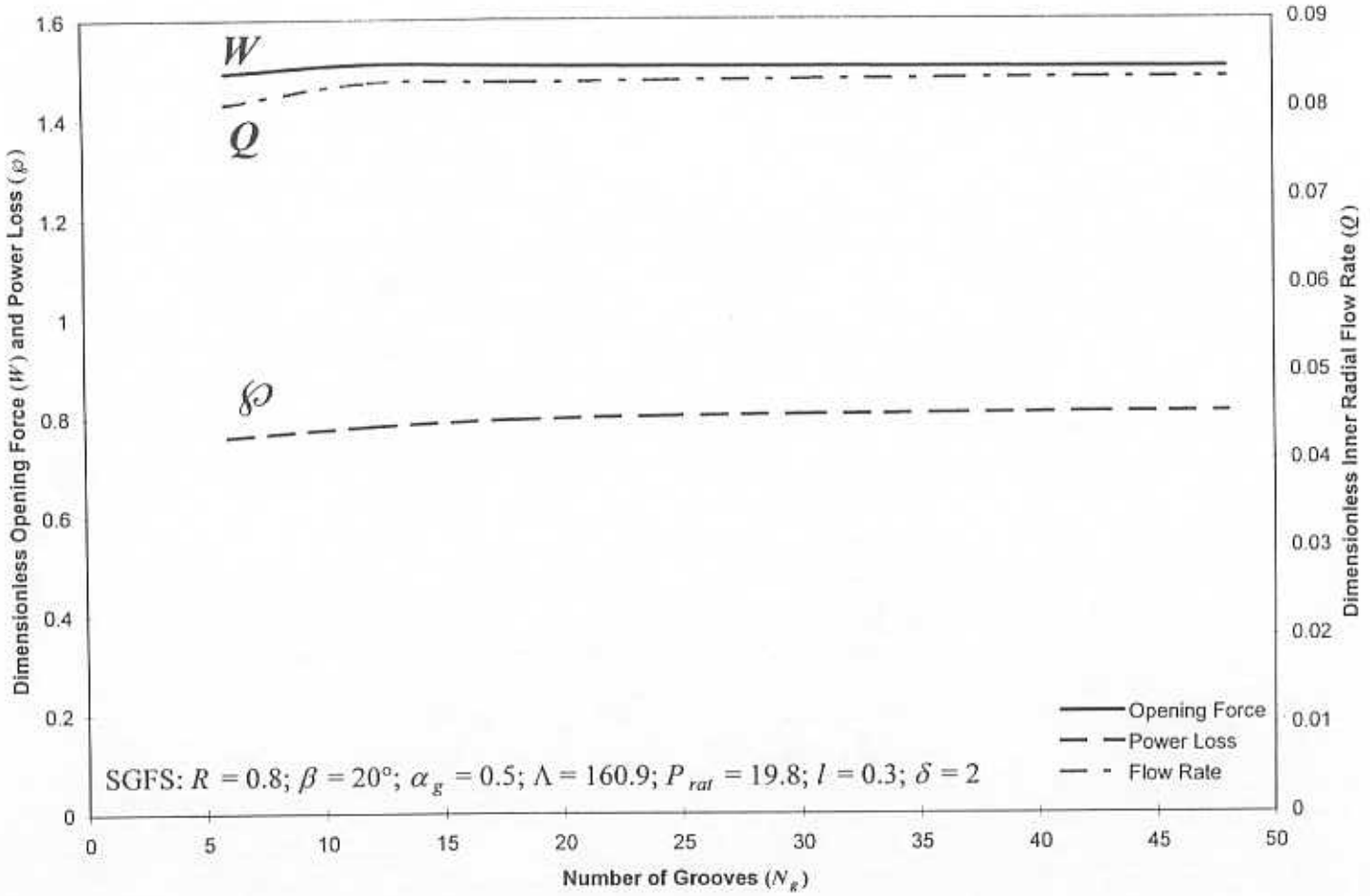

Fig. 25 Variation of opening force, power loss, and leakage rate with the number of grooves (N_g).

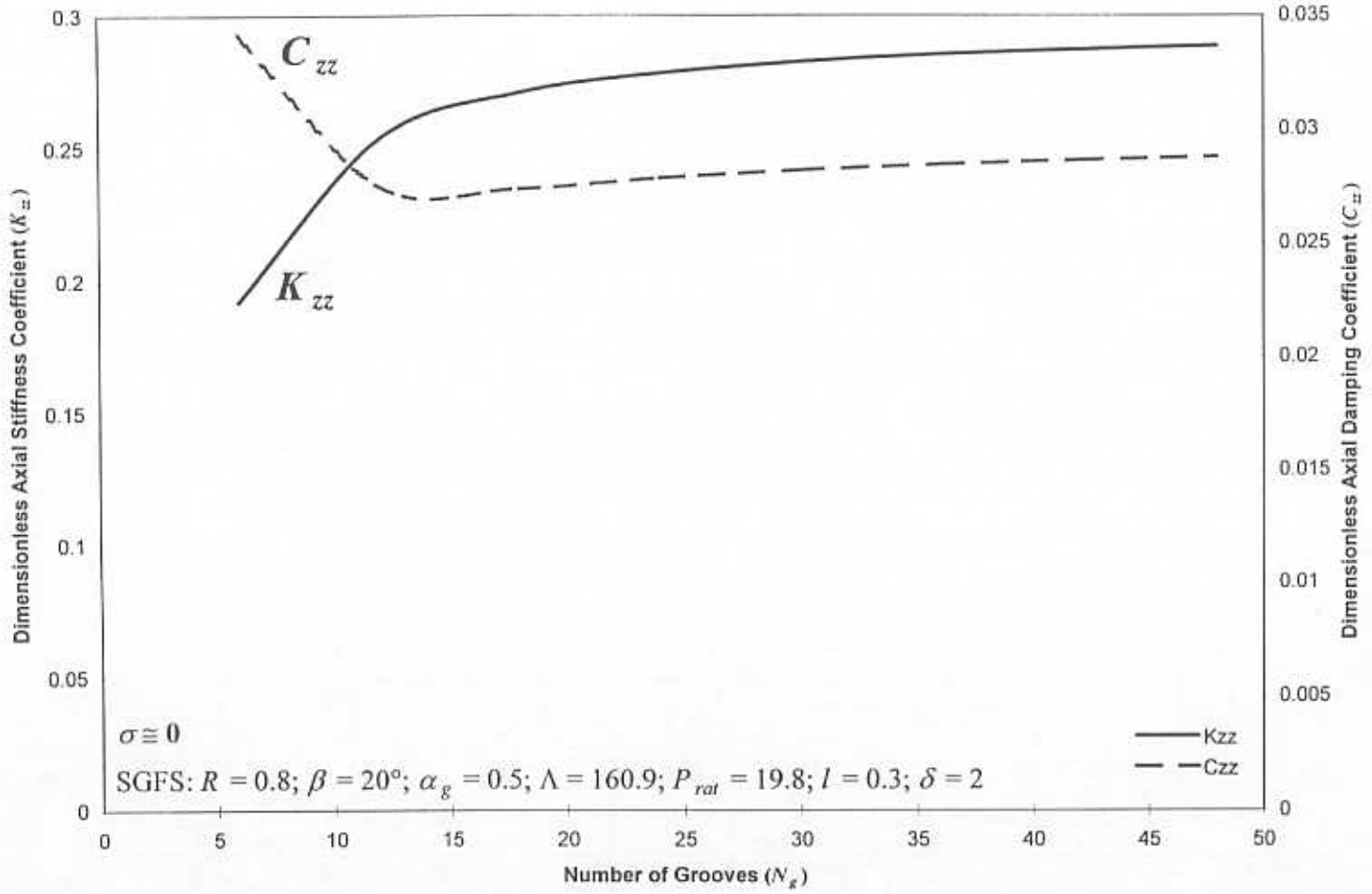

Fig. 26 Variation of the force coefficients with the number of grooves (N_g).

optimum number of grooves since this crossing represents a good operating point of relatively high stiffness and damping.

Effect of the Spiral Groove Angle (β). Although opening force $\left(\overline{W}\right)$ and power loss $\left(\overline{\wp}\right)$ are constant with increasing groove angles (β), leakage rate $\left(\overline{Q}\right)$ peaks by a groove angle of 35°, illustrated in Figure 27. Figure 28 shows that maximum static axial stiffness $\left(\overline{K}_{zz}\right)$ occurs at a groove angle (β) of 18° while the static axial damping coefficient $\left(\overline{C}_{zz}\right)$ reaches a minimum at a groove angle (β) of 21°. The force coefficient lines cross when the groove angle (β) approaches 12°. The choice of optimum groove angle obviously depends on many factors, the importance of which depends on the particular application. In this case, the optimum groove angle (β) of 12° ensures low leakage with good dynamic force characteristics.

Effect of the Groove Width Ratio (α_g). Figure 29 shows the opening force $\left(\overline{W}\right)$ and leakage rate $\left(\overline{Q}\right)$ to increase with groove width ratio (α_g) while the power loss $\left(\overline{\wp}\right)$ decreases. In Figure 30, the static axial damping coefficient $\left(\overline{C}_{zz}\right)$ also decreases as the groove width ratio (α_g) increases, but the static axial stiffness coefficient $\left(\overline{K}_{zz}\right)$ reaches a maximum value when the groove width equals the ridge width ($\alpha_g = 0.5$) determining the optimum value of groove width ratio. Having a large number of grooves (N_g),

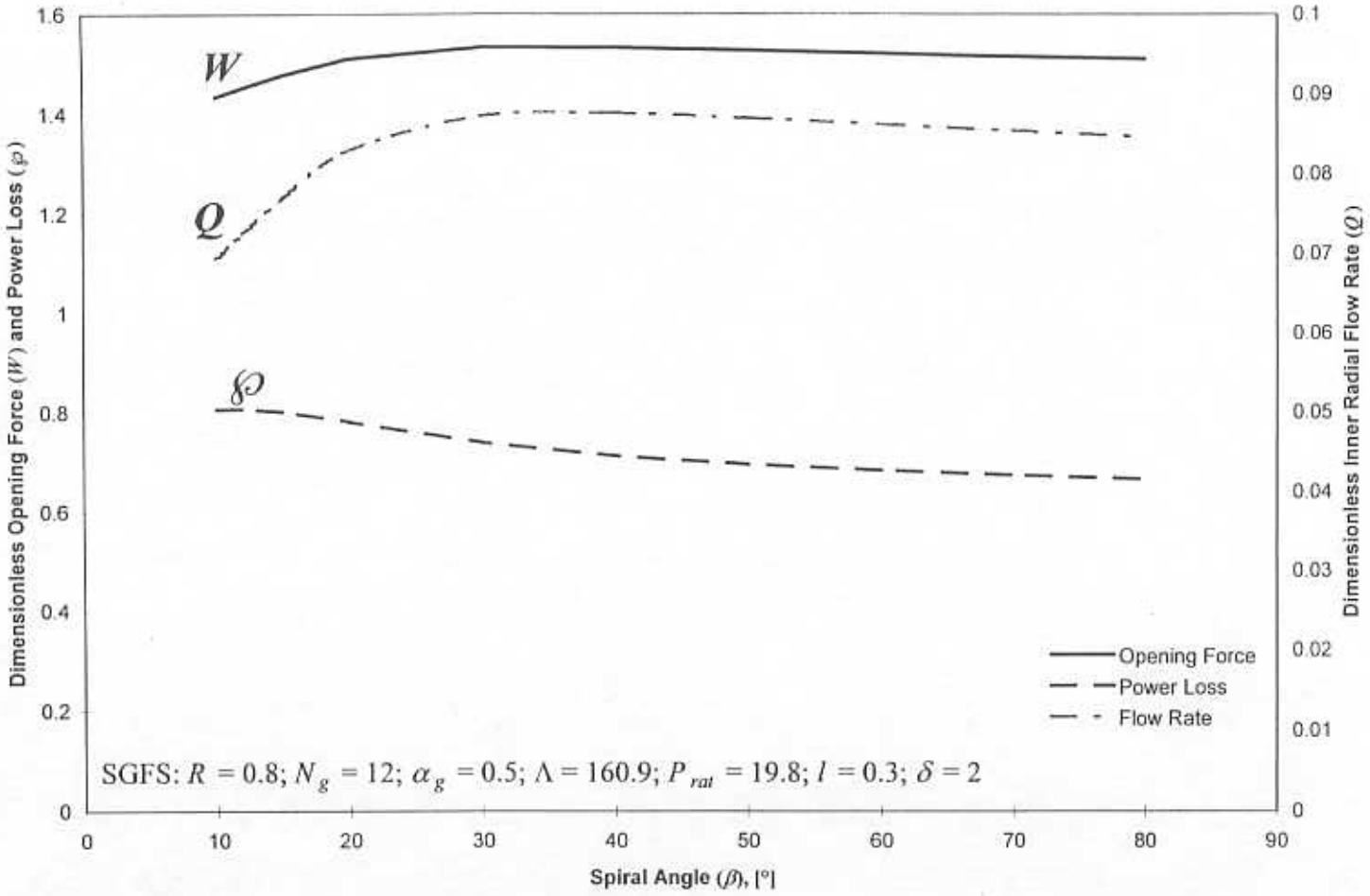

Fig. 27 Variation of opening force, power loss, and leakage rate with the spiral groove angle (β).

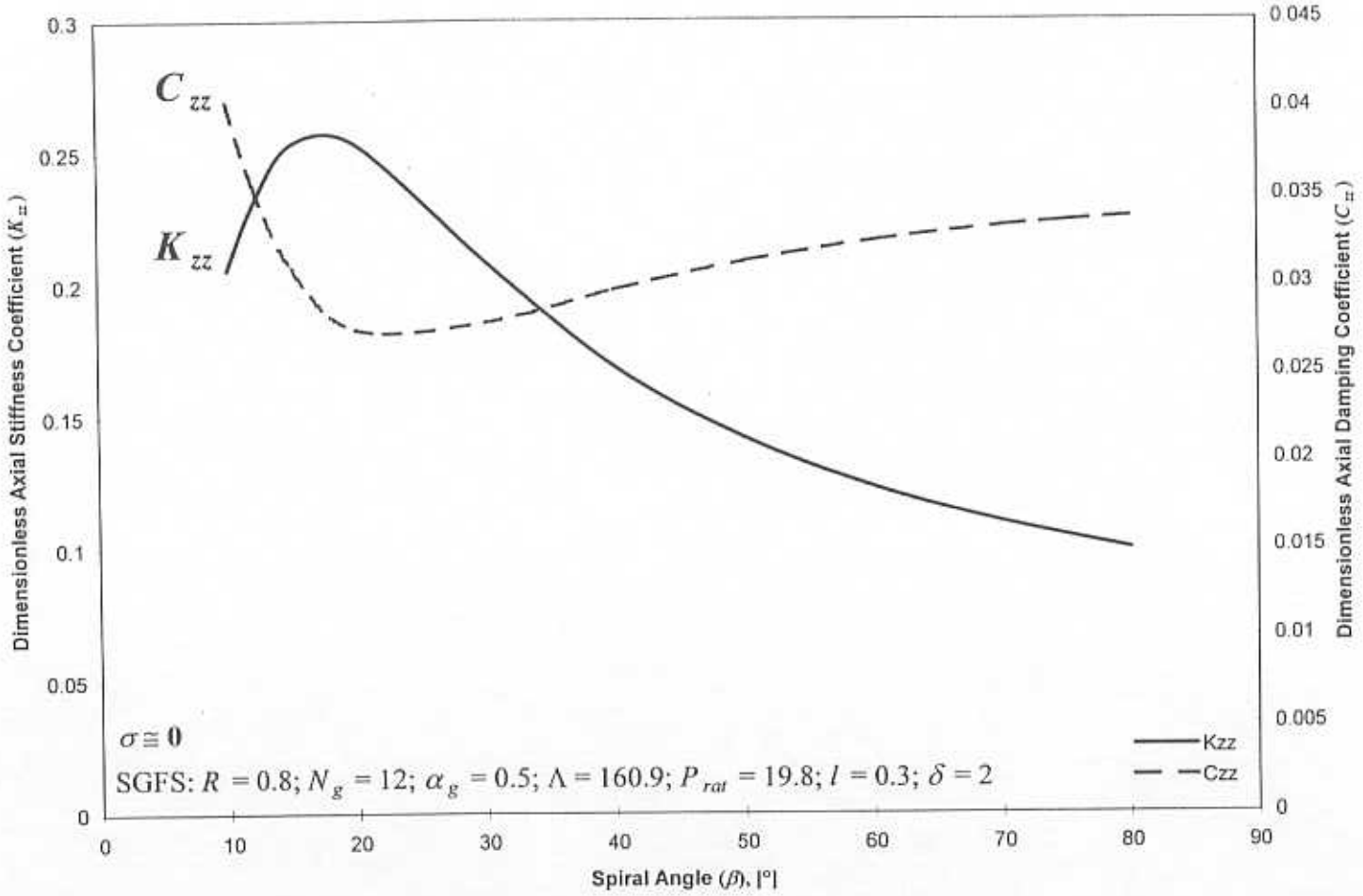

Fig. 28 Variation of the force coefficients with the spiral groove angle (β).

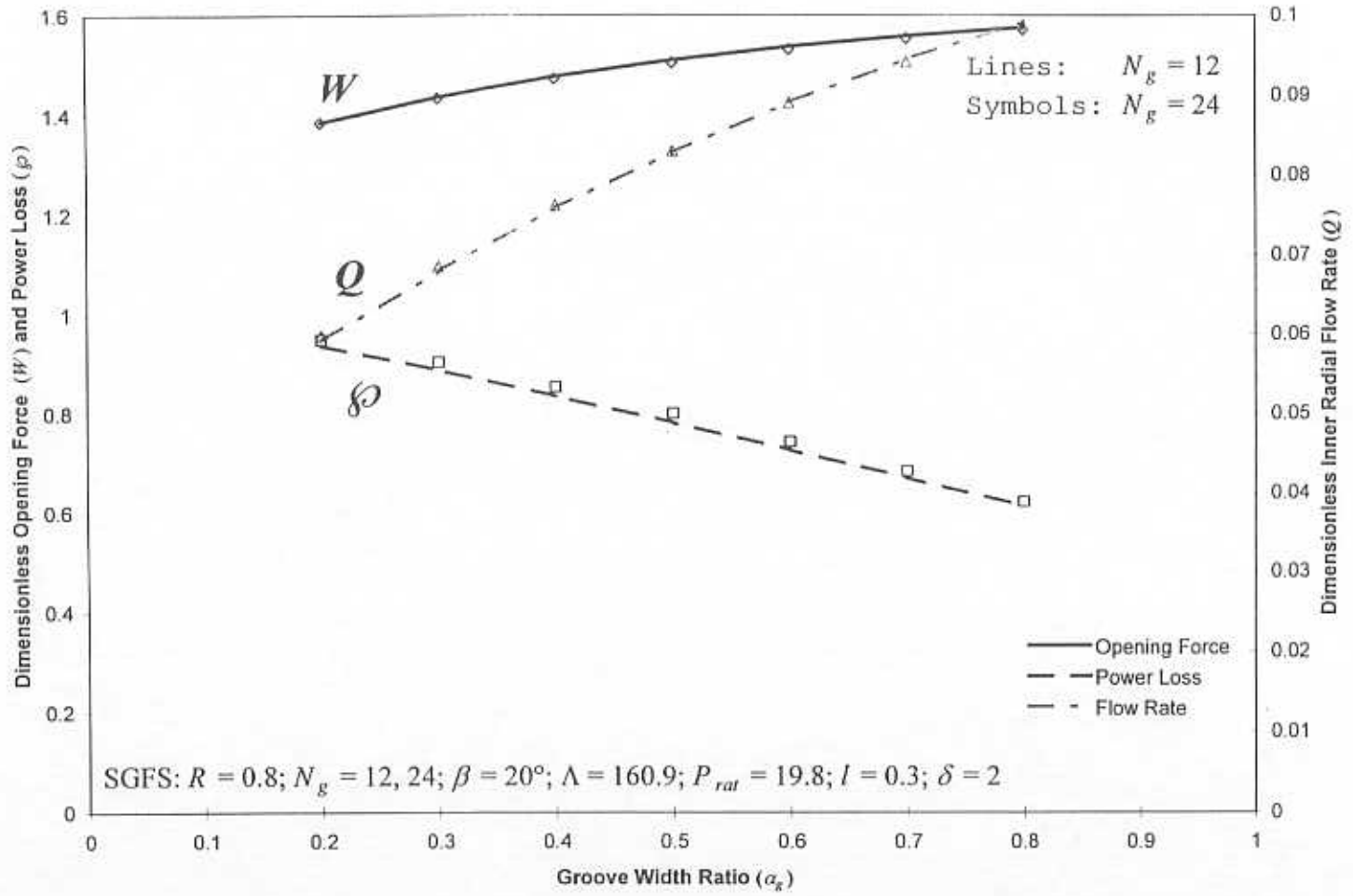

Fig. 29 Variation of opening force, power loss, and leakage rate with the groove width ratio (α_g).

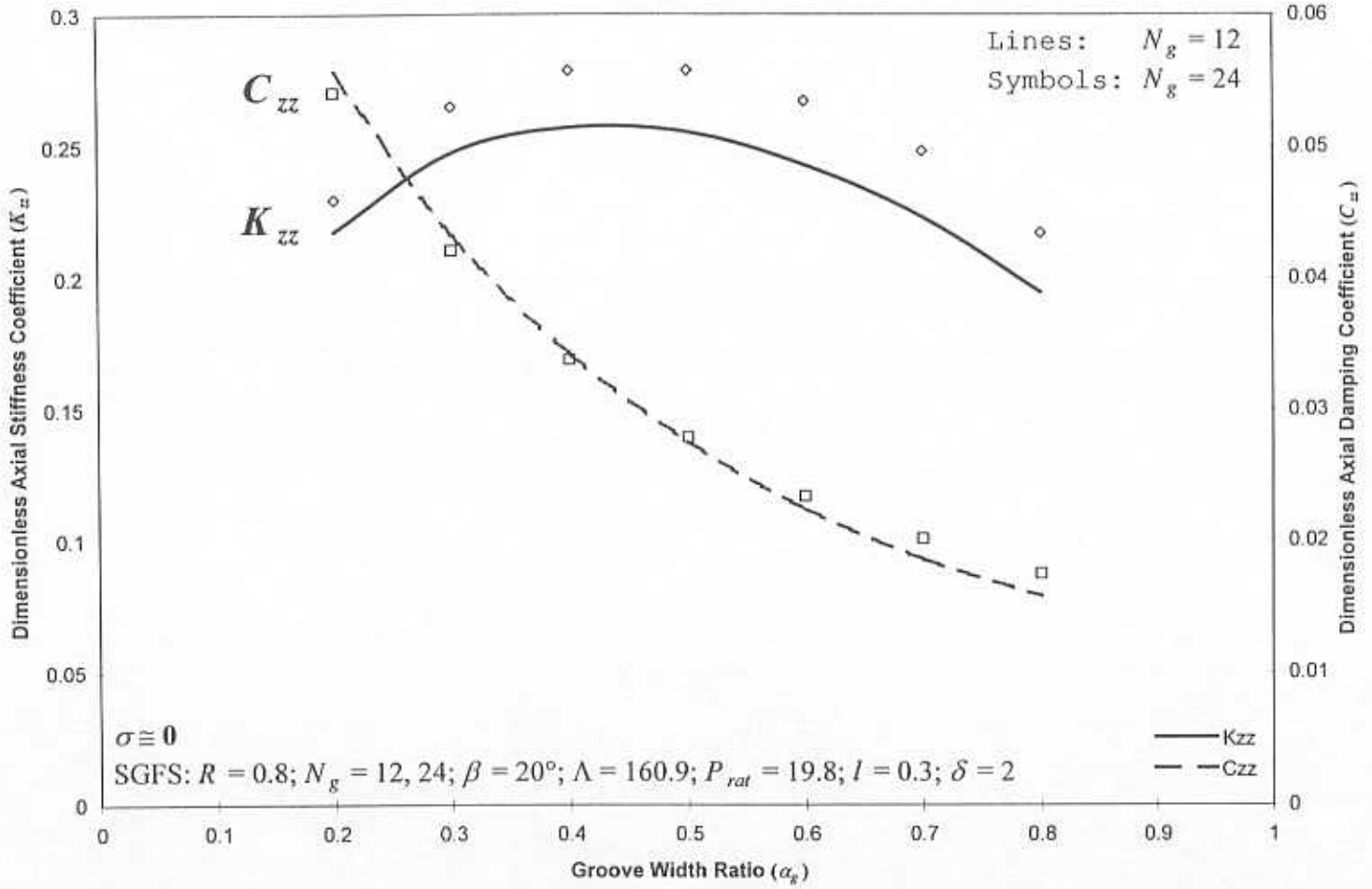

Fig. 30 Variation of the force coefficients with the groove width ratio (α_g).

indicated by symbols on each graph, contributes negligibly to the axial damping $\left(\overline{C}_{zz}\right)$ and face seal static characteristics (opening force, power loss, and leakage rate) while giving slightly larger stiffness $\left(\overline{K}_{zz}\right)$.

Effect of the Seal Dam Extent (l). Figure 31 shows that the opening force $\left(\overline{W}\right)$ reaches a maximum value while the power loss $\left(\overline{\wp}\right)$ is a minimum when the seal dam extends over 30% of the radial face width. The leakage rate $\left(\overline{Q}\right)$ decreases as the seal dam extent (l) increases since the average clearance of the face seal also decreases as the seal dam covers more of the face area. Figure 32 shows the dramatic effect of the seals dam extent (l) on the axial stiffness coefficient $\left(\overline{K}_{zz}\right)$ with a marked peak at a seal dam extent of 16%. The damping coefficient $\left(\overline{C}_{zz}\right)$ increases with the seal dam extent (l). Since designers usually incorporate seal dams to increase seal stiffness, the seal dam radial extent (l) of 0.16 becomes the optimum value.

Effect of the Groove Depth Ratio (δ). Figure 33 indicates a rise in leakage rate $\left(\overline{Q}\right)$ as the groove depth ratio increases (δ) since an increase in this parameter also indicates an increase in the average clearance. Opening force $\left(\overline{W}\right)$ increases slightly with groove depth ratio (δ) while the power loss $\left(\overline{\wp}\right)$ and damping coefficient $\left(\overline{C}_{zz}\right)$ (in Figure 34) decrease. In this case, the stiffness coefficient $\left(\overline{K}_{zz}\right)$ determines the optimum groove

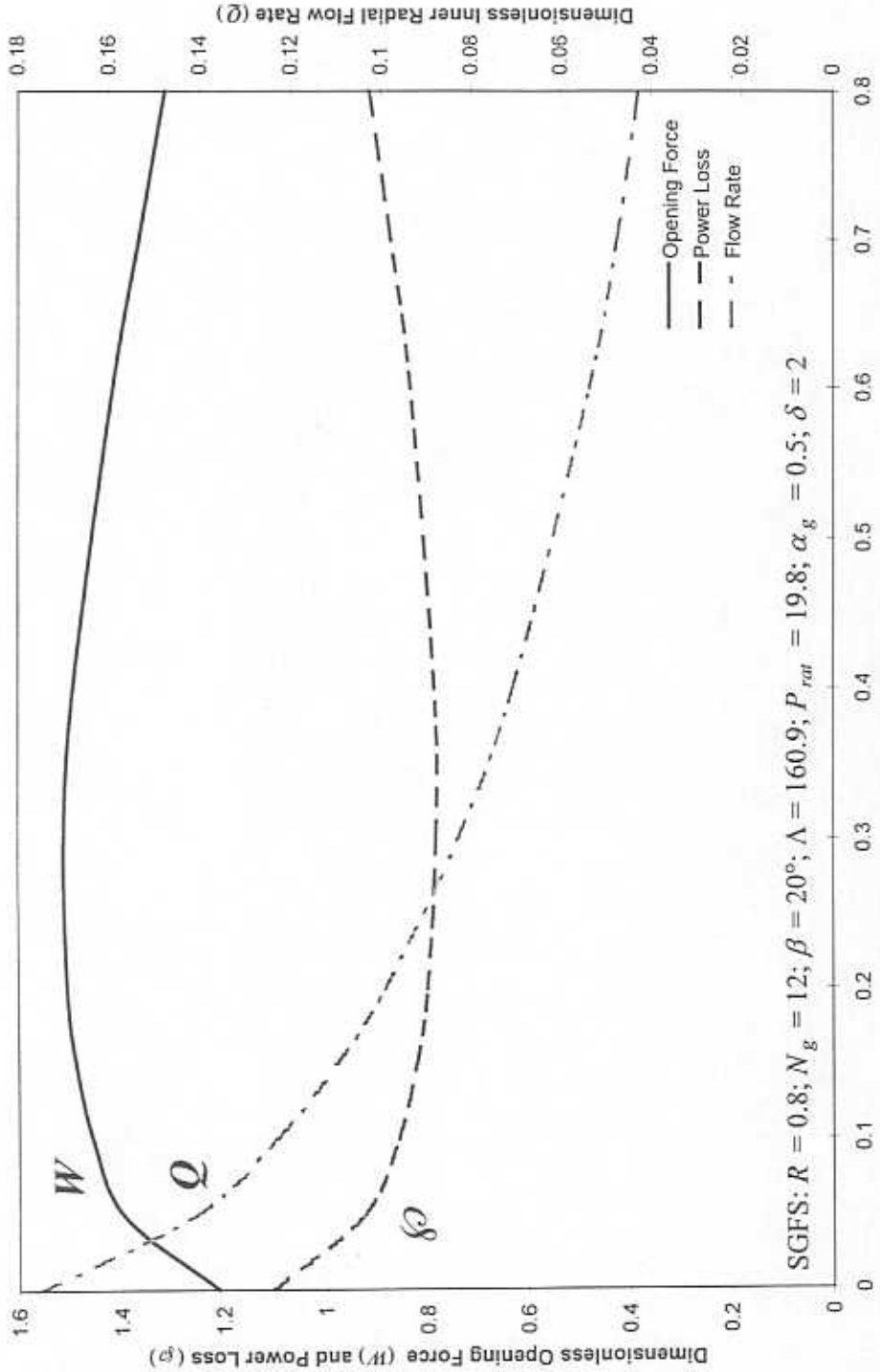

Fig. 31 Variation of opening force, power loss, and leakage rate with the radial seal dam extent (l).

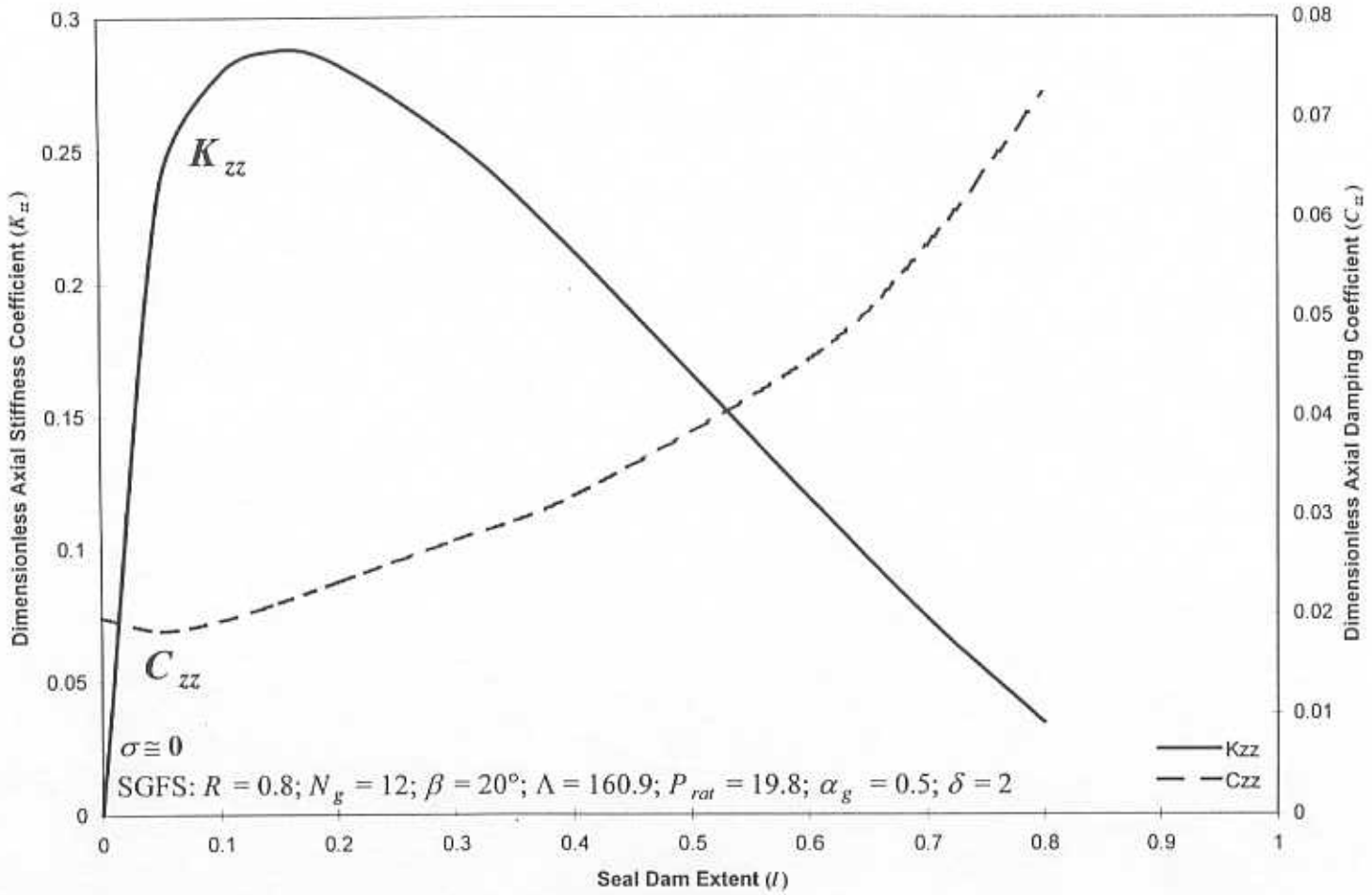

Fig. 32 Variation of the force coefficients with the radial seal dam extent (l).

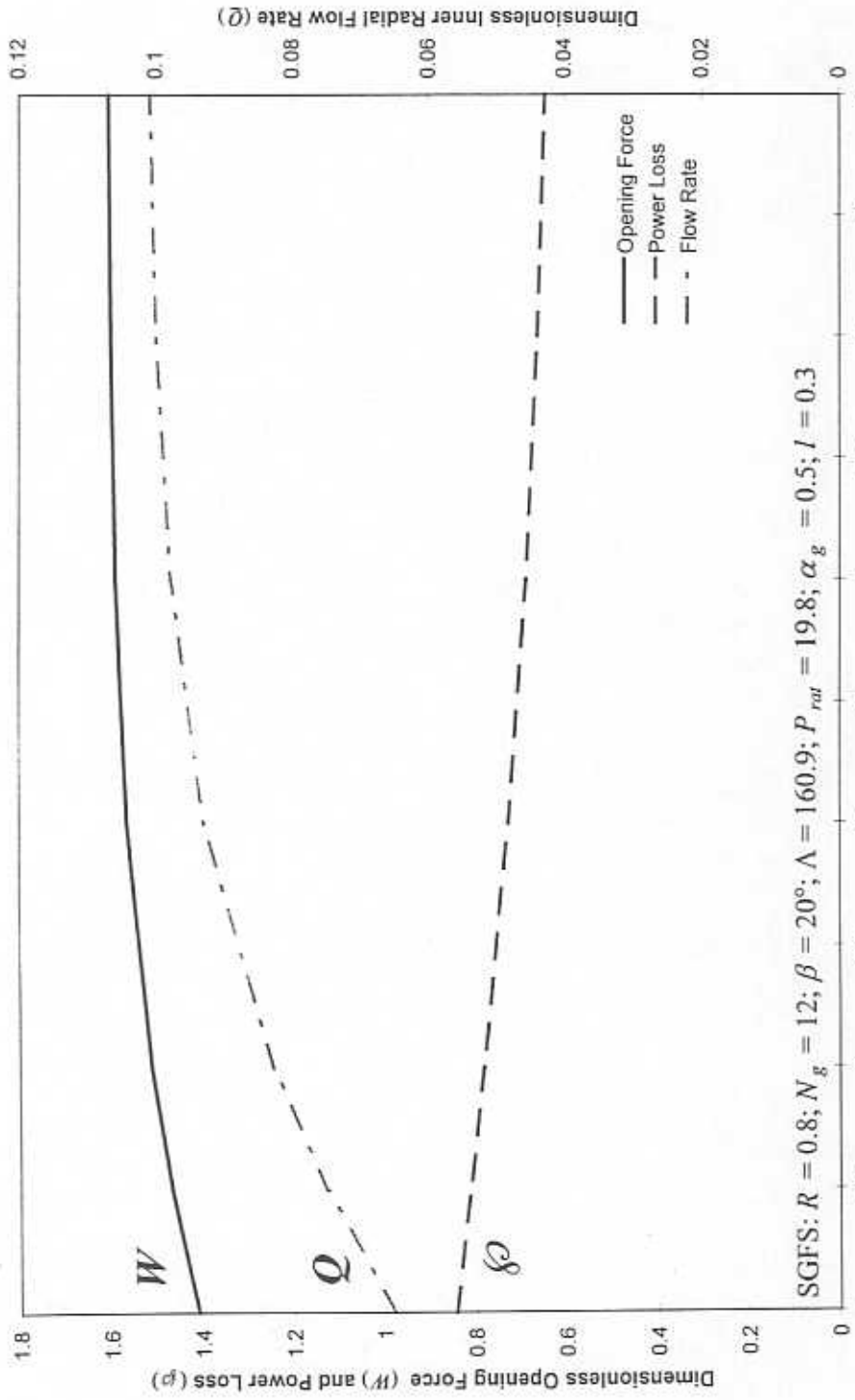

Fig. 33 Variation of opening force, power loss, and leakage rate with the groove depth ratio (δ).

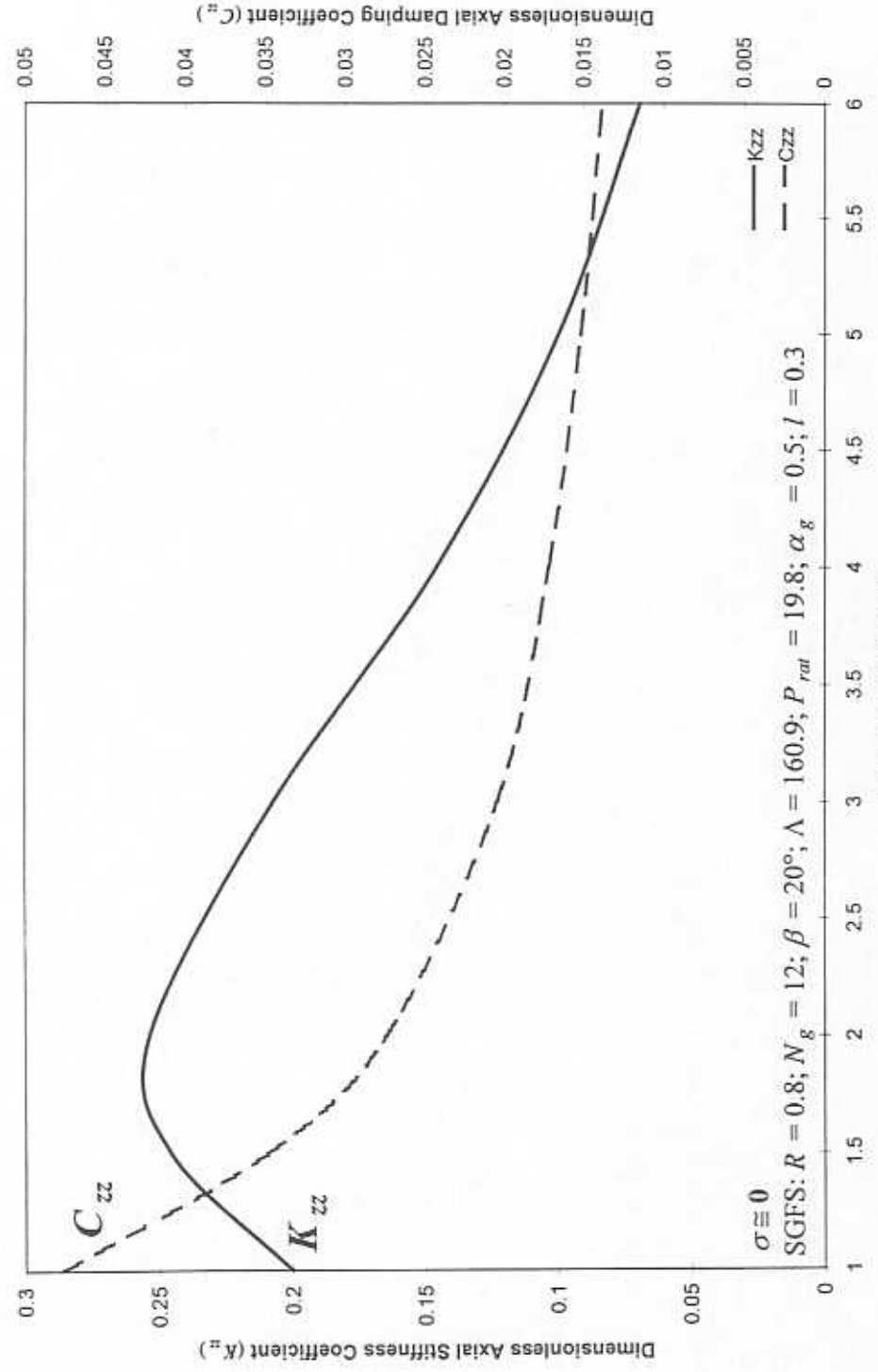

Fig. 34 Variation of the force coefficients with the groove depth ratio (δ).

depth ratio since it reaches a maximum value at a groove depth ratio (δ) of 1.8 as depicted in Figure 34.

Effect of the Pressure Ratio (P_{rat}). The expected result from raising the pressure ratio between the inner and outer seal diameters, as given in Figure 35, is an increase in the opening force $\left(\overline{W}\right)$ and leakage flow rate $\left(\overline{Q}\right)$. Power loss $\left(\overline{\wp}\right)$ remains almost unaffected by changes in the pressure ratio across the seal. Figure 36 shows the force coefficient behavior with an increase in the pressure ratio (P_{rat}). Since the force coefficients are made dimensionless with the average pressure, trends of the original dimensional parameters are not preserved. However, the figures are provided as a design tool. Both axial stiffness $\left(\overline{K}_{zz}\right)$ and damping coefficient $\left(\overline{C}_{zz}\right)$ actually rise steadily as the pressure ratio (P_{rat}) increases. Note that at low pressure ratios (P_{rat}), the damping $\left(\overline{C}_{zz}\right)$ tends to zero, as discussed earlier.

Effect of the Radius Ratio (R). Figure 37 shows that as the ratio between the inner and outer radii (R) increases, the opening force $\left(\overline{W}\right)$ drops since the face area over which pressure can develop is greatly reduced. Since the characteristic values for leakage rate $\left(\overline{Q}\right)$ and power loss $\left(\overline{\wp}\right)$ use the inner radius, trends of the dimensional parameters are not preserved. In actuality, the leakage rate increases while the power loss decreases with an increase in the radius ratio (R). Both the stiffness $\left(\overline{K}_{zz}\right)$ and damping

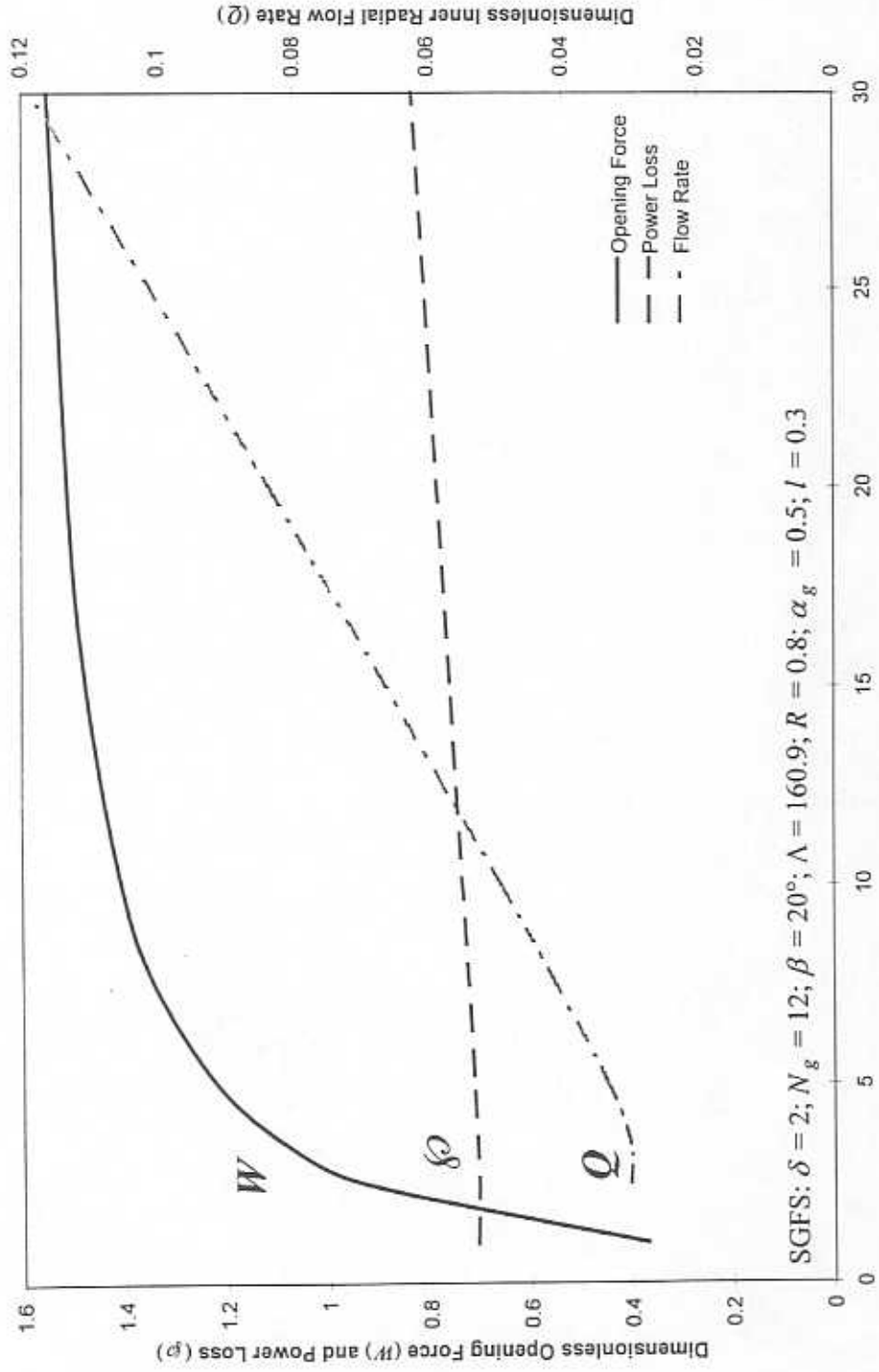

Fig. 35 Variation of opening force, power loss, and leakage rate with the pressure ratio (P_{rat}).

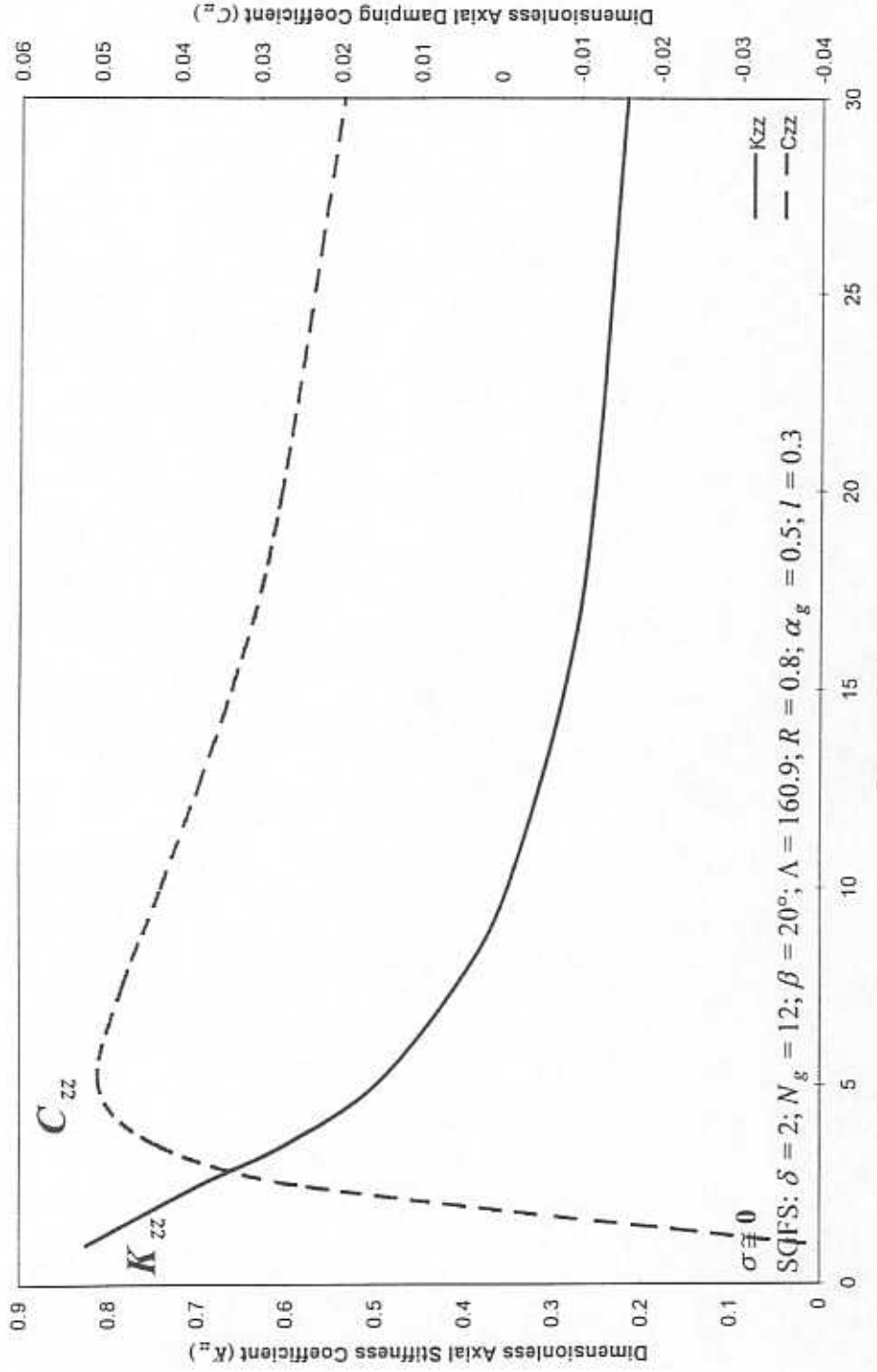

Fig. 36 Variation of the force coefficients with the pressure ratio (P_{rat}).

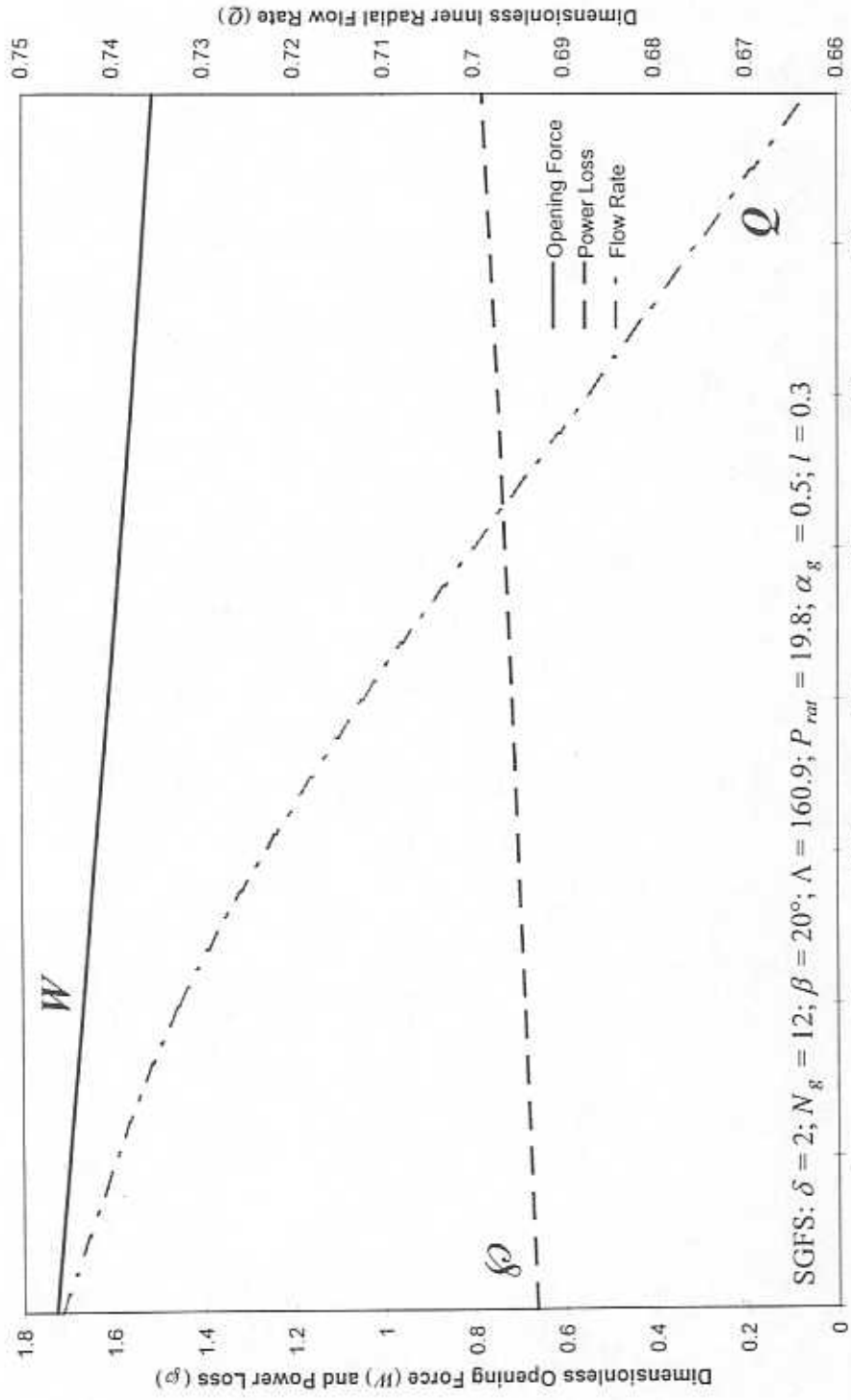

Fig. 37 Variation of opening force, power loss, and leakage rate with the radius ratio (R).

coefficients $\left(\overline{C}_{zz}\right)$, given in Figure 38, generally drop as the radius ratio (R) increases. No optimum is provided since this parameter depends on the specific application and installation geometry. In general, decreasing the radius ratio (R) may provide more stability with larger force coefficients but at the expense of higher power loss.

Summary. The example used in demonstrating *SGFS* behavior yields an interesting result. With a large pressure ratio (P_{rat}), the virtual independence of the static parameters, such as the opening force, with an increase in the number of grooves (N_g) would imply that having grooves on a face seal is unimportant. This predicted behavior is a result of pressure ratio (P_{rat}) having a much greater influence on the opening force than seal hydrodynamics, which arise entirely from the grooves in the absence of misalignments. However, the *SGFS* performance, both static and dynamic, is highly influenced by changes in groove geometry itself, such as groove width ratio (α_g), seal dam extent (l), groove angle (β), and groove depth ratio (δ). Thus, the advantage of the *SGFS* with a large pressure drop occurs as a result of having grooves of a certain configuration, regardless of how many. However, in the absence of a pressure ratio ($P_{rat} = 1$), stability concerns evidenced by negative damping at low excitation frequencies necessitates the use of only a small number of grooves. Attention to this case ($P_{rat} = 1$) applies both to thrust bearings and to face seals with an unexpected loss in pressure.

The results presented in the parametric study are considered as mesh independent since a refinement in the mesh (doubling each mesh parameter) does not change the

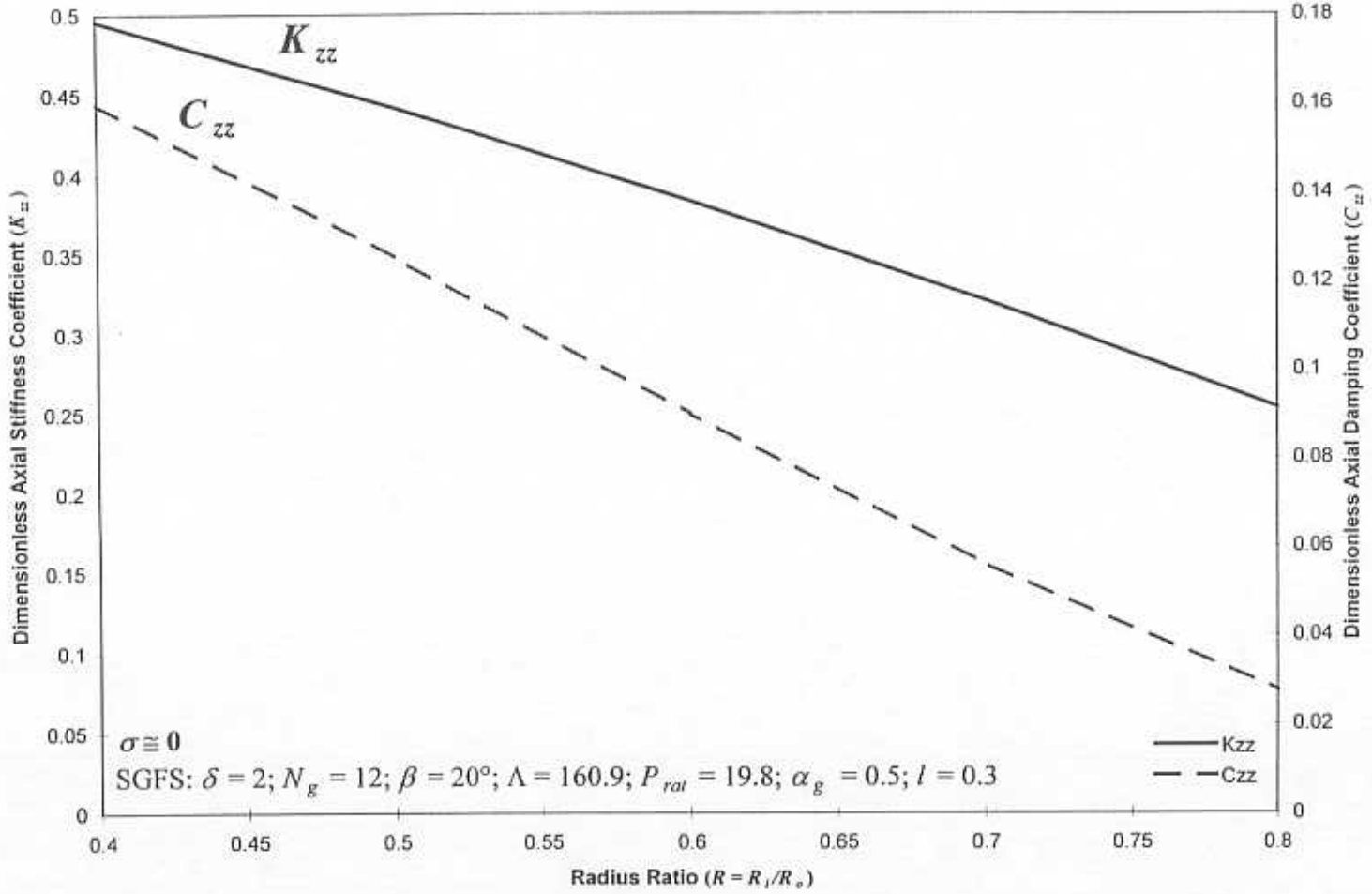

Fig. 38 Variation of the force coefficients with the radius ratio (R).

results significantly (< 2%). Much care was taken to ensure the convergence of the numerical scheme: by adequate mesh refinement and prevention of pressure field fluctuation at the film thickness discontinuities in each case.

Sensitivity of Results to Changes in Groove Depth. The spiral grooves, chemically etched on one of the seal faces, have manufacturing tolerances that are quite small. However, the groove shape may not be completely square in profile, as is assumed in the present analysis; and surface roughness in the groove results from the etching process. In presenting a novel manufacturing process to place grooves on herringbone groove journal bearings by material deformation, Kang, et al. (1996) discuss the effects of varying the groove shape in detail. To further quantify the effects of a non-uniform groove depth, a 10% change in the groove depth ratio (δ) from the baseline *SGFS* geometry given previously with a large pressure ratio (P_{rat}) of 19.8 is introduced. The effects of this change on SGFS performance as a percentage of the baseline results are: opening force (W), 1%; leakage rate (Q), 3.5%; power loss ($\wp$), 1.5%; static axial stiffness coefficient (K_{zz}), 0.1%; static axial damping coefficient (C_{zz}), 9%. From these results, it is clear that slight changes in the groove depth most profoundly affects the damping and the leakage rate, while other performance characteristics remain almost unchanged for a seal with this large pressure ratio.

RECOMMENDATIONS

The present model adopts many simplifying assumptions that may not entirely pertain to the physical situation. Extensions that would elevate the present work to the state-of-the-art among computational models of its kind include:

- *Misalignments.* Angular misalignment between the faces is a common feature in most present day face seal models. The fact that soft springs hold face seals in place entails that these seals are self-aligning elements, implying that misalignments become unimportant. However, minute face separation distances make the smallest amount of angular misalignment significant since this may induce a parametric excitation, greatly affecting seal performance. Moreover, manufacturing defects resulting in an initially deformed face seal will also influence actual seal function.
- *Thermal coning.* Extremely low flow rates out of *SGFSs* indicate the importance of thermal conduction through the seal faces since little convection heat transfer takes place. Even though innovative materials used in present day applications increase the amount of conduction that occurs, thermal coning remains a topic of great concern to seal designers and users. The thermal coning model employed by Pan and Sternlicht (1967) can easily be extended to the present work although simplifying assumptions may limit its applicability. (Considering that the frictional power dissipation is also small diminishes the importance of thermal effects.)

- *Pressure-Density Relationship.* Employing an isentropic model ($P \propto \rho^{1.4}$), as in Lebeck (1991) rather than the present isothermal model ($P \propto \rho$) would yield an improvement in representing the changes in density with pressure.
- *Fluid inertia and flow turbulence.* Effects from fluid inertia become important in *SGFSs* due to the step change in film thickness at the groove-ridge interface. At higher speeds, when fluid inertia effects overcome the influence of viscous effects (i. e., high Reynolds numbers) flow turbulence also may affect seal performance.
- *Numerical method of solution.* As mentioned earlier, the successive approximation has limitations that may affect its predictive capabilities at high speeds. Incorporating more elements at important locations rather than refining the mesh over the whole groove ridge pair would result in lessening computational time. Higher order elements at the groove-ridge interfaces can also help the present method in obtaining a dependable solution.
- *Incorporating other groove types.* Grooves shapes other than logarithmic spirals are in popular use in present day applications. Most notably, the T-groove seal allows the same sealing performance regardless of rotation direction due to radial symmetry of the grooves. Few predictive models, if any, exist to characterize the performance of this seal type.

PROJECT NOTES

Many difficulties impeded progress of the present research during its development. Most of these dealt with trying to understand the many spiral groove configurations published previously. Often these previous works left unstated parameters necessary to replicate the results, or the parameters stated in the work (after some great thought) seemed clearly erroneous. The present author has made considerable effort to remain completely explicit in stating details about each computation, allowing application of this research to future works.

As mentioned previously, the lack of pertinent experimental data for spiral groove configurations operating with compressible fluids does not allow physical validation of the model and limits model verification to comparison with previous estimates. Many current publications show the success of *SGFS* retrofits into existing machines, demonstrating improved, more economical system performance. However, works that experimentally characterize *SGFS* behavior alone are virtually non-existent. With extremely small operating clearances and inevitable thermal deformation in the seal faces, testing *SGFSs* presents some difficulty with large experimental uncertainties likely to occur. Test data on force, leakage, power loss, and dynamic force coefficients in *SGFSs* may allow further verification of the present model, although much caution must be employed in interpreting any test results as completely valid. Furthermore, *SGFS* manufacturers expressly refuse to provide any geometrical details on seals presently in

use. Thus, examples used in parametric study were contrived from previous analytical works rather than an actual *SGFS*.

This research has taught many valuable lessons. Early analyses (before 1970) have proven quite useful not only for comparison with more modern methodologies but as the basis for the present analysis. In solving the non-linear partial differential equation of pressure, the successive approximation approach compares well against models using more complicated solution techniques, but the implementation of a finite element model eliminates many of the simplifications adopted by the *NGT*, i. e., the number of grooves approaching infinity. However, users of the present computational program must be cautious in trusting convergence on load capacity since this solution may have obvious flaws such as extreme pressure fluctuations in the ridge region that profoundly affect force coefficient calculation.

CONCLUSIONS

The present research analyzes the incompressible and isothermal, compressible fluid flows in spiral groove thrust bearings and face seals using the Reynolds equation for laminar flow. Since the Reynolds equation becomes a non-linear partial differential equation of pressure in the compressible fluid analysis, a successive approximation allows an iterative solution of an intermediate linearized partial differential equation. Discretization of the zeroth- and first-order pressure fields and integration of the partial differential equations of pressure is achieved using the finite element method.

Comparisons of the present analysis (for *SGTBs*) with the *NGT* prove favorable for load capacity and inner diameter pressure, and as expected, the inner diameter pressure variations become significant as the number of grooves lessens. In general, damping force coefficients decrease as the ratio between seal inner and outer radii increases. Finite element calculations given in Someya (1989) for Sommerfeld number versus seal clearance further validate the present work. A parametric study shows the effect of varying the *SGFS* geometry on the opening force, force coefficients, leakage rate, and power loss for incompressible fluids. For a face seal having an inner diameter that is half of the outer diameter ($R = 0.5$) and operating with an incompressible fluid, the optimum geometry determined from this study is: $N_g = 12$; $\beta = 20°$; $l = 0.18$, $\alpha_g = 0.45$; and $\delta \cong 2$ for a pressure ratio (P_{rat}) of 5.1.

Static load capacity, axial stiffness, and leakage rate from the present compressible fluid analysis compare well with results from the *NGT* isentropic

compressible fluid flow model given in Lebeck (1991). The present predictions show higher static load capacity than predictions from James and Potter (1967) and Bonneau, et al. (1993) for inward pumping *SGTBs* operating with a compressible fluid. The load capacity and static axial stiffness given by the *NGT* in Malanoski and Pan (1965) appears higher than predicted by the present work. However, the dramatic behavior of the force coefficients with increasing excitation frequency compares well with those of Malanoski and Pan (1965). This behavior is further characterized as part of a parametric study to identify compressible fluid *SGFS* performance and determine an optimum *SGFS* geometry. For a pressure ratio (P_{rat}) of unity, seal instability, predicted by negative values of axial damping, occurs with large numbers of grooves at low excitation frequencies and becomes more prominent at high speed numbers. At high excitation frequencies, the seal stiffness coefficient and axial damping coefficients tend toward asymptotic values regardless of the number of grooves. Based on predictions of the *SGFS* performance characteristic as the seal geometry changes, the optimum geometry for compressible fluid *SGFSs* is: $N_g = 12$; $\beta = 12°$; $l = 0.16$, $\alpha_g = 0.5$; and $\delta \cong 1.8$.

REFERENCES

Bonneau, D., Huitric, J., and Tournerie, B., 1993, "Finite Element Analysis of Grooved Gas Thrust Bearings and Grooved Gas Face Seals," ASME JOURNAL OF TRIBOLOGY, Vol. 115, pp. 348-354.

Cheng, H. S., Castelli, V., and Chow, C. Y., 1969, "Performance Characteristics of Spiral-Groove and Shrouded Rayleigh Step Profiles for High-Speed Noncontacting Gas Seals," ASME JOURNAL OF LUBRICATION TECHNOLOGY, Vol. 91, pp. 60-68.

Constantinescu, V. N., and Galetuse, S., 1987, "On the Dynamic Stability of the Spiral-Grooved Gas-Lubricated Thrust Bearing," ASME JOURNAL OF TRIBOLOGY, Vol. 109, pp. 183-188.

Constantinescu, V. N., and Galetuse, S., 1992, "On Extending the Narrow Spiral-Groove Theory to Configurations of Interest in Seals," ASME JOURNAL OF TRIBOLOGY, Vol. 114, pp. 563-566.

DiRusso, E., 1982, "Film Thickness Measurement for Spiral Groove and Rayleigh Step Lift Pad Self-Acting Face Seals," NASA Technical Paper 2058.

DiRusso, E., 1983, "Design Analysis of a Self-Acting Spiral-Groove Ring Seal for Counter-Rotating Shafts," NASA Technical Paper 2142.

DiRusso, E., 1984, "Dynamic Behavior of Spiral-Groove and Rayleigh-Step Self-Acting Face Seals," NASA Technical Paper 2266.

DiRusso, E., 1985, "Dynamic Response of Film Thickness in Spiral-Groove Face Seals," NASA Technical Paper 2544.

Furuishi, Y., Suganami, T., Yamamoto, S., and Tokumitsu, K., 1985, "Performance of Water-Lubricated Flat Spiral Groove Bearings," ASME JOURNAL OF TRIBOLOGY, Vol. 107, pp. 268-272.

Hsing, F. C., 1972, "Formulation of a Generalized Narrow Groove Theory for Spiral Grooved Viscous Pumps," ASME JOURNAL OF LUBRICATION TECHNOLOGY, Vol. 94, pp. 81-85.

Hsing, F. C., 1974, "Analytical Solutions for Incompressible Spiral Groove Viscous Pumps," ASME JOURNAL OF LUBRICATION TECHNOLOGY, Vol. 96, pp. 365-369.

James, D. D., and Potter, A. F., 1967, "Numerical Analysis of the Gas-Lubricated Spiral-Groove Thrust Bearing-Compressor," ASME JOURNAL OF LUBRICATION TECHNOLOGY, Vol. 89, pp. 439-444.

Kang, K., Rhim, Y., and Sung, K., 1996, "A Study of the Oil-Lubricated Herringbone-Grooved Journal Bearing – Part 1: Numerical Analysis," ASME JOURNAL OF TRIBOLOGY, Vol. 118, pp. 906-911.

Kowalski, C. A., and Basu, P., 1995, "Reverse Rotation Capability of Spiral-Groove Gas Face Seals," *Tribology Transactions*, Vol. 38, pp. 549-556.

Lebeck, A. O., 1991. *Principles and Design of Mechanical Face Seals*, Wiley, New York.

Malanoski, S. B., and Pan, C. H. T., 1965, "The Static and Dynamic Characteristics of the Spiral-Grooved Thrust Bearing," ASME *Journal of Basic Engineering*, Vol. 87, pp. 547-558.

Muijderman, E. A., 1966, *Spiral Groove Bearings*, Philips Technical Laboratory, Springer-Verlag Inc., New York.

Pan, C. H. T., and Sternlicht, B., 1967, "Thermal Distortion of Spiral-Grooved Gas-Lubricated Thrust Bearing Due to Self-Heating," ASME JOURNAL OF LUBRICATION TECHNOLOGY, Vol. 89, pp. 197-202.

Reddi, M. M., 1969, "Finite Element Solution of the Incompressible Lubrication Problem," ASME JOURNAL OF LUBRICATION TECHNOLOGY, Vol. 91, pp. 529-533.

Reddi, M. M., and Chu, T. Y., 1970, "Finite Element Solution of the Steady-State Compressible Lubrication Problem," ASME JOURNAL OF LUBRICATION TECHNOLOGY, Vol. 92, pp. 495-503.

Reddy, J. N, 1993. *Introduction to the Finite Element Method, Second Edition*, McGraw-Hill, New York.

Salant, R. F., and Homiller, S. J., 1992, "The Effects of Shallow Groove Patterns on Mechanical Seal Leakage," *Tribology Transactions*, Vol. 35, pp. 142-148.

Sato, Y., Ono, K., and Iwama, A., 1990, "The Optimum Groove Geometry for Spiral Groove Viscous Pumps," ASME JOURNAL OF TRIBOLOGY, Vol. 112, pp. 409-414.

Shapiro, W., Walowit, J., and Jones, H. F., 1984, "Analysis of Spiral-Groove Face Seals for Liquid Oxygen," *ASLE Transactions*, Vol. 27, 3, pp. 177-188.

Smalley, A. J., 1972, "The Narrow Groove Theory of Spiral Groove Gas Bearings: Development and Application of a Generalized Formulation for Numerical Solution," ASME JOURNAL OF LUBRICATION TECHNOLOGY, Vol. 94, pp. 86-92.

Sneck, H. J., and McGovern, J. F., 1973, "Analytical Investigation of the Spiral Groove Face Seal," ASME JOURNAL OF LUBRICATION TECHNOLOGY, Vol. 95, pp. 499-509.

Someya, T. (editor), 1989, *Journal-Bearing Databook*, Springer-Verlag, Berlin.

Zirkelback, N., and San Andrés, L., 1997, "Finite Element Analysis of a Herringbone Groove Journal Bearing: A Parametric Study," ASME Paper 97-Trib-14.

APPENDIX A

CHARACTERISTIC VALUES USED FOR DIMENSIONLESS PARAMETERS

Dimensionless Values.

Load Capacity	Force Coefficients	Speed Number
$\overline{W} = W/W_*$	$\overline{K}_{zz} = K_{zz}/K_*$	$\Lambda = 6\mu\Omega/P_*\left(R_o/c\right)^2$
$S = \mu N \pi R_o^2 \left(R_o/c_g\right)^2 / W$	$C_{zz} = C_{zz}/C_*$	

Leakage Rate	Power Loss	Pressure
$\overline{Q} = Q/Q_*$	$\overline{\wp} = \wp/\wp_*$	$\overline{P} = P/P_*$

Incompressible Fluid Models.

Comparison with Muijderman (1966). (*SGTB*, $P_{ref} = 0$)

Load capacity [N]	$W_* = \mu\Omega R_o^4/c^2$
Calculated inner diameter pressures [Pa]	$P_* = \mu\Omega\left(R_o/c\right)^2$
Force coefficients [N]	$W_* = \pi R_o^2 \mu\Omega\left(R_o/c_g\right)^2$
	$K_* = W_*/c_g \; ; \; C_* = K_*/\Omega$

Incompressible Fluid Parametric Study. (*SGFS*, $P_{ref} = 101.3$ kPa)

Pressure [Pa]	$P_* = P_i$
Opening force [N]	$W_* = \pi\left(R_o^2 - R_i^2\right)\mu\Omega\left(R_o/c_g\right)^2$

Power loss [W] $\wp_{\bullet} = \pi\mu\Omega^2\left(R_o^4 - R_i^4\right)/2c_g$

Leakage [ℓ/min] $Q_{\bullet} = 6\times10^4\,\pi c_g^3\left(P_i - P_o\right)/6\mu\ln\left(R_o/R_i\right)$

Force Coefficients $K_{\bullet} = W_{\bullet}/c_g$

Compressible Fluid Models.

Comparison with Lebeck (1991). (*SGFS*, P_{ref}= 101 kPa)

Pressure [Pa] $P_{\bullet} = P_i$

Opening Force [N] $\overline{W} = \left[W + \pi P_i\left(R_o^2 - R_i^2\right)\right]/W_{\bullet}$

$W_{\bullet} = \pi\left(R_o^2 - R_i^2\right)\left(P_o - P_i\right)$

Leakage Rate [kg/s] $Q_{\bullet} = \pi\rho_{avg}\left(c + c_g\right)^3\left(P_i - P_o\right)/6\mu\ln\left(R_o/R_i\right)$

$\rho_{avg} = \left(P_i + P_o\right)/2\Re_g T$

Static Axial Stiffness coefficient $K_{\bullet} = W_{\bullet}/c$

Comparison with James and Potter (1967) and Bonneau, et al. (1993).

(*SGTB*, P_{ref}= 101 kPa)

Pressure [Pa] $P_{\bullet} = P_o$

Load Capacity [N] $W_{\bullet} = \pi P_o\left(R_o^2 - R_i^2\right)$

Comparison with Malanoski and Pan (1965). (*SGTB*, P_{ref} = 101 kPa)

Pressure [Pa] $P_\bullet = P_o$

Load Capacity [N] $W_\bullet = \pi P_o \Lambda \left(R_o^2 - R_i^2 \right) / 100$

Force Coefficients $K_\bullet = W_\bullet / c \; ; \; C_\bullet = K_\bullet / \Omega$

Compressible Fluid Parametric Study. (*SGFS*, P_{ref} = 101 kPa)

Opening Force [N] $W_\bullet = \pi P_{avg} \left(R_o^2 - R_i^2 \right) ; \; P_{avg} = \left(P_i + P_o \right) / 2$

Pressure [Pa] $P_\bullet = P_i$

Power Loss [W] $\wp_\bullet = \pi \mu \Omega^2 \left(R_o^4 - R_i^4 \right) / 2c$

Leakage Rate [kg/s] $Q_\bullet = \pi \rho_{avg} \left(c + c_g \right)^3 \left(P_i - P_o \right) / 6 \mu \ln \left(R_o / R_i \right)$

$\rho_{avg} = \left(P_i + P_o \right) / 2 \Re_g T$

Force Coefficients $K_\bullet = W_\bullet / c \; ; \; C_\bullet = K_\bullet / \Omega$

Table A1. Variation of groove rotation direction with seal configuration.

Groove Angle (β) Range	Rotating Grooves	Stationary Grooves
Inward pumping grooves, inner diameter seal dams		
$0° < \beta < 90°$	$B = +1$	$B = -1$
$90° < \beta < 180°$	$B = -1$	$B = +1$
Outward pumping grooves, outer diameter seal dams		
$0° < \beta < 90°$	$B = -1$	$B = +1$
$90° < \beta < 180°$	$B = +1$	$B = -1$

APPENDIX B

SGTB/SGFS GEOMETRIES AND FEM PARAMETERS FOR VALIDATIONS

Incompressible Fluid Models.

Comparison with Muijderman (1966).

Geometry: *SGTB* without inner radial flow. Parameters given specifically in figures.

FEM: Radial elements: 50

Circumferential elements (groove, ridge): 10, 10.

Comparison with Someya (1989).

Geometry: *SGTB* without inner radial flow.

$R = 0.5$, $R_g = 0.6$, $\alpha = 0.5$, $\beta = 30°$, $N_g = 10$, $\rho = 998$ kg/m^3, $\mu = 1.90\times10^{-5}$ Pa·s

FEM: Radial elements (groove, dam): 40, 5

Circumferential Elements (groove, ridge): 10, 10

Incompressible Fluid Parametric Study.

Geometry: Table 1. (*SGFS*)

FEM: Radial Elements (groove, dam): 40, 10

Circumferential Elements (groove, ridge): 10, 10

Compressible Fluid Models.

Comparison with Lebeck (1991).

Geometry: Table 2. (*SGFS*)

FEM: Radial Elements (groove, dam): 10, 15

Circumferential Elements (groove, ridge): 5, 10

Comparison with James and Potter (1967) and Bonneau, et al. (1993).

Geometry: *SGTB* with inner radial flow.

$R = 0.3848$, $\delta = 6$, $\Omega = 24{,}000$ RPM, $\beta = 70°$, $\alpha_g = 0.8$, $N_g = 12$, $\mu = 3.237\times10^{-5}$ Pa·s

$\Lambda = 175.7$, P_i/P_o varies.

FEM: Radial Elements: 12

Circumferential Elements (groove, ridge): 12, 12

Comparison with Malanoski and Pan (1965).

Geometry: *SGTB* with inner radial flow.

SGTB: $R = 0.4$, l = 0.2667, $\delta = 3.05$, $\beta = 161.2°$, $\alpha_g = 0.6587$, $N_g = 50$

$P_{rat} = 1$, $\mu = 1.9\times10$-5

FEM: Radial Elements (groove, dam): 10, 15

Circumferential Elements (groove, ridge): 5, 10

Compressible Fluid Parametric Study.

Geometry: Table 3. (*SGFS*)

FEM: Radial Elements (groove, dam): 10, 15

Circumferential Elements (groove, ridge): 5, 10

(These vary slightly when the geometry deviates greatly from the baseline.)

APPENDIX C

Load and Inner Radius Pressure for SGTBs without Inward Radial Flow (Muijderman, 1966) *Sample Calculation*

(Names next to titles indicate nomenclature in use.)

Fixed Parameters (Zirkelback)

$R_{go} := .0425 \cdot m$

$c_g := 8 \cdot 10^{-6} \cdot m$

$N_g := 15$

$\Omega := 31.4 \cdot \frac{rad}{sec}$

$\mu := .19 \cdot 10^{-4} \cdot Pa \cdot sec$

$\rho := 998 \cdot \frac{kg}{m^3}$

Parameters for Case 1 (Zirkelback)

$R_{gi} := .0170 \cdot m$

$c := 2.56 \cdot 10^{-6} \cdot m$

$\beta := .216420827247 \cdot rad$

$\alpha_r := .537037037037$

Nomenclature (Muijderman)

h_0 : Groove depth [m]

h_1 : Film height above grooves [m] $h_1 = h_0 - h_2$

h_2 : Film height above ridges [m]

H : Groove depth ratio $H = \frac{h_2}{h_1}$

k : Number of grooves

(r, θ) : Groove coordinate system

r_1 : Inner radius of grooved part

r_2 : Outer radius of grooved part [m]

W : Load carrying capacity [N]

α : Groove angle [rad] $r = r_1 \cdot e^{\theta \cdot \tan(\alpha)}$

γ : Ratio of ridge width to groove width

η : Dynamic viscosity [N-s/m^2]

ω : Angular velocity [rad/s]

Nomenclature Conversion (M := Z)

$h_0 := c_g$

$h_1 := c - c_g$

$h_2 := c$

$H := \frac{c}{c - c_g}$

$k := N_g$

$r_1 := R_{gi}$

$r_2 := R_{go}$

$\alpha := \beta$

$\gamma := \frac{\alpha_r}{1 - \alpha_r}$

$\eta := \mu$

$\omega := \Omega$

Governing Equations (Muijderman)

Further Definitions (Equations numbers in Muijderman (1966) listed.)

Characteristic Load:

$$W_s = \frac{\eta \cdot \omega \cdot r_2^{\,4}}{h_2^{\,2}}$$

$$g_1 = \frac{\gamma \cdot H^2 \cdot \cot(\alpha) \cdot (1 - H) \cdot (1 - H^3)}{(1 - \gamma \cdot H^3) \cdot (\gamma - H^3) - H^3 \cdot \cot(\alpha)^2 \cdot (1 - \gamma)^2} \qquad (2.62)$$

$$\lambda = \frac{r_1}{r_2} \qquad (5.8)$$

$$C_1 = \frac{\exp\left[\frac{\pi}{k} \cdot \left(1 - \frac{2 \cdot \alpha}{\pi}\right) \cdot (\tan(\alpha)) \cdot \left(\frac{2}{1 + \gamma}\right) \cdot \left(\frac{1 - \gamma \cdot H^3}{1 - H^3}\right)\right] - \lambda^2 \cdot \exp\left[\frac{\pi}{k} \cdot \left(1 - \frac{2 \cdot \alpha}{\pi}\right) \cdot (\tan(\alpha)) \cdot \left(\frac{2}{1 + \gamma}\right) \cdot \left(\frac{1 + \gamma \cdot H^3}{1 - H^3}\right)\right]}{1 - \lambda^2}$$

$$p_{r1} = \frac{3 \cdot \eta \cdot \omega \cdot r_2^{\,2}}{h_2^{\,2}} \cdot (1 - \lambda^2) \cdot g_1 \cdot C_1 \qquad (5.7)$$

$p_{r1} = 3.54763 \cdot 10^4 \cdot \text{Pa}$ <== Pressure at the inner diameter

(5.10)

$$C_2 = \frac{\exp\left[\frac{2 \cdot \pi}{k} \cdot \left(1 - \frac{2 \cdot \alpha}{\pi}\right) \cdot \tan(\alpha) \cdot \left(\frac{2}{1 + \gamma}\right) \cdot \left(\frac{1 + \gamma \cdot H^3}{1 + H^3}\right)\right] - \lambda^4 \cdot \exp\left[\frac{2 \cdot \pi}{k} \cdot \left(1 - \frac{2 \cdot \alpha}{\pi}\right) \cdot \tan(\alpha) \cdot \left(\frac{2}{1 + \gamma}\right) \cdot \left(\frac{1 + \gamma \cdot H^3}{1 + H^3}\right)\right]}{1 - \lambda^4}$$

$$W_t = \frac{3 \cdot \pi \cdot \eta \cdot \omega \cdot r_2^{\,4}}{2 \cdot h_2^{\,2}} \cdot (1 - \lambda^4) \cdot g_1 \cdot C_2 \qquad (5.9) \qquad W = \frac{W_t}{W_s}$$

$W_t = 113.72334 \cdot \text{kg} \cdot \text{m} \cdot \text{sec}^{-2}$ <== NGT load capacity

$W = 0.3829$ <== NGT dimensionless load capacity

APPENDIX D

COMPRESSIBLE FLUID SGFS COMPUTATIONAL CODE FLOW CHART

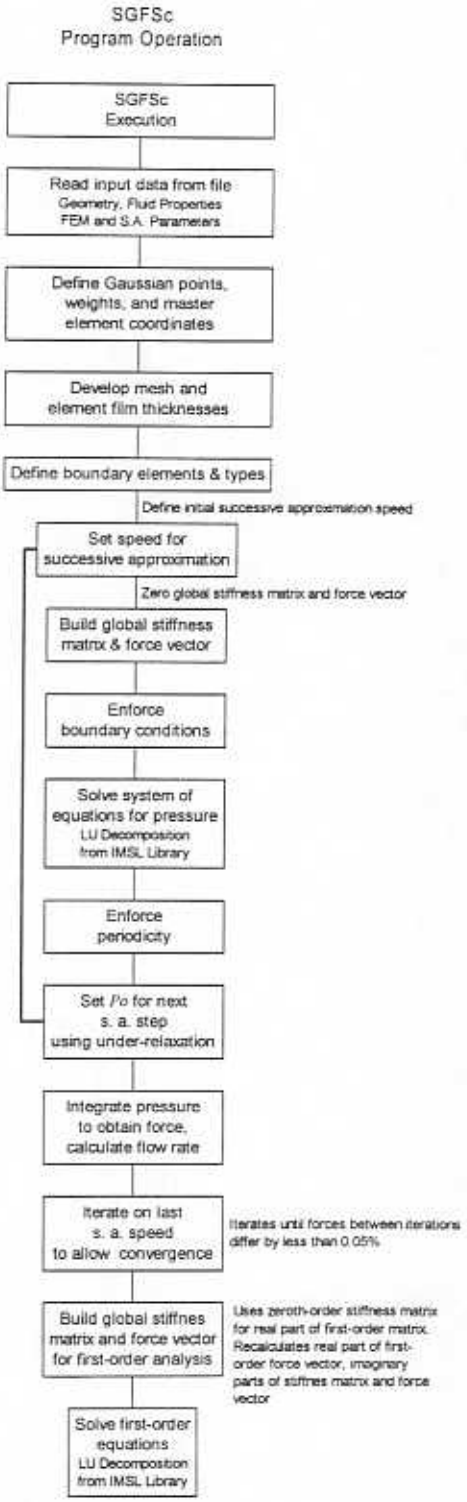

APPENDIX E

IMPROVEMENTS TO *SPIRALC* FOR EFFICIENT STORAGE AND SOLUTION OF SPARSE UNSYMMETRICAL SYSTEM OF EQUATIONS

Marco Faria
Graduate Student

INTRODUCTION

A sparse matrix storage procedure for unsymmetric matrices is implemented into the finite element code *SPIRALC*. The procedure based on a skyline profile storage technique reduces the computational effort in the solution of the compressible fluid Reynolds equation for spiral groove thrust bearings (SGTBs) and face seals (SGFSs).

Non-banded unsymmetric matrices are obtained in the finite element modeling of the non-linear Reynolds equation subject to periodic boundary conditions. In the former version of SPIRALC, the matrices are defined in their full extent to allow the use of available canned subroutines.

In this enhanced version of SPIRALC, unsymmetric matrices are assembled and stored by using skyline storage techniques [Bathe,1982]. Basically, most of the zero entries of the matrix are not stored. Using Gauss elimination method, a direct solution method for systems of linear equations is developed to handle the sparse matrices generated by the model.

Some performance tests are carried out in order to compare the solution times of both versions of SPIRALC. The enhanced version is more efficient than the former one in terms of computational effort. The code structure and the accuracy of the results remain unchanged.

UNSYMMETRIC SPARSE MATRICES

The zero-th and first-order Reynolds equations lead to sparse unsymmetric matrices. The sparse unsymmetric matrices are obtained by superposing the finite element matrices,

whose expressions are given by equations (30) and (33.a)[1]. Periodic boundary conditions (see equation (6)) produce a lack of bandwidth in the global finite element matrices. Figure 1 shows schematically the matrix structure of the sparse unsymmetric matrices assembled by SPIRALC.

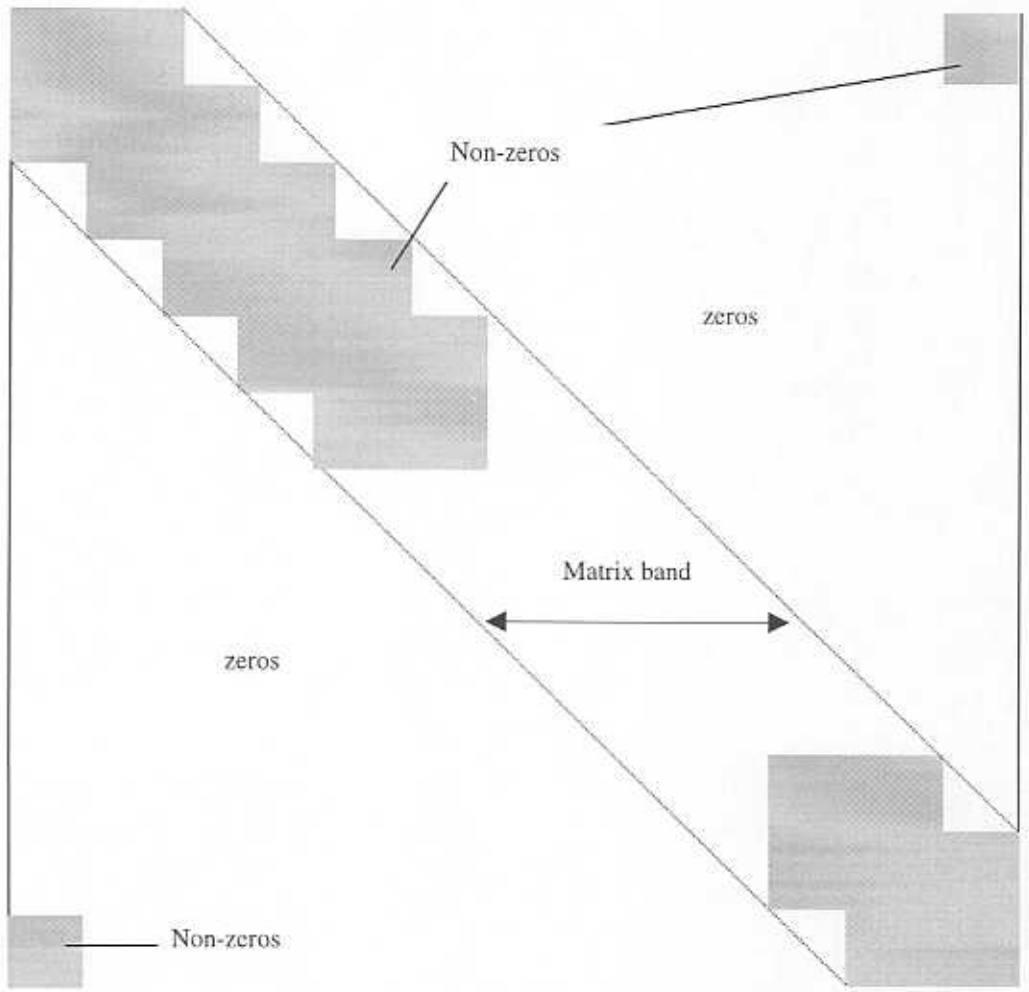

Figure 1 – Unsymmetric sparse matrix structure with periodic boundary conditions.

[1] Equation numbers refer to the main text of this report.

Non-zero entries are located around the main diagonal and on the upper right and lower left corners of the matrix.

MATRIX STORAGE PROCEDURE

The storage procedure stores the unsymmetric matrix into two vectors. These vectors, *KU(j)* and *KL(j)*, store the skyline profiles of the upper and lower triangular matrices, respectively. Index *j* varies from *1* to the total number of entries stored by each vector. The entries stored by the vectors *KU(j)* and *KL(j)* are shown in figure 2.

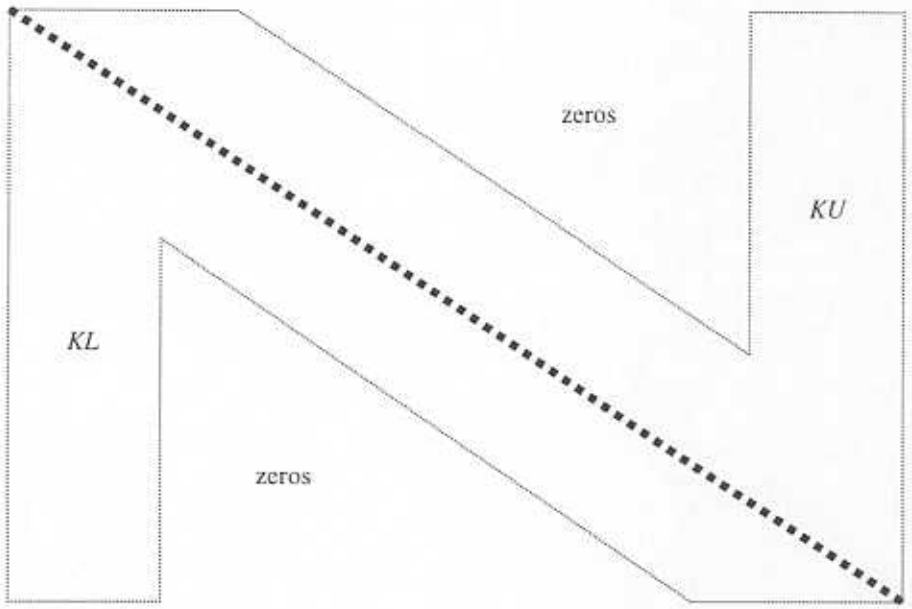

Figure 2 – Profile of the unsymmetric matrix stored in vectors *KU(j)* and *KL(j)*.

A column-oriented algorithm is used to implement the storage procedure. Vector *KU(j)* stores non-zero entries of the upper triangular matrix. Two additional vectors, *IPU(k)* and *ISU(k)*, where *k* is the column index, are used to carry out the storage of the upper

triangular matrix. For the k-th column, *IPU(k)* represents the address of the diagonal element in the vector *KU(j)*, while *ISU(k)* gives the number of entries of the matrix stored in the k-th column .

Vector *KL(j)* stores the entries of the lower triangular matrix. Also two additional vectors, *IPL(k)* and *ISL(k)*, which give the address of the diagonal element and the number of elements stored at the k-th column, respectively, are employed in the storage procedure. The following example shows the storage procedure.

EXAMPLE: Determination of vectors *KU(j)*, *KL(j)*, *IPU(k)*, *ISU(k)*, *IPL(k)*, and *ISL(k)* for the arbitrary sparse unsymmetric matrix given below.

$$\begin{bmatrix} 1 & -3 & 0 & 0 & 6 \\ 2 & 4 & 2 & 0 & 0 \\ 0 & -1 & 3 & 5 & 0 \\ 0 & 0 & 2 & -1 & 7 \\ -5 & 0 & 0 & 3 & 1 \end{bmatrix}$$

The skyline profile vectors *KU(j)* and *KL(j)* are built in the following manner.

$$KU = \{1 \quad -3 \quad 4 \quad 2 \quad 3 \quad 5 \quad -1 \quad 6 \quad 0 \quad 0 \quad 7 \quad 1\}^T$$

$$KL = \{1 \quad 2 \quad 0 \quad 0 \quad -5 \quad 4 \quad -1 \quad 3 \quad 2 \quad -1 \quad 3 \quad 1\}^T$$

The vectors used to identify both upper and lower triangular matrices are given in the following table.

Column	1	2	3	4	5
IPU	1	3	5	7	12
ISU	1	2	2	2	5
IPL	1	6	8	10	12
ISL	5	2	2	2	1

All non-zero entries of the unsymmetric matrix are stored in the vectors *KU(j)* and *KL(j)*.

DIRECT SOLUTION METHOD

Applying the successive approximation method to the non-linear Reynolds equation results in a set of linear differential equations (eq. 23). These linear equations lead to sparse systems of linear algebraic equations. A direct solver based on the Gauss elimination method is used to solve the systems of equations.

Gaussian elimination is adequate for the solution of general problems of nonsymmetric systems of linear equations [Press et al.,1989]. This method is chosen for its ease of implementation. An unsymmetric matrix K is factored into the product of a lower triangular matrix L and an upper triangular matrix U, as follows.

$$K = LU \tag{i}$$

The triangularization is performed by subtracting rows from the product of other rows by their multipliers. In SPIRALC, during the elimination process, certain zero entries of the lower triangular matrix L can become non-zero. Direct solvers produce this phenomenon of "fill-in" during the solution of sparse linear systems [Wahl et al.,1996].

At the solver input, the vectors *KU* and *KL* store the skyline profiles of the upper and lower triangular matrices of *K*, respectively. After the Gaussian elimination, vector *KU* stores the decomposed upper triangular matrix in skyline profile, which is used in the back substitution procedure. Vector *KL* will store the full lower triangular matrix, which contains the multipliers computed by the elimination process [Stewart, 1996].

COMPARATIVE TESTS

Some cases of compressible spiral groove thrust bearings (SGTB) and face seals (SGFS) are selected to evaluate the performance of both versions of SPIRALC. The codes are written in Fortran 90 for Microsoft PowerStation v.4. The tests are carried out on a computer Pentium 586, 200 MHz, with 64 MB of RAM.

Variable names used in the input files are described in the User's manual [Zirkelback and San Andres, 1997]. Three examples of lubricated grooved parallel plates are chosen. Computational efforts are determined for three finite element meshes to assess the code efficiency for increasing number of linear algebraic equations. The former version of SPIRALC employs the optimized subroutines DLSARG and DLSACG from IMSLIB to solve the linear systems of algebraic equations derived from the compressible fluid Reynolds equation.

Example 1: Dynamic force coefficients are computed for a spiral groove face seal. Direct and inverse problems are solved. A sample of the input file describing the seal parameters is shown as follows.

```
SGFS: 1998     Example 1
03/31/98
50                                  Number of Grooves
.11200E+00    .20000E+00            Inner,Outer Diam. [m]
.80000E-01    .20000E+00            Inner,Outer Seal-Dam Diam. [m]
.10000E-04    .30500E-04            Cr [m],Cg [m]
.65870E+00    .16120E+03            Groove width ratio, helix angle [deg]
.29318E+05                          Shaft Speed [RPM]
.10000E+06    .10000E+06            I.D.,O.D. pressures [Pa]
10    10    10                      # rad.,circ.(groove),& circ.(ridge) elements
10      0                           # radial inner, outer seal-dam elements
0                                   (0/1) traces calculations (No/Yes)
20    .10000E-02                    Max # load iterations, Max % error
.19000E-04    .13220E+01            Liquid viscosity [Pa.s], & density [kg/m^3]
1  0                Groove rotation direction(±1),Thrust Bearing (0/1 = N/Y)
5    .75000E+00     Number of s.approx steps,RPM fraction for s.a. start
.50000E+00                          Under relaxation parameter
1                                   Number RPM fractions for force coeff calc
.10000E-03                          RPM Fractions
```

Three finite element meshes are used to model a seal ridge-groove pair. The meshes are given in the following manner.

Table 1 – Finite Element Meshes.

Mesh (number of elements)	400	625	900
No. of radial elements – groove region	10	15	20
No. of circumferential elements – groove region	10	15	20
No. of circumferential elements – ridge region	10	10	10
No. of radial elements – inner seal dam	10	10	10

Numerical results computed by both the original and enhanced versions of SPIRALC are exactly the same. A sample of an output file calculated for the direct problem with a mesh of 400 elements is given as follows.

```
OPTION 4: Find the LOAD given the MINIMUM CLEARANCE (from INPUT.TXT)
-------------------------------------------------------------------------
Cr          Force         Qout                PowL            Pmax
[um]        [N]           [kmole.K/s]         [W]             [MPa]
10.000      8688.1       -.30534E-02          1784.7          .80625
Freq No.     Freq          Freq/Speed          Kzz             Czz
[ - ]        [Hz]          [ - ]               [MN/m]          [kN.s/m]
.70000E-01  .48863E-01     .10000E-03          1618.3         -2451.1
```

Table 2 shows the CPU time for both versions of SPIRALC in the solution of the direct and inverse problems. T_o gives the CPU time in seconds calculated for original version, while T_n gives the time for the enhanced version. A force of 1000 N is used to solve the inverse problem.

Table 2 – CPU times for the inverse and direct problems.

	Direct Problem – CPU time			*Inverse Problem – CPU time*		
Mesh	T_o (s)	T_n (s)	T_o/T_n	T_o (s)	T_n (s)	T_o/T_n
400	38.85	16.07	2.42	270.74	110.41	2.45
625	119.61	44.16	2.71	836.41	304.41	2.75
900	319.83	102.37	3.12	2212.38	711.80	3.11

As the number of elements increases, the superior computational efficiency of the enhanced version of SPIRALC becomes more evident. Figure 3 depicts the computational efforts of both original and enhanced versions of SPIRALC for the direct problem.

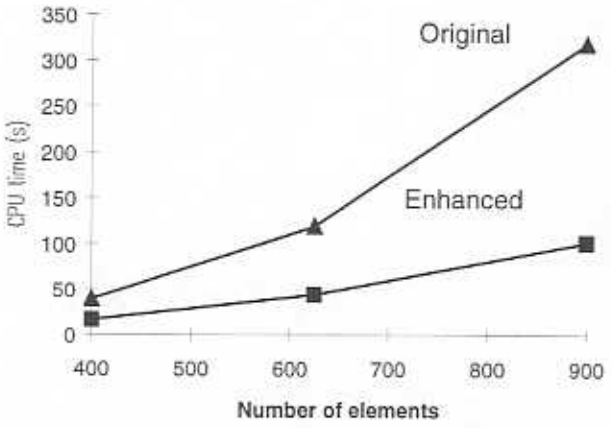

Figure 3 – Computational efficiency of SPIRALC for the direct problem of example 1.

Example 2: Dynamic force coefficients of a SGFS are determined for several values of excitation frequency. A sample of the input file used in this example is shown below.

```
SGFS: 1998  Example 2
04/02/98
12                          Number of Grooves
0.11352E+00  0.13200E+00     Inner,Outer Diam. [m]
0.1056 0.132                Dsi,Dso
0.40000E-05  0.80000E-05     Cr [m],Cg [m]
0.50000E+00  20.0            Groove ratio, helix angle [deg]
0.50000E+04                 Shaft Speed [RPM]
0.10100E+06  2.00000E+06     I.D.,O.D. pressures [Pa]
10   10   10                 # rad.,circ.(groove),& circ.(ridge) elements
10      0                   Nsi,Nso
0                           =1: traces calculations, =0 (no)
10  0.10000E+01             Max # load iterations, Max % error
0.19000E-04  0.93760E+00    Liquid viscosity [Pa.s], & density[kg/m^3]
-1 0                        -1=>Grooves rotate; 1=>Grooves fixed
5  0.75000E+00             Number of s.a. steps, fraction of omega to start
0.50000E+00                 Relaxation factor
8                           # fractions of RPM for force coef. calculations
0.00000E+00                 Fractions of RPM for coeff. calculation
0.015537818
0.031075635
0.155378177
0.310756353
0.621512706
1.553781765
3.10756353
```

The direct problem is solved by using the same finite element meshes as those used in example 1. Both versions of SPIRALC give exactly the same results. A sample of an output file calculated in this example for a mesh of 400 elements is given as follows.

```
OPTION 4: Find the LOAD given the MINIMUM CLEARANCE (from INPUT.TXT)
-------------------------------------------------------------------------------
Cr          Force        Qout              PowL          Pmax
[um]        [N]          [kmole.K/s]       [W]           [MPa]
4.0000      7812.6      -.42386E-02        17.906        2.0000
Freq No.      Freq         Freq/Speed        Kzz              Cz
[ - ]         [Hz]         [ - ]             [MN/m]           [kN.s/m]
.03218        0.0833       .10000E-03        331.57           68.138
5.0000        1.2948       .15538E-01        331.57           68.138
10.000        2.5896       .31076E-01        331.57           68.138
50.000        12.948       .15538            331.62           68.134
100.00        25.896       .31076            331.74           68.121
200.00        51.793       .62151            332.26           68.068
500.00        129.48       1.5538            335.84           67.703
1000.0        258.96       3.1076            348.28           66.433
```

Table 3 gives the CPU time calculated by both versions of SPIRALC . Indexes o and n are referred to as original and enhanced, respectively.

Table 3 – CPU time for the direct problem.

	Example 2 – CPU time		
Mesh	T_o (s)	T_n (s)	T_o/T_n
400	99.08	54.52	1.82
625	322.17	152.51	2.11
900	867.33	365.75	2.37

Figure 4 depicts the computational efficiency of SPIRALC for example 2.

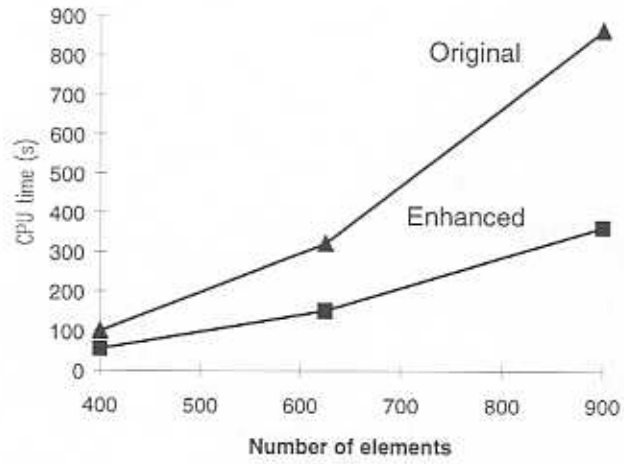

Figure 4 – Computational efficiency of SPIRALC in example 2.

Numerical results show that the new matrix storage procedure makes the enhanced SPIRALC perform much more efficiently than the former code as the number of elements increases.

Example 3: The third and last test consists of computing the dynamic force coefficients for a spiral groove thrust bearing. Three finite element meshes are selected for the computation as shown in Table 4.

Table 4 – Finite Element Meshes.

Mesh (number of elements)	**360**	**648**	**800**
No. of radial elements – groove region	15	18	20
No. of circumferential elements – groove region	12	18	20
No. of circumferential elements – ridge region	12	18	20

An input file used in example 3 is shown as follows.

```
SGTB: 1998  Example 3
04/07/98
12                          Number of Grooves
.12700E-01    .33020E-01    Inner,Outer Diam. [m]
.12700E-01    .33020E-01    Inner,Outer Seal-Dam Diam. [m]
.27500E-05    .16500E-04    Cr [m],Cg [m]
.80000E+00    .11000E+03    Groove width ratio, helix angle [deg]
.24000E+05                  Shaft Speed [RPM]
.10000E+06    .10000E+06    I.D.,O.D. pressures [Pa]
15  12  12                  # rad.,circ.(groove),& circ.(ridge) elements
0   0                       # radial inner, outer seal-dam elements
0                           (0/1) traces calculations (No/Yes)
20    .10000E-02            Max # load iterations, Max % error
.32370E-04    .11233E+01    Liquid viscosity [Pa.s], & density [kg/m^3]
1  0                Groove rotation direction(±1),Thrust Bearing (0/1 = N/Y)
5    .75000E+00        Number of s.approx steps,RPM fraction for s.a. start
.50000E+00                  Under relaxation parameter
1                           Number RPM fractions for force coeff calc
.10000E-03                  RPM Fractions
```

Both versions of SPIRALC render exactly the same results for the example. Results computed for mesh of 360 elements are given as.

```
OPTION 4: Find the LOAD given the MINIMUM CLEARANCE (from INPUT.TXT)
-------------------------------------------------------------------------------
Cr          Force          Qout              PowL              Pmax
[um]        [N]            [kmole.K/s]       [W]               [MPa]
2.7500      3.5276        -.36639E-04        3.8902            .13150
Freq No.      Freq           Freq/Speed        Kzz               Czz
[ - ]         [Hz]           [ - ]             [MN/m]            [kN.s/m]
.35188E-01    .40000E-01     .10000E-03        .98013            .59111
```

Table 5 shows the CPU time for the three finite element meshes presented in Table 4. The results of Table 5 show the same trend presented in the two previous examples. As the number of degrees of freedom increases, the enhanced SPIRALC performs much more efficiently than the former one. Figure 5 depicts a comparison of CPU time for both versions.

Table 5 – CPU time for the direct problem.

	Example 3 – CPU time		
Mesh	T_o (s)	T_n (s)	T_o/T_n
360	35.32	12.83	2.75
648	137.74	37.82	3.64
800	239.75	59.95	4.00

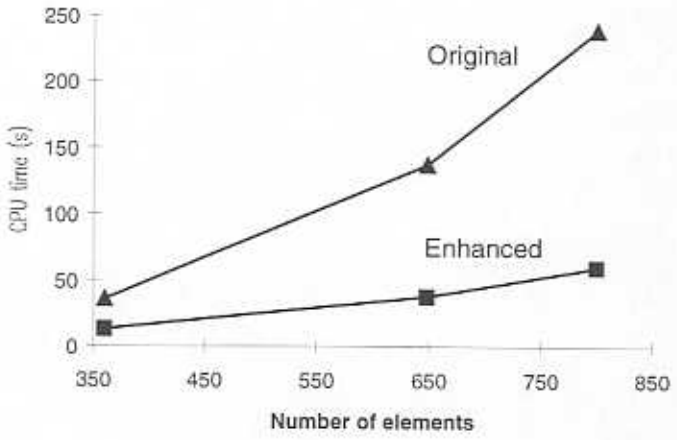

Figure 5 – Computational Efficiency of SPIRALC on example 3.

FINAL REMARKS

Improvements on the computational efficiency of linear system solvers can be achieved by developing customized algorithms for sparse matrices. This concept has been widely used in numerical methods for engineering analysis, such as finite element, finite difference and boundary element methods. For large-scale problems, sparsity is a property that needs to be accounted for to reduce considerably the computing time.

A matrix storage procedure for sparse unsymmetric matrices is implemented into the code SPIRALC to increase its computational efficiency. Also a direct solver which uses the Gauss elimination method with the new matrix storage is implemented to solve sparse systems of linear equations generated by the compressible fluid Reynolds equation. Numerical tests demonstrate that the enhanced version of SPIRALC performs more efficiently than the former one. Efforts spent in the development of the sparse unsymmetric storage procedure and direct solver are thoroughly justified. Time savings achieved by the enhanced

code are remarkable indicators of the computational improvement achieved by the applied matrix storage technique.

REFERENCES

Bathe, K.J., 1982, *Finite Element Procedures in Engineering Analysis*, Prentice-Hall, Inc., Englewood Cliffs, NJ, p702-706.

Press, W.H., Flannery, B.P., Teukolsky, S.A., and Vetterling, W.T., 1989, *Numerical Recipes*, Cambridge University Press, p19-38.

Stewart, G.W., 1996, *Afternotes on Numerical Analysis*, SIAM books, p98-102.

Wahl, M.H., Lee, P.R., and Talke, F.E., 1996, "An Efficient Finite Element-Based Air Bearing Simulator for Pivoted Slider Bearings Using Bi-conjugate Gradient Algorithms", *STLE Tribology Transactions*, v39, No.1, p130-138.

Zirkelback, N., and San Andres, L., 1997, "*SPIRAL, SPIRALC* – Release 1.0 – Combined User's Manual", *TRC Report* No.TRC-SEAL-4-97.